University of Stavanger

Faculty of Science and Technology

MASTER'S THESIS

Study program/Specialization: Petroleum Geosciences Engineering	Spring, 2018 Open
Writer: Lars Ulsund Frette	(Writer's signature)

Faculty supervisor:
Nestor Cardozo, University of Stavanger

External supervisor(s):
Surender Manral, Schlumberger SIS
Lothar Schulte, Schlumberger SIS

Title of thesis:

Quantitative seismic interpretation using converted PS waves: A case study from the Oseberg South Field, North Sea

Credits (ECTS): 30

Keywords: Converted waves, AVO, Seismic inversion, Vp/Vs, Oseberg South	Pages: 105 Stavanger, 15th June, 2018

Quantitative seismic interpretation using converted PS waves: A case study from the Oseberg South Field, North Sea

by

Lars Ulsund Frette

MSc Thesis

Presented to the Faculty of Science and Technology

The University of Stavanger

The University of Stavanger

June 2018

Acknowledgements

This Master thesis is submitted in completion of the MSc in Petroleum Geoscience Engineering at the University of Stavanger.

I would like to thank my supervisors Nestor Cardozo, Surender Manral, and Lothar Schulte for their excellent guidance, both technical and theoretical, and for their constructive feedback needed for the completion of this Master thesis. In addition, I am grateful to Equinor ASA for providing the dataset and to Schlumberger for providing the software Petrel, which was used in this thesis.

I would also like to express my appreciation to my fellow colleagues and friends for their support, and for the time spent together at the University of Stavanger. Finally, I would like to thank my family, and especially my two girls at home, Stine and Lotte, whose support throughout this Master has been admirable.

Quantitative seismic interpretation using converted PS waves: A case study from the Oseberg South Field, North Sea

Lars Ulsund Frette

The University of Stavanger, 2018

Supervisors: Nestor Cardozo, Surender Manral, and Lothar Schulte

Abstract

The converted wave (PS) seismic in combination with the compressional wave (PP) seismic may help in better description and understanding of subsurface stratigraphic and structural features. Since compressional and shear waves sense different rock and pore-fluid properties, inversion of PP and PS seismic data can provide better insight into reservoir lithology and fluid distribution. The objective of this Master thesis is to analyze the information contained in the PS seismic, and together with the PP seismic, derive Vp/Vs volumes for highlighting changes in lithology and pore-fluids. Rock physics, amplitude versus offset (AVO) analysis, including extended elastic impedance (EEI) reflectivity analysis, and simultaneous AVO inversion of PP and joint PP and PS data are used to describe the value of the converted waves seismic on exploration and reservoir characterization. The study area is on the southern part of the Oseberg South Field, eastern flank of the Viking Graben, northern North Sea. The AVO analysis of the PP data emphasizes changes in the pore-fluid content, whereas the PS data facilitates analyzing changes in the lithology. In addition, the joint inversion of PP and PS data delivers more accurate and detailed shear impedance estimates compared to the simultaneous PP AVO inversion. Therefore, the Vp/Vs data derived from the joint inversion of PP and PS data are useful for highlighting the reservoir sand and hydrocarbon distribution. This Master thesis underlines the potential benefits of including converted seismic waves in seismic interpretation. Quantitative seismic studies, including converted wave seismic, have not been published for the dataset provided for this thesis. Therefore, the results of this thesis could lead to enhanced reservoir characterization and potential reduction of economic risk in exploration and production activities in this area.

Table of Contents

List of Tables

List of Figures

1. INTRODUCTION

Seismic data are a description of the subsurface in terms of seismic reflections (i.e. changes in acoustic impedance) and are thereby dependent on seismic waves velocities and rock densities. Marine seismic data typically express changes in compressional (P) wave impedance but lack the information of changes in shear (S) wave impedance, as shear waves do not propagate through fluids. Shear waves, however, may deliver a better picture of subsurface structures. Since S-wave impedance also affects amplitude variations with offset (AVO), it is also important to consider the S-wave information when interpreting seismic data (Simm and Bacon, 2014). With new technology developed over time, the acquisition of S-waves has become possible.

Converted wave (PS) seismic can be acquired using ocean-bottom cable (OBC) technology. This makes possible to capture the energy of S-waves in addition to P-waves by arranging a grid of cables with receivers on the ocean floor (Barr, 1997). PS-waves propagate slower than PP-waves and hence provide a different, stretched representation of the subsurface in the time domain compared to PP-seismic. Therefore PS-waves should be converted to PP-time to compare the S-wave with the P-wave seismic section (Corcoran, 1989; Stewart et al., 2002).

1.1. OBJECTIVES AND MOTIVATION

The objective of this Master thesis is to analyze the information contained in converted wave (PS) seismic. Based on various methods (e.g. rock physics, AVO analysis, and seismic inversion) the effect and value of the combined use of PP- and PS-seismic are studied. This includes getting enhanced lithology and fluid information based on Vp/Vs, and determining the source of AVO effects in PP and PS (e.g. fluid or lithology). Converted wave studies have not been published for the dataset used in this thesis, which covers part of the Oseberg South Field. Consequently, this study can lead to enhanced exploration, reservoir characterization, and production in this area.

1.2. STUDY AREA

The Oseberg South Field is a producing oil and gas field located between the Viking Graben and the Horda Platform in the northern North Sea (**Figure 1.1**). The main reservoir level is the Middle Jurassic sandstone of the Tarbert Formation, defined by the first appearance of the shoreline sediments of the retrograding Brent delta (Helland-Hansen et al., 1992; Løseth et al., 2009). In addition to the Tarbert Fm. reservoirs, hydrocarbon is also present in the sandstones of the Cook and Ness Formations, and in the intra-sands of the Heather Formation. The study area is located in the southeastern part of the Oseberg South Field (**Figure 1.1**). The development of this structure was approved in 2003, and the production started in 2006 (NPD, 2018a).

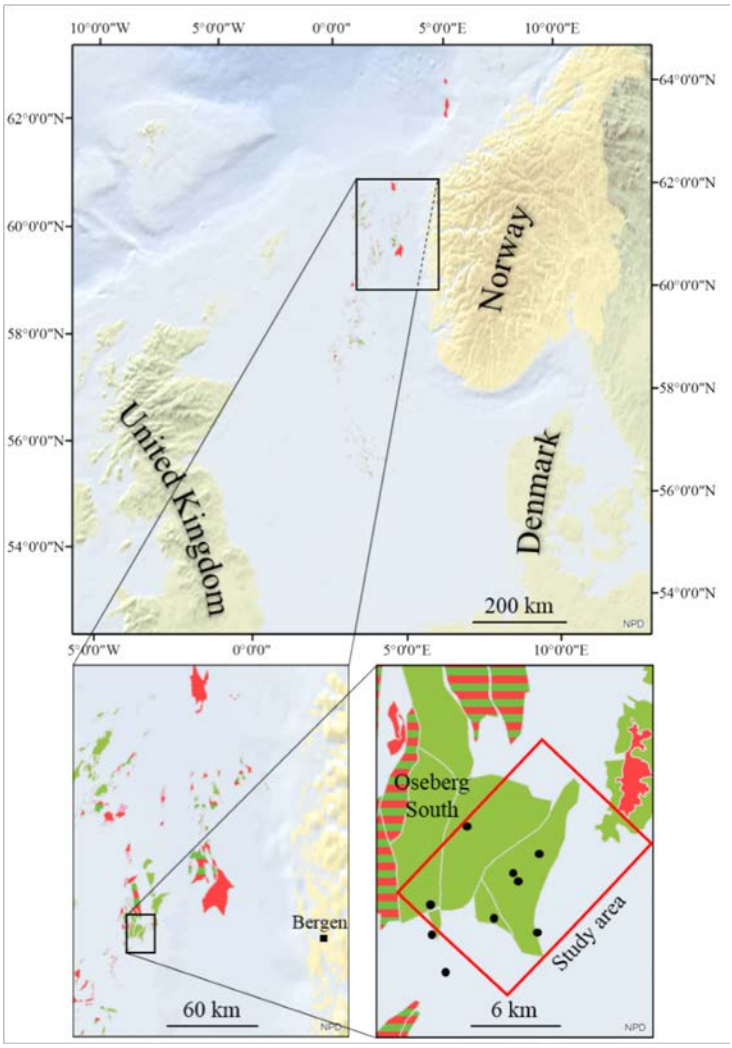

***Figure 1.1**: Location of the Oseberg South Field, study area (red square), available wells (black dots), and nearby fields (oil fields are in green and gas fields in red) (NPD, 2018b).*

1.3. BACKGROUND OF CONVERTED WAVES

Converted seismic waves (i.e. P-wave converted to S-wave at the reflectors) are used more and more in exploration of subsurface hydrocarbon targets for its different properties compared to compressional waves (e.g. no S-wave propagation through fluids). Granli et al. (1999), Stewart et al. (2003), and Xu (2011) describe a set of applications for the use of converted waves, which include detailed fault and horizon imaging, imaging of interfaces with low P-wave contrast but significant S-wave change, supplementing AVO inversion for density and velocity, and using Vp/Vs (ratio of P-wave to S-wave velocity) for lithology discrimination (e.g. sand/shale).

The S-wave propagates slower through the subsurface than the P-wave, hence the PS-seismic needs to be matched with the PP-seismic in order to be comparable. Another consequence of the differences in velocity between P- and S-waves is the asymmetric travel path of the converted wave (Stewart et al., 2002) (**Figure 1.2**). This is a major challenge for processing of the converted wave data.

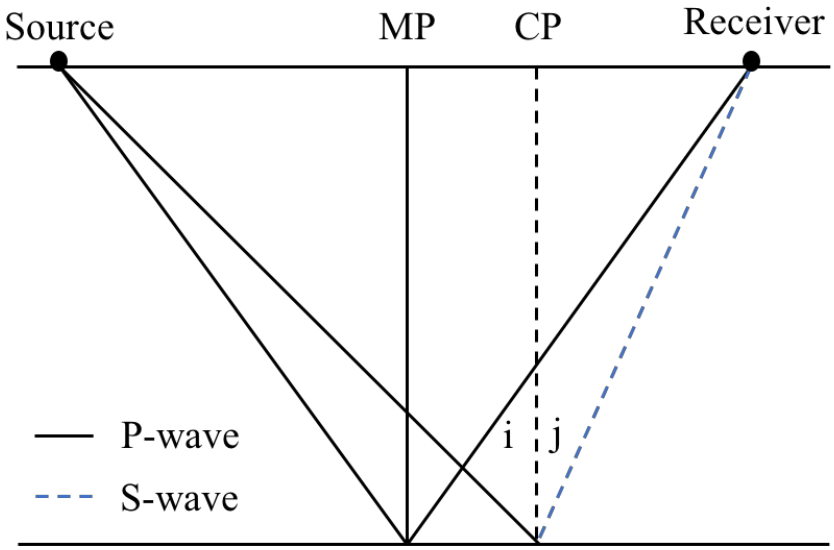

***Figure 1.2**: A converted wave (P-S) reflection at its conversion point (CP) compared to a pure P-wave reflection at its midpoint (MP). Modified after (Stewart et al., 2002). Incidence angle i is different from the reflection angle j for the converted wave.*

1.4. PREVIOUS WORK

Currently, few articles covering quantitative seismic studies of the Oseberg South Field have been published. However, similar studies have been conducted for other fields in the North Sea. Hanson et al. (1999) and MacLeod et al. (1999) presented the impact of the converted-wave seismic on the development and interpretation of the Alba Field in the UK part of the North Sea (**Figure 1.3**). Based on this study the converted wave data are now central to the well planning and geosteering processes in the Alba Field.

Later, Jenkinson et al. (2010) conducted a joint PP-PS angle-stack analysis and presented a workflow for AVA (amplitude versus angle) inversion of the Grane Field in the central part of the North Sea. The study of the Grane Field shows that the S-impedance inversion from a single input PS angle stack gives the best result for sand prediction (**Figure 1.4**).

More recently, Paydayesh et al. (2014) performed a joint PP-PS inversion based on a single well in the Oseberg South Field. This study shows that the joint PP-PS inversion provides more geological variation and detail in density and shear impedance than the estimates of elastic properties from the PP inversion alone (**Figure 1.5**).

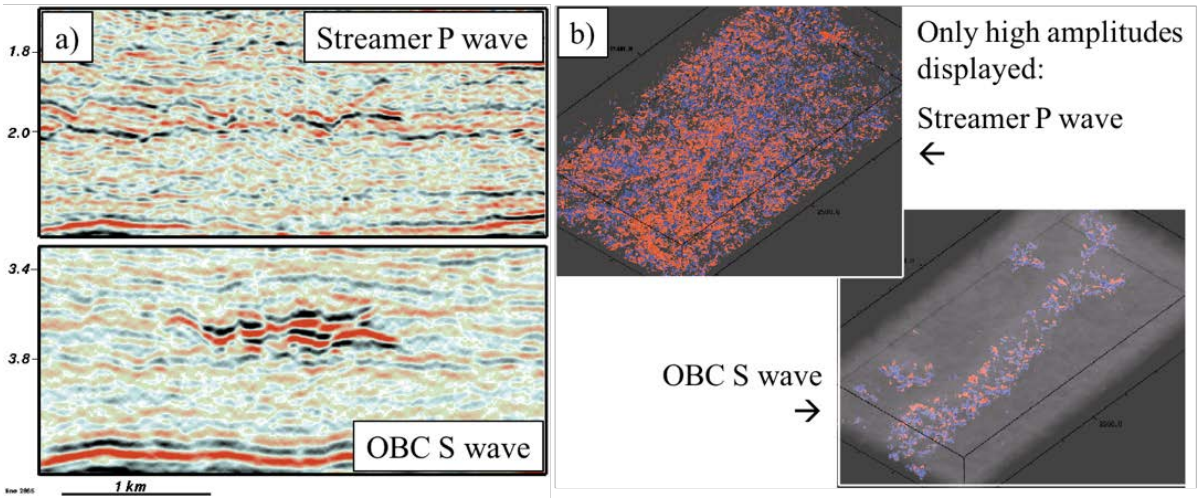

***Figure 1.3**: a) Converted wave data from the northern parts of the Alba Field showing dramatically improved imaging relative to the P-wave data. b) 3-D view of a sub-volume of the streamer and converted wave (OBC S-wave) data of the Alba Field, displayed with only the high amplitudes visible. The outline of the field is clearly seen in the converted wave data. Modified after (MacLeod et al., 1999).*

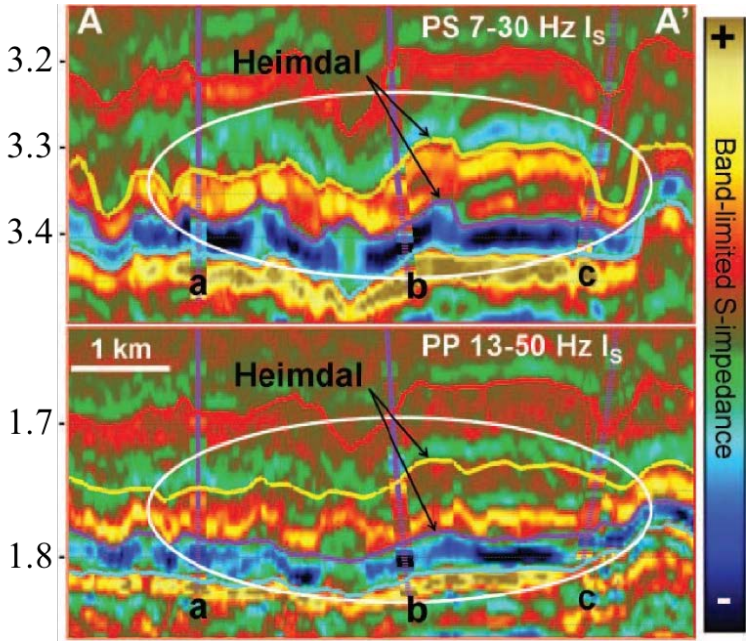

***Figure 1.4**: Vertical sections through three wells extracted from band-limited S-impedance inversion of PS and PP seismic data. The S-impedance from the PS inversion (top section) yields better contrast between sand and shale and a better tie to the wells than the S-impedance from the PP inversion (bottom section). Modified after (Jenkinson et al., 2010).*

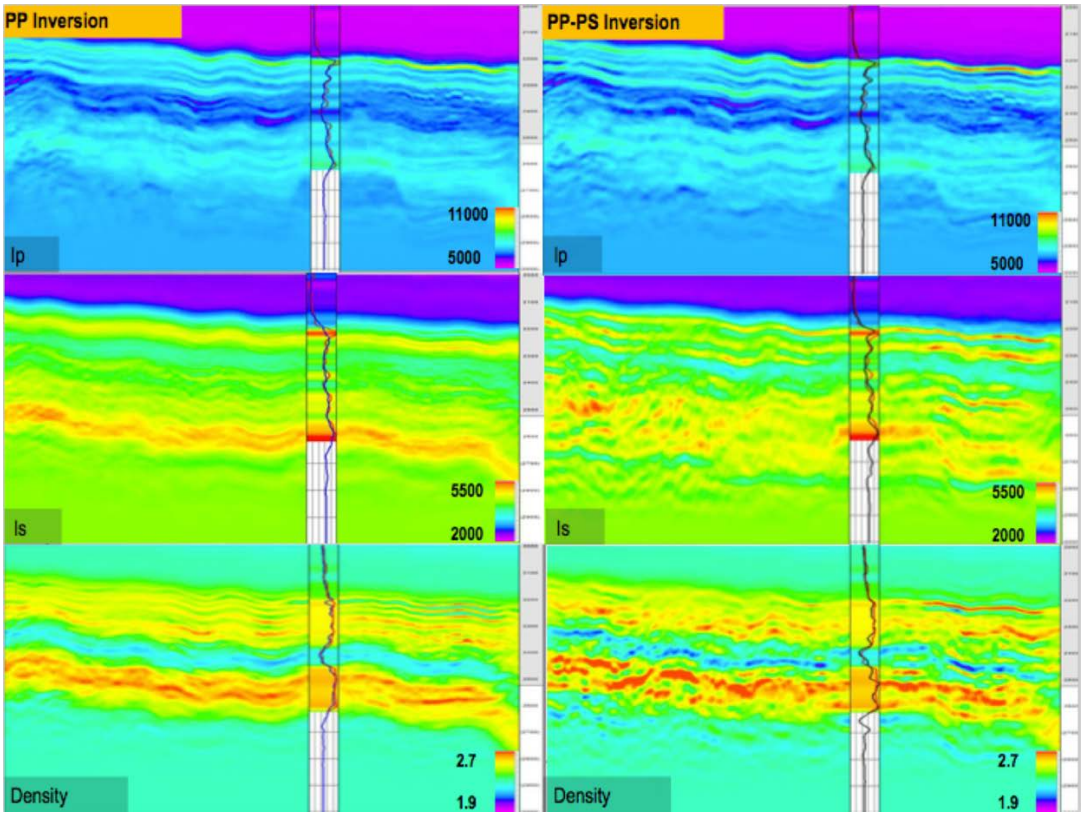

***Figure 1.5**: Acoustic impedance (Ip), shear impedance (Is), and density derived through inversion of PP and joint PP-PS seismic data in the Oseberg South field (Paydayesh et al., 2014).*

2. GEOLOGY OF THE AREA

This chapter summarizes the geology of the study area. Section 2.1 gives a brief description of the main tectonic events in the study area with associated lithostratigraphy. Section 2.2 describes relevant features in the reservoir and overburden.

2.1. STRUCTURAL AND STRATIGRAPHIC EVOLUTION

The Oseberg-Brage area is located on the eastern flank of the Viking Graben, northern North Sea (Figures 1.1 and 2.1). This region, as the remaining part of the Viking Graben, developed during at least two phases of rifting: Permian-Triassic and Middle Jurassic-Early Cretaceous (Badley et al., 1984; Badley et al., 1988; Gabrielsen et al., 1990; Steel and Ryseth, 1990; Yielding et al., 1992; Færseth, 1996; Ravnås and Bondevik, 1997; Færseth and Ravnås, 1998). Whereas the Permo-Triassic extension affected the total width of the northern North Sea, the Jurassic extension was concentrated mainly along the axis of the Viking and Sogn Grabens (Færseth, 1996) (Figures 2.1 and 2.2). The structural framework of the Oseberg-Brage area consists mainly of N-S and NE-SW striking normal faults formed during these phases of extension (Ravnås and Bondevik, 1997) (**Figure 2.1**).

2.1.1. PERMO-TRIASSIC

The central segment of the northern North Sea, bounded by the Øygarden Fault Complex to the east and the East Shetland Platform to the west, displays a Permo-Triassic full-graben below the Jurassic Horda Platform (Færseth, 1996; Færseth and Ravnås, 1998) (**Figure 2.2**a). The Brage East Fault, the eastern boundary of the Brage Horst, is mainly a Permo-Triassic feature, which separates the Permo-Triassic full-graben to the east and the Jurassic half-graben to the west (Færseth, 1996; Færseth and Ravnås, 1998) (Figures 2.1 and 2.2).

2.1.2. EARLY JURASSIC

Towards the end of the Triassic, a longer phase of post-rift thermal subsidence occurred (Løseth et al., 2009). Evidence of growth on the Oseberg and Brage faults during the Early Jurassic is shown by the stepwise, westward thickening of the Statfjord Formation and the Dunlin Group. However, within individual fault-blocks, the Statfjord Fm and Dunlin Gp are almost tabular (Ravnås and Bondevik, 1997; Færseth and Ravnås, 1998) (**Figure 2.2**b). The thickness

variations present in the footwalls indicate that faulting also triggered footwall uplift (Færseth and Ravnås, 1998).

2.1.3. MIDDLE JURASSIC

During the Middle Jurassic, the Viking Graben and its surroundings (i.e. Oseberg-Brage) were exposed to increased fault-related subsidence, documented by the increase in thickness over time of the Brent Gp relative to the underlying Dunlin Gp (Steel, 1993; Færseth and Ravnås, 1998). The Brent Gp, consisting of the Broom/Oseberg, Rannoch, Etive, Ness, and Tarbert Formations, marks the change from marine conditions (Dunlin Gp) to a more deltaic environment in this area (Helland-Hansen et al., 1992; Færseth and Ravnås, 1998). In addition, the Brent Gp is commonly defined as the top of the pre-rift sequence (Yielding et al., 1992; Færseth and Ravnås, 1998).

In the Oseberg-Brage area, the gradual transition to the main-rift, marked by rotational extensional faulting, is dated as Early Bajocian (Helland-Hansen et al., 1992; Ravnås et al., 1997; Færseth and Ravnås, 1998). From the Bajocian to the Bathonian, major fault activity shifted westward, making the Oseberg Fault less significant. However, the Brage Fault increased its activity, leading to the decoupling of the Oseberg Fault-Block from the Horda Platform (Ravnås et al., 1997; Færseth and Ravnås, 1998) (Figures 2.1 and 2.2). Movement along the N-S to NNW-SSE striking segments of the Brage Fault reached its climax in the Callovian and the Late Oxfordian-earliest Kimmeridgian, and experienced maximum footwall uplift at ca 60°30´N (Færseth and Ravnås, 1998) (**Figure 2.1**).

2.1.4. LATE JURASSIC

The NE-SW striking fault bounding the Oseberg Fault-Block in the southeast (within the seismic coverage area, **Figure 2.1**) is considered to be fairly inactive during the Early-Middle Jurassic extension. However, during the Kimmeridgian-Volgian, significant growth and footwall uplift were associated with this segment, which is regarded as a part of the Brage Fault (Færseth and Ravnås, 1998). The increasing impact of a NE-SW structural grain during the Late Jurassic coincides with the shift from the oxygenated mudstones of the Heather Fm to the anaerobic mudstones of the Draupne Fm (Færseth and Ravnås, 1998).

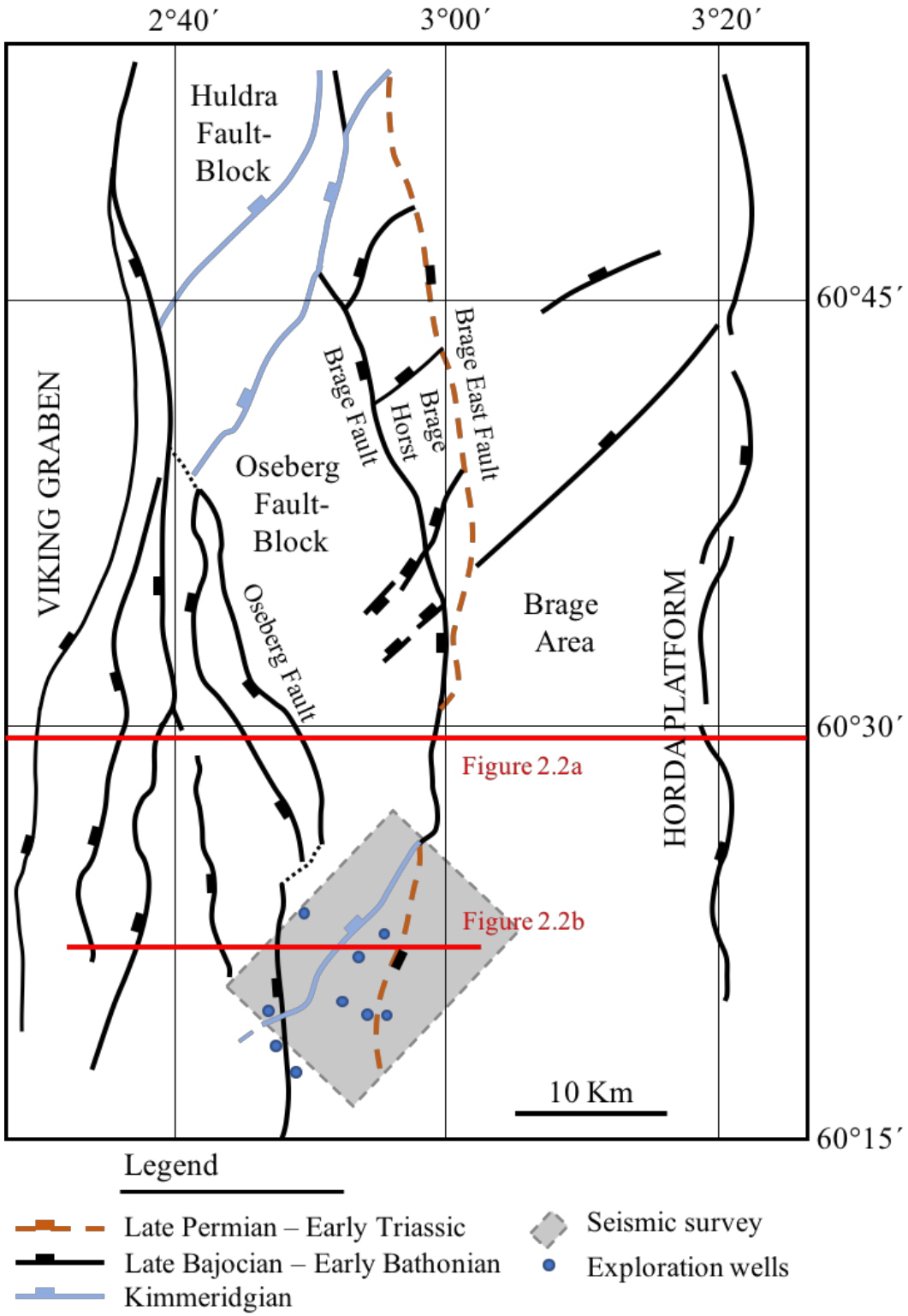

***Figure 2.1**: Structural map of the Oseberg-Brage area indicating the timing of fault initiation of the major normal faults (Færseth and Ravnås, 1998). Available exploration wells, seismic coverage area, and the location of the cross-sections in Figure 2.2 are highlighted in the map. Modified after (Ravnås and Bondevik, 1997; Færseth and Ravnås, 1998).*

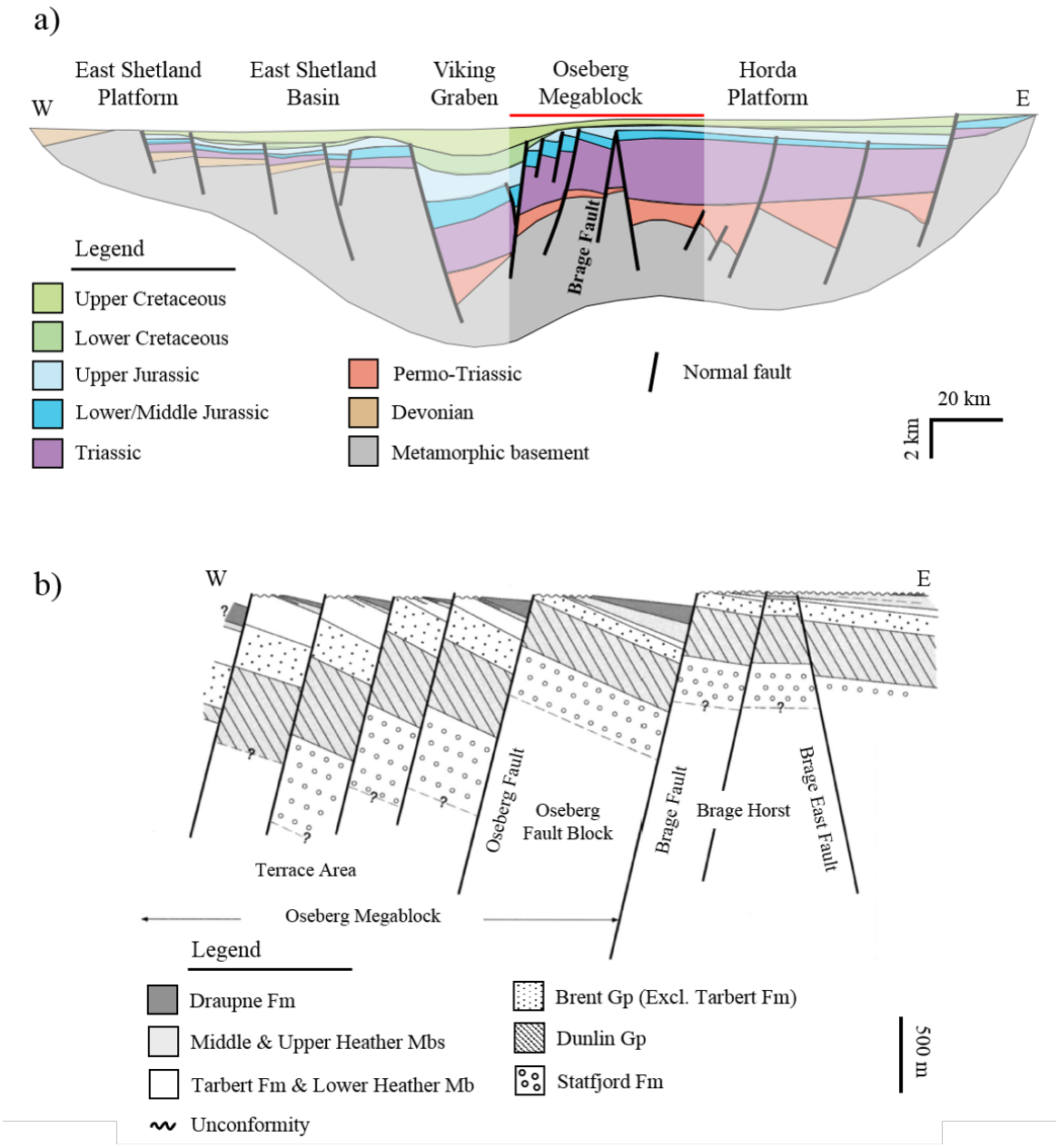

***Figure 2.2**: a) Cross-section showing Jurassic and Permo-Triassic major fault-blocks with related faults across the central segment of the northern North Sea at the end of Cretaceous time (Færseth, 1996). The red line (and the bright area beneath it) represents the area within the structural map in Figure 2.1. b) Schematic cross-section showing the strata deposited during the Jurassic (Færseth and Ravnås, 1998). Modified after (Færseth, 1996) and (Færseth and Ravnås, 1998), respectively. See Figure 2.1 for location of the cross-sections.*

2.2. RESERVOIR AND OVERBURDEN

2.2.1. RESERVOIR

The reservoirs in the Oseberg South area comprise several deposits of Jurassic age. Whereas the main reservoir units are in the Tarbert and Heather Formations, hydrocarbons are also present in the sandstones of the Cook and Ness Formations. The reservoirs in this area lie at a depth of 2 000–2 800 m (NPD, 2018a). The reservoir targets comprise a variety of depositional environments, including channel deposits, deltaic sequences with associated turbidites, and deep marine pelagic deposits (Fleming et al., 2007). The Middle Jurassic Tarbert Fm deposited during the retreat of the great Brent Delta, encompassing regressive-to-transgressive, coarsening-upward sandstone units (Helland-Hansen et al., 1992; Løseth et al., 2009).

2.2.2. OVERBURDEN

In some areas of the North Sea, irregular high-amplitude anomalies of Oligocene age can be identified (Dangerfield et al., 2010). These anomalies are carbonate-cemented sand injectites resulting from the intrusion of fluidized sand into fractures (Rodrigues et al., 2009). With a measured velocity of 5000 to 6000 m/s, compared to the background velocity of 2200 m/s, these anomalies causes a variety of problems (i.e. localized pull-up of deeper reflections, structural distortion and absorption of seismic energy) in the Oseberg area (Dangerfield et al., 2010; Mathewson et al., 2012) (**Figure 2.3**).

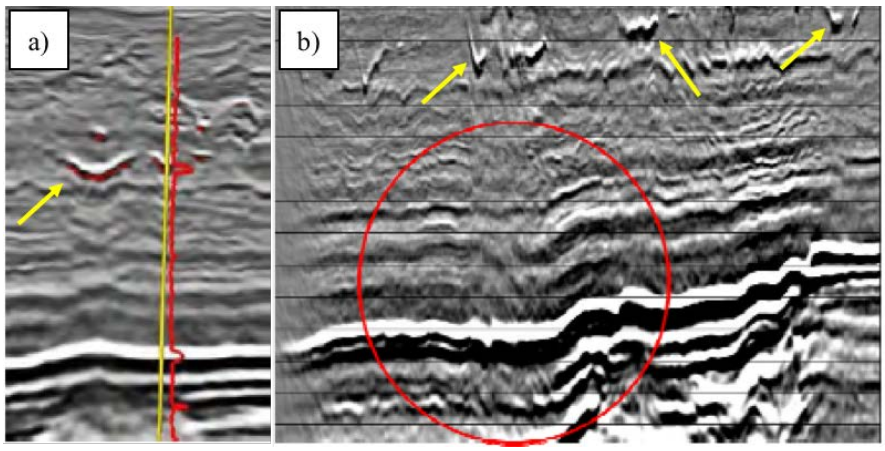

***Figure 2.3**: High velocity sand injectites (yellow arrows) with associated problems. a) Pull-up of deeper reflection. Sonic log (red track) measured along a well (yellow track) drilled through the anomaly indicating increase in velocity. b) Distortion and absorption of seismic energy beneath the Oligocene anomalies. Modified after (Mathewson et al., 2012).*

3. THEORY

This chapter provides a brief summary of the theory and concepts used in this thesis. Section 3.1 explains how compressional and shear wave velocities can be used to predict lithology and fluids through rock physics. Section 3.2 describes in detail the properties of converted waves. Sections 3.3 and 3.4 explain how this information is used to predict lithology and fluids at seismic scale through AVO analysis and inversion, respectively.

3.1. ROCK PHYSICS

Seismic data carry information about the subsurface rock and pore content in terms of travel time, reflection amplitude and phase variations. Seismic properties (e.g. Vp, Vs, and density) are affected by many factors such as pressure, temperature, porosity, saturation, type of fluid, etc. (Wang, 2001). In order to give a more detailed description of the subsurface reservoir characteristics, one has to understand how these factors are described by changes in the seismic properties. Rock physics integrates petrophysical, geomechanical, and seismic measurements, and consequently helps bridging the gap between the seismic properties and the elastic reservoir rock properties derived at the wells.

3.1.1. ELASTIC MODULI

In the theory of elasticity, the bulk modulus (K), shear modulus (μ), Young modulus (E), and Poisson´s ratio (v) are elastic parameters that describe different stress-strain relationships (e.g. in rocks) (**Figure 3.1**). In other words, the elastic moduli describe the object's resistance to be elastically (i.e. non-permanently) deformed.

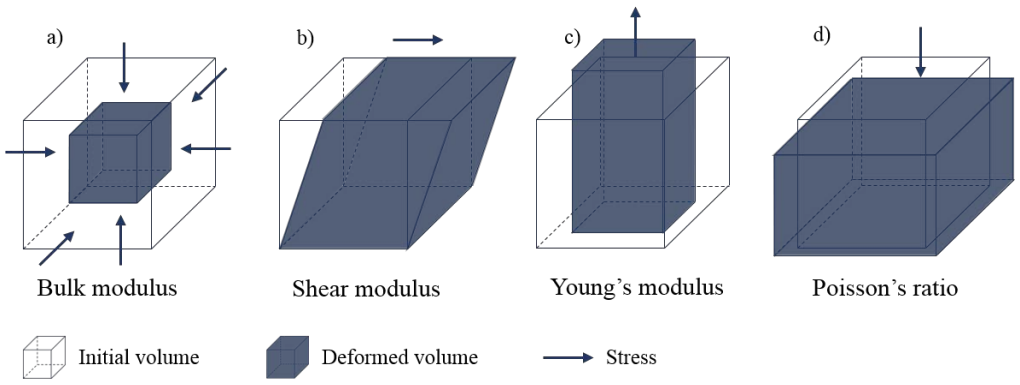

***Figure 3.1**: Elastic parameters. Volume and shape changes in rocks under stress. a) Bulk modulus, b) Shear modulus, c) Young's modulus, and d) Poisson's ratio.*

The bulk modulus *K*, also called incompressibility, represents the resistance of the material to change its volume under stress (**Figure 3.1**a). The bulk modulus relates hydrostatic stress (*P*) to volumetric strain (ε_V) as follows:

$$P = \frac{1}{3}(\sigma_{11} + \sigma_{22} + \sigma_{33}) = K(\varepsilon_{11} + \varepsilon_{22} + \varepsilon_{33}) = K_{\varepsilon_V} \quad (1)$$

where σ_{ii} and ε_{ii} are normal stress and strain, respectively. The indices represent the coordinate axes.

The shear modulus μ describes the resistance of the material to shear deformations (**Figure 3.1**b), and relates shear stress to shear strain in the following way:

$$\sigma_{ij} = 2\mu\varepsilon_{ij}, \qquad i \neq j \quad (2)$$

The Young modulus *E* is defined by a linear stress-strain relationship in a uniaxial stress state (e.g. with a normal stress component σ_{11}, and all other stress components equal to zero) (**Figure 3.1**c). The Young modulus is defined as:

$$\sigma_{11} = E\varepsilon_{11} \quad (3)$$

The Poisson´s ratio *v* describes the relation between the normal strain ε_{11}, caused by the applied stress σ_{11}, and the resulting normal strain in the orthogonal direction (**Figure 3.1**d). The Poisson´s ratio, which is a measure of incompressibility in porous rock, is defined as:

$$\nu = -\frac{\varepsilon_{22}}{\varepsilon_{11}} = -\frac{\varepsilon_{33}}{\varepsilon_{11}} \quad (4)$$

3.1.2. SEISMIC VELOCITY

In an isotropic elastic medium, the propagation velocities of compressional (P) waves α and shear (S) waves β are given by:

$$\alpha = Vp = \sqrt{\frac{K + \frac{4}{3}\mu}{\rho}} \quad (5)$$

and

$$\beta = Vs = \sqrt{\frac{\mu}{\rho}} \tag{6}$$

where K, μ, and ρ are bulk modulus, shear modulus, and bulk density, respectively.

3.1.3. IMPEDANCE

Seismic data typically describes the elastic properties in terms of acoustic impedance (Zp) and shear impedance (Zs) (in addition to density), where the acoustic impedance is:

$$Zp = \alpha\rho \tag{7}$$

and the shear impedance is:

$$Zs = \beta\rho \tag{8}$$

For normal incidence, the acoustic impedance alone determines the reflection coefficients. However, when an S- or P-wave strikes an interface at an angle other than 90 degrees, a mode conversion takes place. This means that the reflected energy of an incoming P-wave is split into an S-wave in addition to a P-wave.

3.1.4. LITHOLOGY AND PORE-FLUIDS

To distinguish between different lithologies, and to determine the fluid-content, it is important to know how seismic velocity and density are related. Several empirical relationships exist that relate seismic velocity to bulk density, for example Wang (2000). Based on a laboratory dataset containing more than 500 data points, Wang grouped sedimentary rocks based on lithology, and developed a set of relationships between bulk density, Vp (α), and Vs (β) (**Figure 3.2**).

Currently, dipole sonic logs, measuring both P- and S-waves, are commonly acquired in wells. The need to derive Vs from measured Vp is, however, still important, due to the lack of measured shear sonic logs in a lot of already developed fields (Wang, 2001). A well-known empirical relationship for compressional to shear velocities is the mudrock line established by Castagna et al. (1985).

Many AVO concepts (e.g. Smith and Gidlow (1987), discussing the so-called fluid factor; Whitcombe et al. (2002), discussing extended elastic impedance), and seismic inversion methods (e.g. Stewart (1990), joint inversion) exist, which assume that the Vp-Vs relationship described by Castagna et al. (1985) holds (see chapter 3.3 Seismic amplitude analysis and 3.4 Seismic inversion).

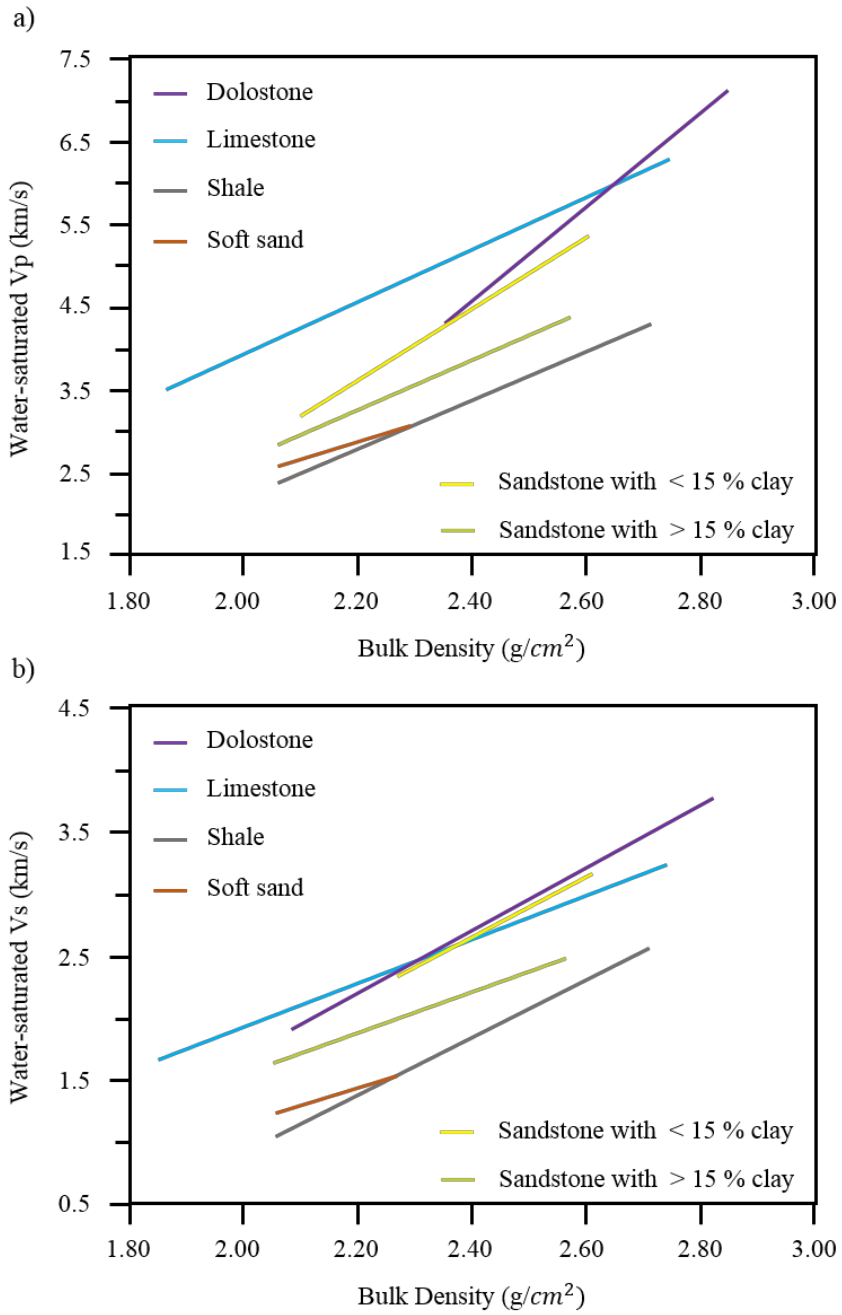

***Figure 3.2**: a) Vp and b) Vs, versus bulk density in sedimentary rocks. These relationships are based on a laboratory dataset consisting of more than 500 data points (Wang, 2000). Modified after (Wang, 2001).*

In terms of reservoir rocks, for a given porosity and pore aspect ratio spectrum, dolomite (dolostone) has the highest Vp, followed by limestone, sandstone, and unconsolidated (soft) sand (Wang, 2001) (**Figure 3.2**a). For the shear wave velocity, however, this ranking is different (**Figure 3.2**b). For clean sandstone (with < 15 % clay) the shear wave velocity is similar, or even higher, compared to dolomite and limestone (**Figure 3.2**b). Consequently, clean sandstone has lower Vp to Vs ratio, compared to the other reservoir rocks.

In terms of pore content, P-wave velocity in oil and gas is lower than in water. Consequently, P-wave velocity, which is dependent on bulk modulus, is sensitive to changes in the pore content. Shear waves, however, depend mainly on the shear modulus. As fluids cannot withstand shear deformation (μ = 0), S-waves will not propagate through fluids (Hamada, 2004). However, because of density of the pore fill, Vs will increase slightly with increasing hydrocarbon saturation (Ensley, 1985). Consequently, the ratio of Vp to Vs, is more sensitive to changes in the pore-fluid compared to the two velocities alone.

A standard way for discriminating different lithologies and different pore contents is cross-plotting the Vp/Vs ratio versus the acoustic impedance (**Figure 3.3**). The advantage of these two parameters is that often they can be derived reliably from elastic (AVO) inversion (see chapter 3.4 Seismic inversion) (Avseth et al., 2010). Rock physics templates (RPT) are often included in these cross-pots, which may help in discriminating between the different facies and identifying hydrocarbon (**Figure 3.3**).

The RPT's are based on different rock physics models, which relate elastic rock properties to various geological trends (e.g. Han et al. (1986), describing the effect of porosity and clay content on velocity, and Batzle and Wang (1992), describing the effect of temperature, pressure, and fluid composition on the density and velocity of pore fluids). Furthermore, these models are locally constrained by depth, mineralogy, fluid properties, and critical porosity (Avseth et al., 2010) (**Figure 3.3**). Critical porosity (i.e. 36 - 40 % for sandstone) is the porosity which separates consolidated, frame-supported rocks from fluid-supported suspensions, and therefore it is key in relating physical properties to porosity in rocks (Nur et al., 1998).

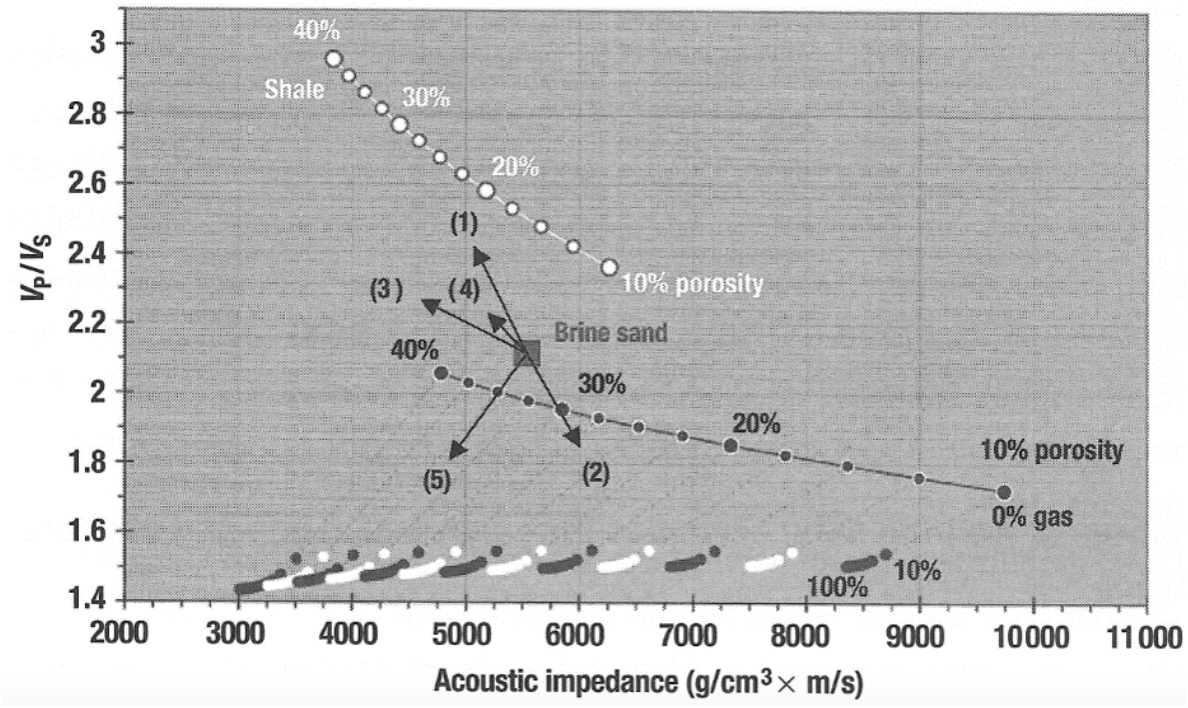

***Figure 3.3**: A rock physics template (RPT) presented as a cross-plot of Vp/Vs versus AI. Including rock physics models locally constrained by depth (i.e. pressure), mineralogy, critical porosity, and fluid properties. The template includes porosity trends for different lithologies, and increasing gas saturation for sands (assuming uniform saturation). The black arrows show various geological trends (conceptually): (1) increasing shaliness, (2) increasing cement volume, (3) increasing porosity, (4) decreasing effective pressure, and (5) increasing gas saturation. Adopted from (Avseth et al., 2010).*

3.2. CONVERTED WAVES

In seismic surveying, different types of seismic waves propagate through the subsurface and reflect back to the receivers. Converted waves use downward propagating P-wave energy, which converts and reflects back up as P-wave as well as S-wave energy from their deepest point of penetration (Stewart et al., 2003).

3.2.1. PROPAGATION

Two basic aspects control the propagation of PS-waves: 1) the asymmetric ray path defined by Snell's Law (**Figure 3.4**), and 2) the sinusoidal amplitude variations with offset described by the Zoeppritz equations (see section 3.3.1 Zoeppritz approximations) (Zoeppritz, 1919; Stewart et al., 2002; Xu, 2011). Snell's law describes the relationship between incidence, refraction (transmission), and reflection angles of waves entering a boundary of two different isotropic media, as follows:

$$\frac{\sin i}{\alpha} = \frac{\sin j}{\beta} \tag{9}$$

where i and j are the P- and S-wave angles of incidence and reflection, respectively. Because $\beta < \alpha$, angle j is smaller than angle i (**Figure 3.4**).

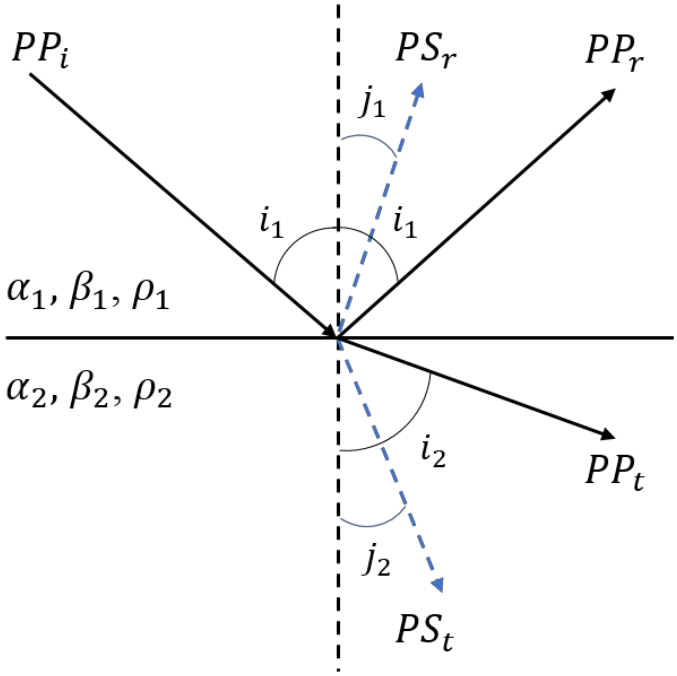

***Figure 3.4**: Incidence P-wave (PP_i) and its reflected P- and S-waves (PP_r and PS_r) and transmitted P- and S-waves (PP_t and PS_t). The parameters $\alpha, \beta,$ and ρ are corresponding to the properties of media 1 and 2. Modified after (Xu and Bancroft, 1997).*

In addition to the asymmetric ray path, the location of the P-to-S conversion point shifts from the receiver towards the asymptotic conversion point (ACP) with increasing depth (Stewart et al., 2002) (**Figure 3.5**). This is a result of different P-incidence and S-reflection angles for any source-receiver offset. This gives major problems for the processing of PS-seismic data compared to the processing of PP-seismic data, which is based on the common-midpoint assumption (Stewart et al., 2002).

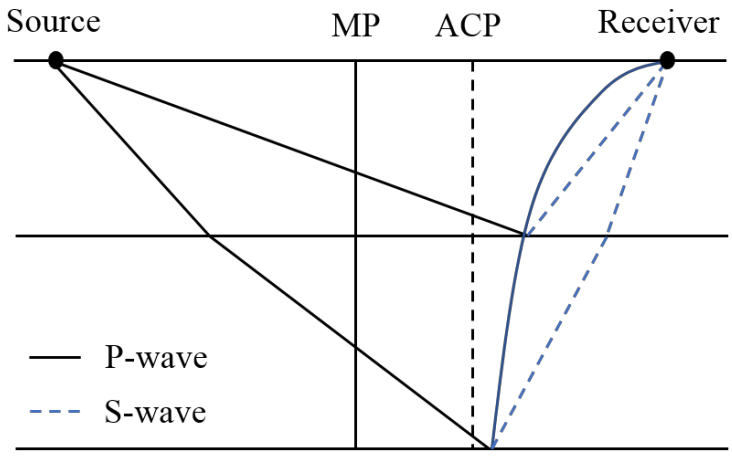

***Figure 3.5**: The P-S conversion point moves from the receiver along the asymptotic conversion point (ACP) trajectory with increasing depth. Modified after (Stewart et al., 2002).*

3.2.2. MEASURING S-WAVE PROPERTIES

S-wave images can be generated directly by S-wave sources (i.e. S-to-S-wave reflection). However, the S-wave images generated by traditional P-wave sources (i.e. converted wave images) are advantageous in many areas (Chan, 1998). Whereas the SS reflection data suffers from quite large shot and receiver statics, the PS data benefit from the relative low P-wave source statics. In addition, PS data often yield better resolution and, due to low-frequency noise generated by S-wave sources, also better signal-to-noise compared to the SS data (Garotta et al., 1990). On the other hand, due to the lower frequency range of S-waves relative to P-waves, the resolution of PP data is in general superior to that of the PS (and SS) (Stewart et al., 2002).

3.2.3. MATCHING OF PP AND PS EVENTS

S-waves propagate slower through the Earth compared to P-waves. Consequently, the PS reflections will appear at a different two-way-time (TWT) compared to the corresponding PP reflections. Therefore, to better compare the same event on both PP and PS seismic, their seismic sections need to be matched (Xu, 2011).

Several authors have derived different techniques for matching the PP- and PS-seismic events. Lawton and Howell (1992) used forward modeling to create PP and PS offset stacks for correlation. PP and PS seismic and synthetic stacks were then correlated individually and combined. For the purpose of investigating a productive, fractured interval in the Willesden Green region, central Alberta, Stewart et al. (1995) used PP and PS vertical seismic profiling

(VSP) data. The PP and PS sections were processed to depth and then converted back to P-wave time (Stewart et al., 2002). Subsequent, Gaiser (1996) developed a multicomponent correlation analysis to get Vp/Vs values. Later, Chan (1998) presented a method comprising of log-stretching the PP and PS time into the logarithmic time, before applying a bulk shift.

3.3. SEISMIC AMPLITUDE ANALYSIS

Reflectivity depends on the incidence angle of the propagating wave and the impedance contrast at the reflection boundary. For a normally incident wave, the reflection coefficient (R_c) is expressed as:

$$R_c = \frac{Z_2 - Z_1}{Z_2 + Z_1} \tag{10}$$

where $Z_1$and Z_2 are the impedance above and below the boundary, respectively. For non-normal (oblique) incidence, a pair of P and S waves is reflected at the interface (see **Figure 3.4**). The reflection coefficients for the two waves are described by the Zoeppritz's equations (Zoeppritz, 1919). These equations are complex and impractical in computations. Consequently, the need for linear approximations emerges.

3.3.1. ZOEPPRITZ APPROXIMATIONS

Many authors have derived linear approximations based on the Zoeppritz's equations. Bortfeld (1961) used Poisson's ratio (ν) to isolate the reflection coefficient into three terms: a normal incidence term, a fluid factor term, and a rigidity factor term. Later, Aki and Richards (1980) laid the ground for almost all the following approximations. The Aki and Richards approximation uses three terms to separate rock properties into density, compressional and shear velocities, and to calculate the reflection coefficient of the P-to-P (Rpp) and P-to-S (Rps) waves: The reflection coefficient of an incident P-wave to reflected P-wave is given by:

$$Rpp(i) = \frac{1}{2}(1 - 4\beta^2 p^2)\frac{\Delta\rho}{\rho} + \frac{1}{2\cos^2 i}\frac{\Delta\alpha}{\alpha} - 4\beta^2 p^2 \frac{\Delta\beta}{\beta} \tag{11}$$

and, the reflection coefficient of an incident P-wave to reflected S-wave is:

$$\mathrm{Rps(i)} = \frac{-\mathrm{p}\alpha}{2\cos \mathrm{j}}\left[\left(1 - 2\beta^2\mathrm{p}^2 + 2\beta^2 \frac{\cos \mathrm{i}}{\alpha}\frac{\cos \mathrm{j}}{\beta}\right)\frac{\Delta\rho}{\rho} - \left(4\beta^2\mathrm{p}^2 - 4\beta^2 \frac{\cos \mathrm{i}}{\alpha}\frac{\cos \mathrm{j}}{\beta}\right)\frac{\Delta\beta}{\beta}\right] \qquad (12)$$

where ρ, α, and β are the mean values of density, compressional and shear velocities, and $\Delta\rho$, $\Delta\alpha$, and $\Delta\beta$ are their differences. The ray parameter $p = \frac{\sin i}{\alpha} = \frac{\sin j}{\beta}$ (Snell's Law, Equation 9), where i is the incidence angle of the P-wave and j is the reflected angle of the S-wave (**Figure 3.4**). In these linear approximations, Aki and Richards (1980) assume small changes in elastic-wave properties across an interface. Also from the equations (and Snell's law) it is clear that $Rps(0) = 0$ and that there is no P-to-S conversion at normal incidence.

Smith and Gidlow (1987) compared modelled amplitudes using the Aki and Richards (1980) approximation with the reflection coefficients obtained from the Bortfeld (1961) approximation and the full Zoeppritz equation (**Figure 3.6**). These authors found that even with small changes of elastic properties across an interface, amplitude variations with angle of incidence (AVA) can be significant. For this comparison it is also important to note that the Aki and Richards approximation follows the full Zoeppritz equation from normal incidence until an incidence angle of 45 degrees.

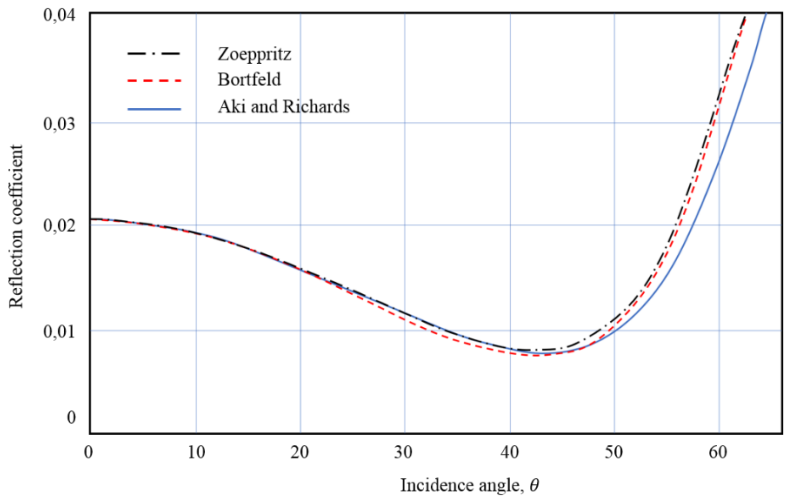

***Figure 3.6**: Reflection coefficient versus angle of incidence for a single interface. Comparison of the Aki and Richards (1980) approximation with the Bortfeld (1961) approximation and the exact Zoeppritz solution. Model: Vp_1 = 3000, Vs_1 = 1414, and ρ_1 = 2,40, and Vp_2 = 3100, Vs_2 = 1500, and ρ_2 = 2,42. Modified after (Smith and Gidlow, 1987).*

Based on the equation (11) of Aki and Richards, Shuey (1985) separated the compressional wave reflection coefficient into three terms, intercept (A) (describing the amplitude at normal incidence), gradient (B), and curvature (C):

$$R(\theta) \approx A + B \sin^2 \theta + C \sin^2 \theta \tan^2 \theta \tag{13}$$

where θ is the angle of incidence. The Shuey three-term equation (13), can also be expressed by the two first terms, but it is then only valid for the incidence angle at which it deviates from the three-terms and the full Zoeppritz equation (Simm and Bacon, 2014) (**Figure 3.7**).

$$R(\theta) \approx A + B \sin^2 \theta \tag{14}$$

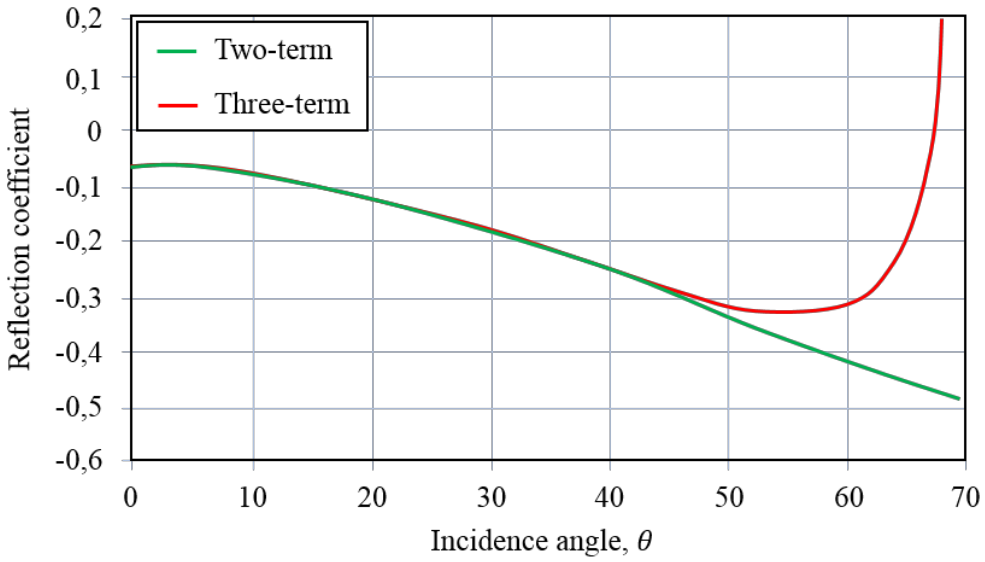

***Figure 3.7**: Comparison of the Aki and Richards (Shuey) two-terms and three-terms equations for an interface of shale overlying a gas sand. Model: shale: Vp_1 = 2438, Vs_1 = 1006, and ρ_1 = 2,25, and gas sand: Vp_2 = 2600, Vs_2 = 1700, and ρ_2 = 1,85. Modified after (Simm and Bacon, 2014).*

More approximations can be found in the literature e.g. (Chapman, 1976; Fatti et al., 1994; Hilterman, 2001). Most of them are based on the approximations derived by Aki and Richards (1980). The methods used in this thesis are based on the Aki and Richards and the Shuey two-term approximations given by equations (11), (12), and (14).

3.3.2. AVO ANALYSIS

Amplitude versus offset (AVO), or amplitude versus angle (AVA) analysis was primarily proposed as a method for confirming amplitude anomalies (e.g. bright spots) associated with gas sands (Ostrander, 1984). The work of Ostrander is based on Koefoed (1955), who found that a significant Poisson's ratio contrast between two media could have a large impact on the P-wave reflection coefficient with increasing offset. Gas sands, proven to have particularly low Poisson's ratio, embedded by "normal" Poisson's ratio sediments, should then result in an amplitude anomaly with increasing offset (Ostrander, 1984).

Based on AVO characteristics, Rutherford and Williams (1989) grouped the gas-sand reflectors into three classes defined by the reflection coefficient at zero incidence (R(0), intercept) at the top of the gas sand zone (**Figure 3.8**). Class I consists of high-impedance sands, class II and IIp consists of near-zero impedance contrast sands, and class III comprises the low-impedance sands. Later, Castagna et al. (1998) highlighted a fourth class of sand (class IV) where the reflection coefficient becomes more positive, but decrease in magnitude with increasing offset (**Figure 3.8**). For the classes defined by Rutherford and Williams (1989), the base gas-sand reflections tend to fall above a background trend (i.e. brine-saturated sandstones and shales) in an AVO intercept (A) and gradient (B) cross-plot, whereas the top gas-sand reflections tend to fall below it (Castagna et al., 1998) (**Figure 3.8**b).

Based on the equations of Aki and Richards, Smith and Gidlow (1987) presented a weighted-stacking method to create a pseudo-Poisson's ratio reflectivity (Rv) and a fluid factor (ΔF) stack for the detection of gas. In non-mathematical terms, the ΔF is defined as the distance away from the mudrock line defined by Castagna et al. (1985) (**Figure 3.9**). This difference should be attributed to fluid/gas anomalies.

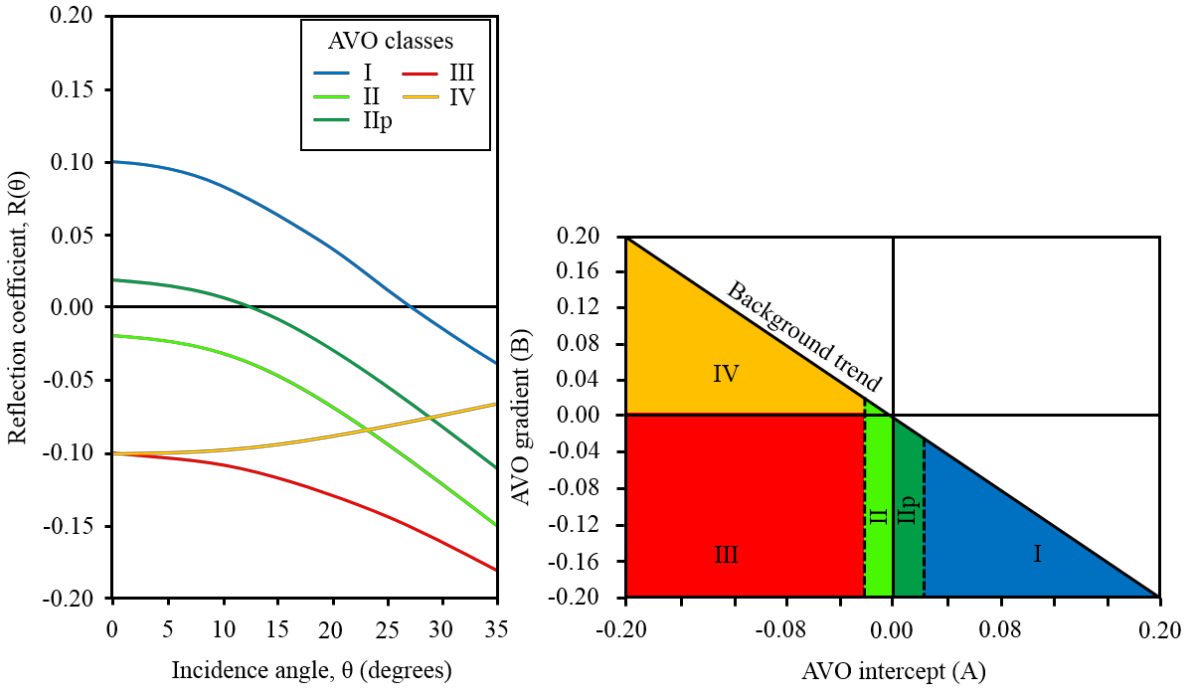

***Figure 3.8**: AVO classification. a) Reflection coefficients as function of incidence angle at the gas sand top showing the different classes defined by Rutherford and Williams (1989). b) AVO intercept (A) versus gradient (B) cross-plot showing the same gas sand classes. Top of gas sand reflections tend to fall below the background trend (brine-saturated sandstones and shales). Modified after (Rutherford and Williams, 1989; Castagna et al., 1998).*

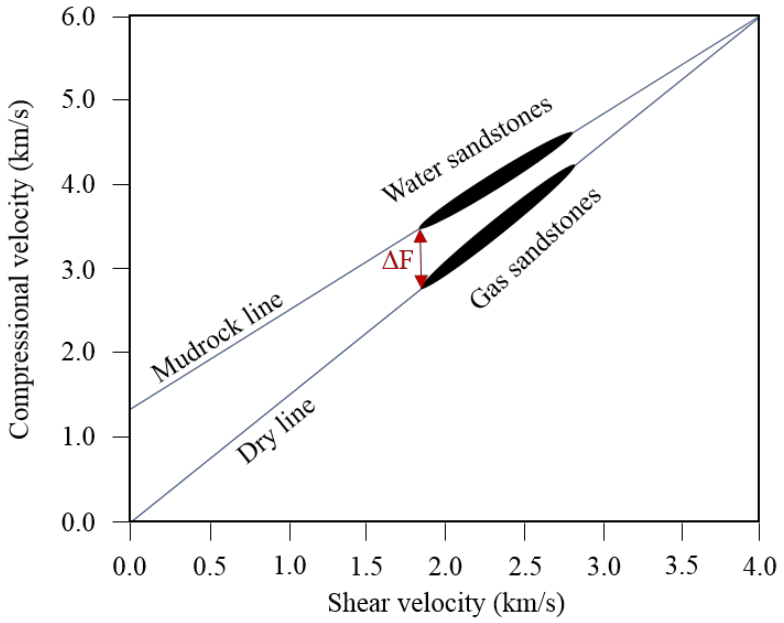

***Figure 3.9**: Shear velocity versus compressional velocity, showing the trends for water-saturated (mudrock line) and dry (dry line) sandstones. Smith and Gidlow (1987) fluid factor (ΔF) is defined as the distance away from the mudrock line. Modified after (Castagna et al., 1985) and (Fatti et al., 1994).*

Later, Smith and Gidlow (2003) introduced the Fluid Factor Angle, which is defined as the angle of incidence for which the background (i.e. brine-saturated clastics) reflection coefficients are zero (i.e. in the Shuey (1985) two-term equation (14)). However, the fluid factor could also be considered as the combination of intercept and gradient which will produce a zero (intercept) result for the background trend (i.e. the fluid line, **Figure 3.10**) (Smith and Gidlow, 2003). Consequently, the Crossplot Angle (φ), which is the angle that the fluid line makes with the intercept in an intercept-gradient (A-B) cross-plot, was introduced (**Figure 3.10**).

In **Figure 3.10** one can see some effects of changes in the reservoir properties (i.e. porosity and fluid compressibility) on AVO response for normal polarity data (i.e. positive sample corresponds to an increase in acoustic impedance) (Foster et al., 2010). An increase in pore-fluid compressibility displaces the reflection response away from the fluid line, whereas an increase in porosity moves the reflection response parallel to the fluid line (Foster et al., 2010) (**Figure 3.10**).

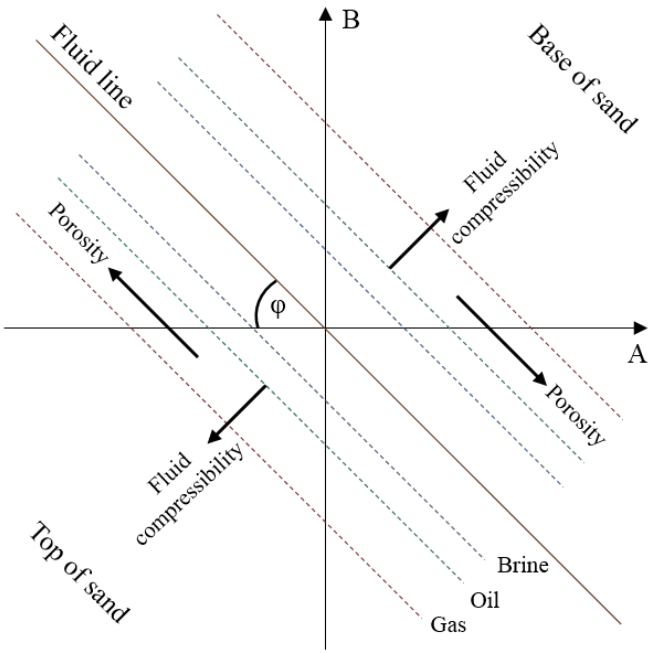

***Figure 3.10**: Effects of changes in reservoir properties in an intercept-gradient (A-B) cross-plot. An increase in pore-fluid compressibility displaces the reflection response away from the fluid line, whereas an increase in porosity moves the reflection response parallel to the fluid line (Foster et al., 2010). Highlighted is also the crossplot Angle (φ) described by Smith and Gidlow (2003), which produces a zero result for the background trend (i.e. fluid line). Modified after (Foster et al., 2010).*

The intercept and gradient, which can be estimated (see (Castagna et al., 1998)) using Shuey (1985) two- or three-term equations (13) and (14), can together produce several AVO attributes (e.g. AVO product, AVO sum and AVO difference). The objective of these attributes is to maximize the distinction between fluid types. The AVO product (intercept * gradient) will show a positive anomaly only for AVO classes II and III (see **Figure 3.8**) at the top and base of the reservoir. The fluid factor, however, will theoretically work for all the AVO classified gas sands, as it describes the deviations from the background trend (Smith and Gidlow, 1987; Castagna et al., 1998).

3.3.3. ELASTIC AND SHEAR WAVE ELASTIC IMPEDANCE

Connolly (1999) introduced the elastic impedance (EI) (later normalized by Whitcombe (2002)) as a generalization of acoustic impedance for non-normal incidence, facilitating the inversion of angle stacks in addition to full-stack data (see chapter 3.4 Seismic inversion). In the same paper, Connolly, also suggested that EI values are more uniform than AI values for a given lithology. Equivalent to the EI, shear-wave elastic impedance (SEI) was derived by Duffaut et al. (2000) with the purpose of linking the converted wave stacks to wells using a linearization of the Zoeppritz equations.

3.3.4. EXTENDED ELASTIC IMPEDANCE

Whitcombe et al. (2002) introduced an extension of the EI concept called extended elastic impedance (EEI). They replaced $\sin^2\theta$ by $\tan\chi$ in Shuey (1985) two-term equation (15), before scaling this equation by $\cos\chi$, to allow any combination of the intercept and gradient as an extension of the EI:

$$\mathrm{Rs}(\chi) = \mathrm{A}\cos\chi + \mathrm{B}\sin\chi \tag{15}$$

where *Rs(*χ) is scaled reflectivity, A and B are intercept and gradient, respectively, and χ (chi) is the angle of rotation in the A-B space (**Figure 3.11**). The scaled reflectivity ranges from a value of A at χ = 0 (zero incidence reflectivity) to a value of B at χ = 90 (gradient reflectivity) (Whitcombe et al., 2002). The extended elastic impedance equivalent to equation (15) is:

$$EEI(\chi) = \alpha_0\rho_0[(\frac{\alpha}{\alpha_0})^p(\frac{\beta}{\beta_0})^q(\frac{\rho}{\rho_0})^r] \quad (16)$$

where α, β, ρ are P-wave velocity, S-wave velocity, and density, respectively, and α_0, β_0, ρ_0 are constants (e.g. averages of α, β, ρ) (Whitcombe, 2002). Furthermore, $p = (\cos\chi + \sin\chi)$, $q = -8K\sin\chi$, and $r = (\cos\chi - 4K\sin\chi)$, where K is the average (β_n^2/α_n^2) over the interval n of interest (Whitcombe, 2002). Whitcombe et al. (2002) demonstrated that the EEI could be tuned (using different χ values) to make it approximately proportional to elastic parameters (e.g. acoustic impedance, bulk modulus, Vp/Vs ratio, shear impedance, shear modulus, etc.).

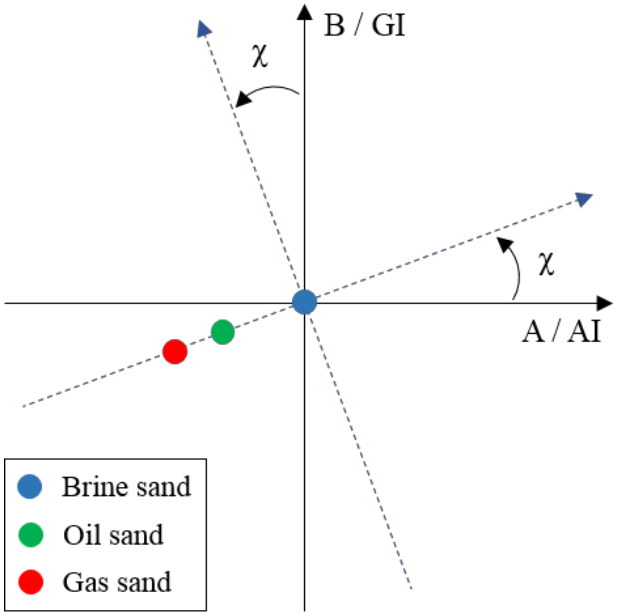

***Figure 3.11**: Rotation in the intercept-gradient (A-B) (or the impedance (AI-GI)) space using angle χ (chi). This particular rotation maximizes the distinction between brine, oil, and gas sands and is equivalent to the Smith and Gidlow (2003) crossplot angle. Modified from (Simm and Bacon, 2014).*

Using the logarithmic relationship between reflectivity and impedance (Simm and Bacon, 2014), A and B can be replaced by ln(AI) (acoustic impedance) and ln(GI) (gradient impedance), respectively, to move from the reflectivity intercept-gradient (A-B) domain to the impedance (AI-GI) domain, maintaining the same angular relationship (**Figure 3.11**). By defining $AI_0 = \alpha_0\rho_0$, equation (17) can be written as:

$$EEI(\chi) = AI_0[(\frac{AI}{AI_0})^{\cos\chi}(\frac{GI}{AI_0})^{\sin\chi}] \quad (17)$$

where EEI (χ = 0) is equivalent to acoustic impedance (AI) and, EEI (χ = 90) is equivalent to gradient impedance (GI) (Whitcombe et al., 2002).

Typically, the EEI procedure involves a rotation in the intercept-gradient (A-B) space (see **Figure 3.11**), providing the best correlation coefficient with a specific log (e.g. water-saturation and gamma-ray, **Figure 3.12**), to generate the equivalent intercept-gradient combination (i.e. the EEI) (Whitcombe et al., 2002). In addition, Whitcombe et al. showed that this approach allowed defining a single function (i.e. equations (16) or (17)) that is proportional to many elastic parameters (e.g. bulk modulus, K $\propto$ EEI(χ = 12.4°), and Vp/Vs $\propto$ EEI(χ = 45°)). Having in mind the effect of pore-fluid compressibility (**Figure 3.10**) on the intercept-gradient (A-B) cross-plot, a tuning of the EEI to the bulk modulus, should lead to a maximized fluid distinction. Similarly, a tuning of the EEI to the Vp/Vs should optimize lithology and fluid discrimination. Consequently, the EEI could be optimized to highlight changes in the fluid or lithology.

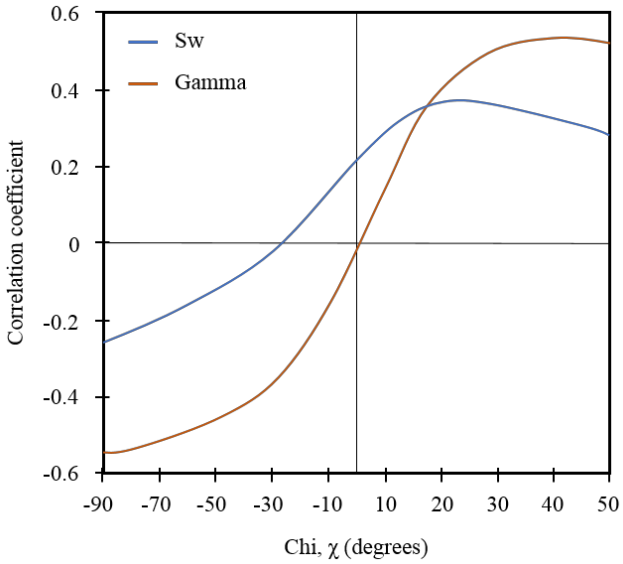

***Figure 3.12**: Correlation coefficient between EEI and gamma-ray and Sw (water-saturation) for a range (-90 to 90 degrees) of χ (chi) values. Modified from (Whitcombe et al., 2002).*

3.4. SEISMIC INVERSION

Overall there are two types of seismic inversion, deterministic and stochastic (Simm and Bacon, 2014). Quite a number of different approaches to deterministic seismic inversion exist (e.g. recursive inversion, sparse spike inversion and model-based inversion). A range of these approaches are discussed by Russell (1988). In general, seismic inversion is defined as the process of deriving from the seismic data the elastic rock properties (e.g. acoustic impedance, shear impedance). Thus, the final goal of inversion is to move from the reflectivity domain of the seismic to reliable estimates of layer elastic properties (**Figure 3.13**). Some of the benefits of inverted data can be simplified stratigraphic relationships and more interpretable lithological and fluid/gas effects, attributed to the introduction of layers instead of reflections (Simm and Bacon, 2014).

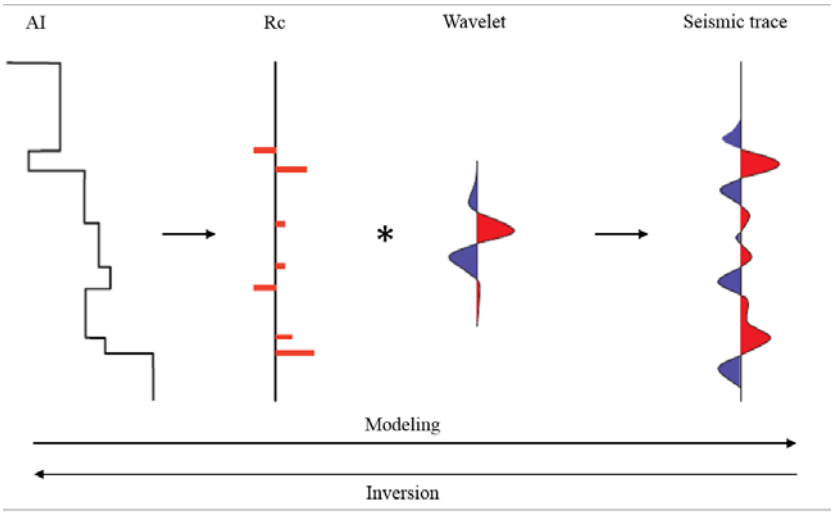

***Figure 3.13**: Process of forward modeling (left to right) versus seismic inversion (right to left). In the process of inversion, a wavelet is extracted from the seismic before the seismic is deconvolved. Resulting in reflection coefficients (Rc) and eventually relative acoustic impedance. If absolute acoustic impedance is the goal, a low-frequency model/trend has to be added. Modified after(Simm and Bacon, 2014).*

Seismic reflectivity data are band-limited (i.e. bound within a range of frequencies), and typically lack high and low frequencies (**Figure 3.14**). Consequently, to estimate absolute values of rock properties through inversion, one must include a background low frequency model (LFM). The missing low frequency component is derived from the well log data (**Figure 3.15**a), and is used to add trend and accuracy, and to constrain the resulting impedance. It is

important to be aware of the influence of the low frequency background model on the final inversion results, as it may introduce artefacts, not representative of the geology (e.g. Francis and Syed (2001), **Figure 3.15**) (Simm and Bacon, 2014).

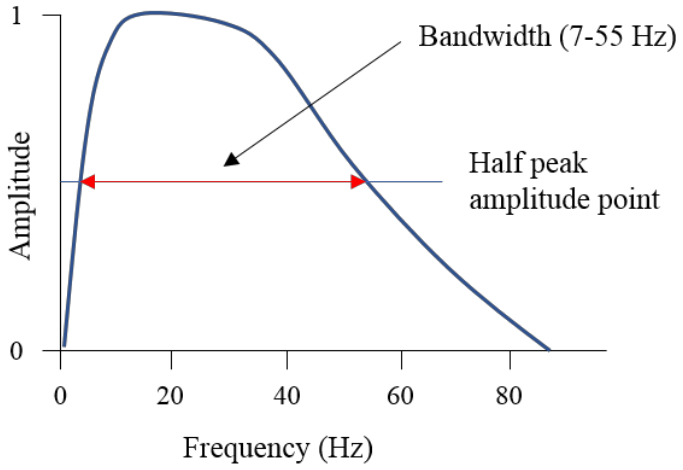

***Figure 3.14**: Typical normalized amplitude spectrum of seismic data. A common threshold for the bandwidth is half the peak amplitude (Simm and Bacon, 2014). Seismic reflectivity data lacks high and low frequency content. Modified after (Simm and Bacon, 2014).*

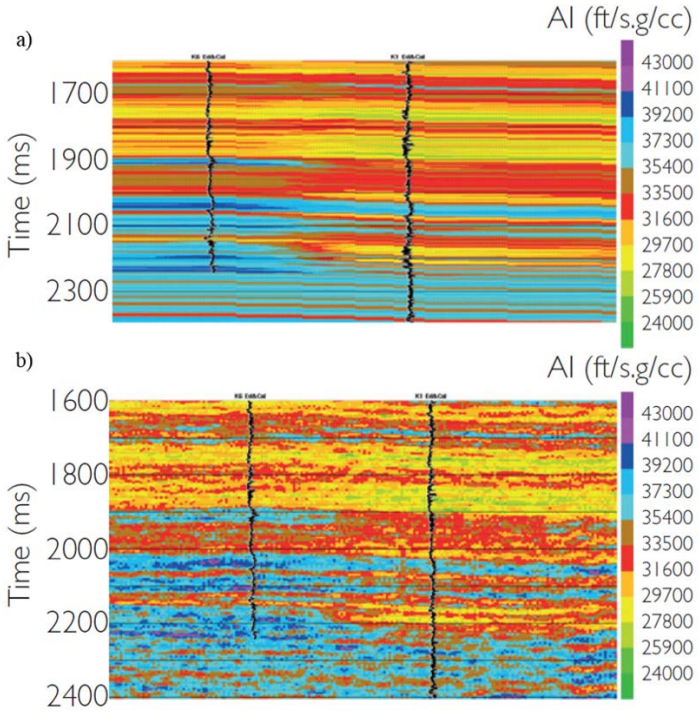

***Figure 3.15**: An example of the influence of the background model on the final inversion results (Francis and Syed, 2001). a) Background low frequency model (LFM) based on interpolated well data. b) Final inversion result, highly influenced by the background model. Modified after (Simm and Bacon, 2014).*

For the deterministic approach to the seismic inversion, it is important to be aware of how the different components affect the final result. Consequently, some questions (e.g. related to the wavelet, well tie and background model) arise, that should be answered prior to the interpretation of the inversion results. Typical questions can be how well the wavelet is understood (particularly its phase), how good is the match between well synthetics and the seismic (e.g. at the targeted reservoir level), and if the background model is a potential source of bias in the impedance values (Simm and Bacon, 2014).

Once these questions have been answered, the inversion results should be quality checked against the well log and the seismic data. Typically, the final impedance section is compared against well impedance (upscaled to seismic) to see how good they match e.g. (Bach et al., 2000) (**Figure 3.16**).

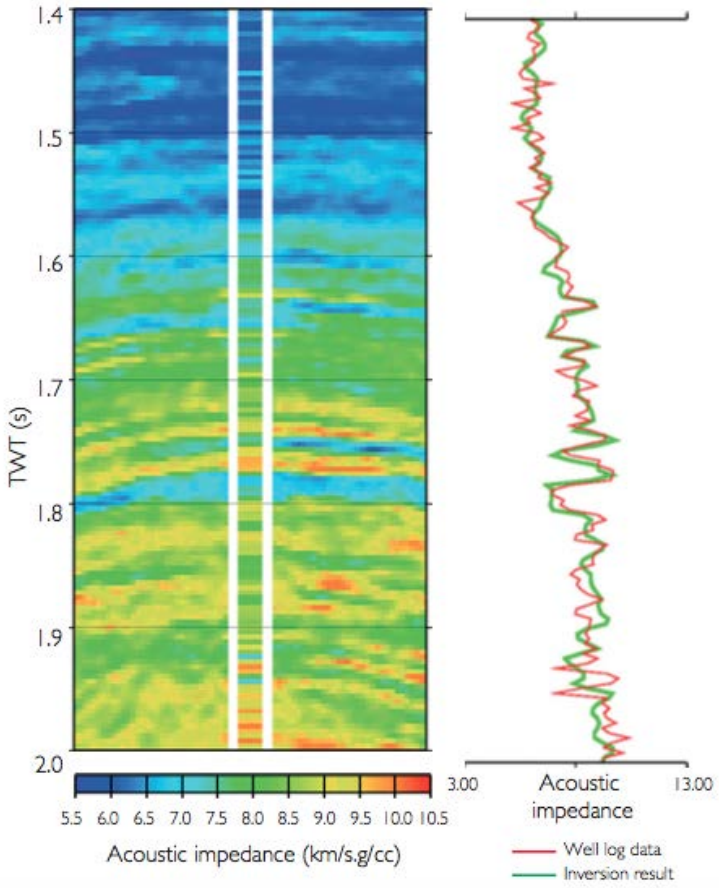

***Figure 3.16**: A good match is observed between the acoustic impedance derived from the AVO inversion (green curve) and the acoustic impedance measured in the well (red curve). Modified after (Bach et al., 2000).*

3.4.1. MODEL-BASED INVERSION

A common approach to the inversion of seismic data is model-based inversion (**Figure 3.17**). This inversion uses an iterative forward modelling technique, followed by a comparison procedure (i.e. of modelled trace and seismic trace) to build a final impedance model (Veeken and Da Silva, 2004; Simm and Bacon, 2014). A starting (low frequency) model based on log data and guided by the seismic horizons, together with an extracted wavelet give a modelled trace. The modelled trace is subsequently checked against the seismic trace to minimize errors (Simm and Bacon, 2014). The initial model is updated, and the process is repeated until the error is sufficiently small. Finally, the final impedance model is created.

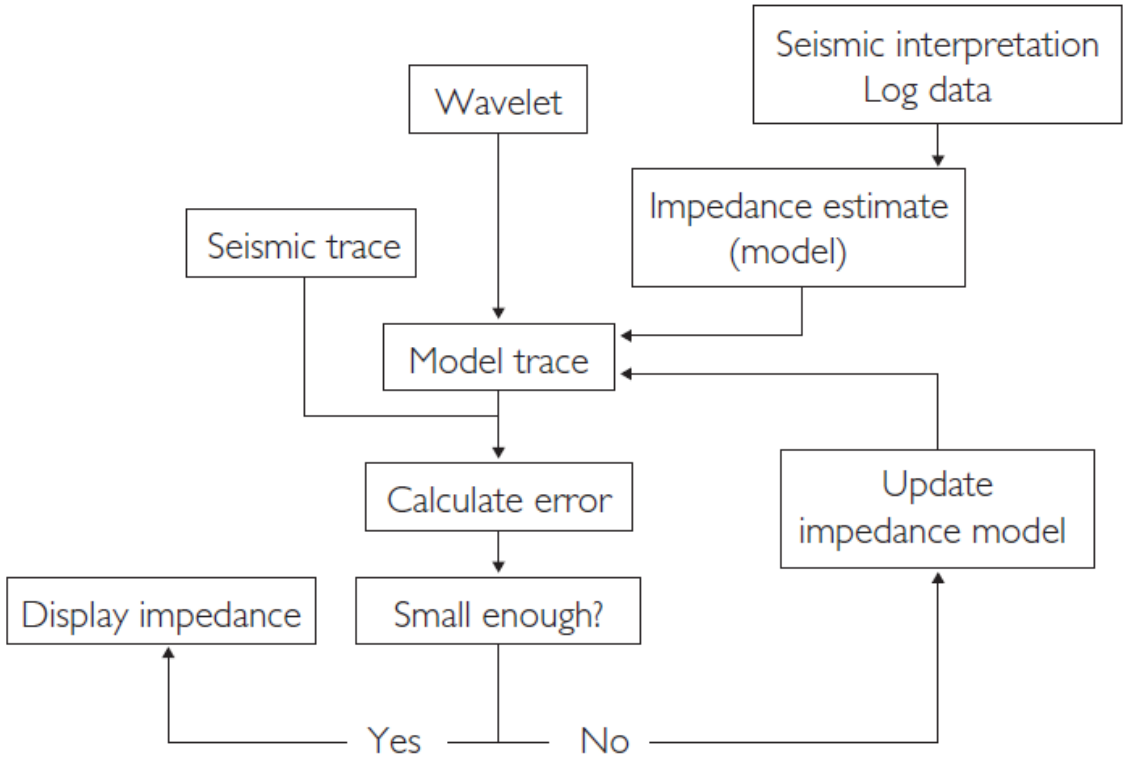

***Figure 3.17**: Model-based inversion flow-chart. An initial impedance (low frequency) model, based on log data and guided by the horizons, and an extracted wavelet serve as input to create a modelled trace. The modelled trace is compared with the seismic trace, and if the error is small enough the final impedance is displayed. If not, the impedance model is updated, and the process is repeated until a small error is reached. Adapted from (Simm and Bacon, 2014).*

3.4.2. PRE-STACK SIMULTANEOUS INVERSION

Most of the methods already mentioned, are based on post-stack seismic data to get acoustic impedance. However, to obtain estimates of shear impedance and density, in addition to acoustic impedance, one has to consider offset-dependent reflectivity data (i.e. angle stacks). Note that inverting the seismic for the bulk density is quite difficult, due to its small contribution to the overall seismic amplitude, which is only present on large angles (beyond 40°) (Francis, 2013; Simm and Bacon, 2014).

Simultaneous AVO inversion is a pre-stack inversion method for estimating P-wave velocity, S-wave velocity, density, and the combinations of these (i.e. impedances and Vp/Vs ratio) (**Figure 3.18**). Similar to the model-based post-stack inversion mentioned above, this method includes an optimization procedure. The starting model is updated until the mismatch between its resulting synthetic angle stacks and the input seismic angle stacks is small enough. The result of each iteration is a P-impedance, S-impedance, and density cube derived from the prior models (LFM) of Vp, Vs, and density (or impedances and density). Subsequently, based on these cubes the reflectivity as a function of angle is calculated using an approximation of the Zoeppritz equation. The reflectivity cube is then convolved with a wavelet. The resulting synthetic angle stacks (modelled amplitudes) are then compared with the measured angle stacks (Francis, 2013; Simm and Bacon, 2014). If the error is small enough, the synthetic angle stacks and the impedance cubes are accepted (**Figure 3.18**).

The challenge of deriving reliable estimates of these elastic rock properties through inversion has been discussed by several authors e.g. (Simmons and Backus, 1996; Bach et al., 2000; Buland and Omre, 2003; Hampson et al., 2005; Francis, 2013). As mentioned above, if the goal is to invert for density (if possible at all), in addition to acoustic and shear impedance (referred to as Shuey (1985) three-term inversion), good quality seismic and processed angles above 40° are needed. More commonly, a Shuey (1985) two-term (i.e. acoustic and shear impedance) inversion of angle stacks is more robust, although it does not deliver reflectivity for large angles (see **Figure 3.7**) (Francis, 2013).

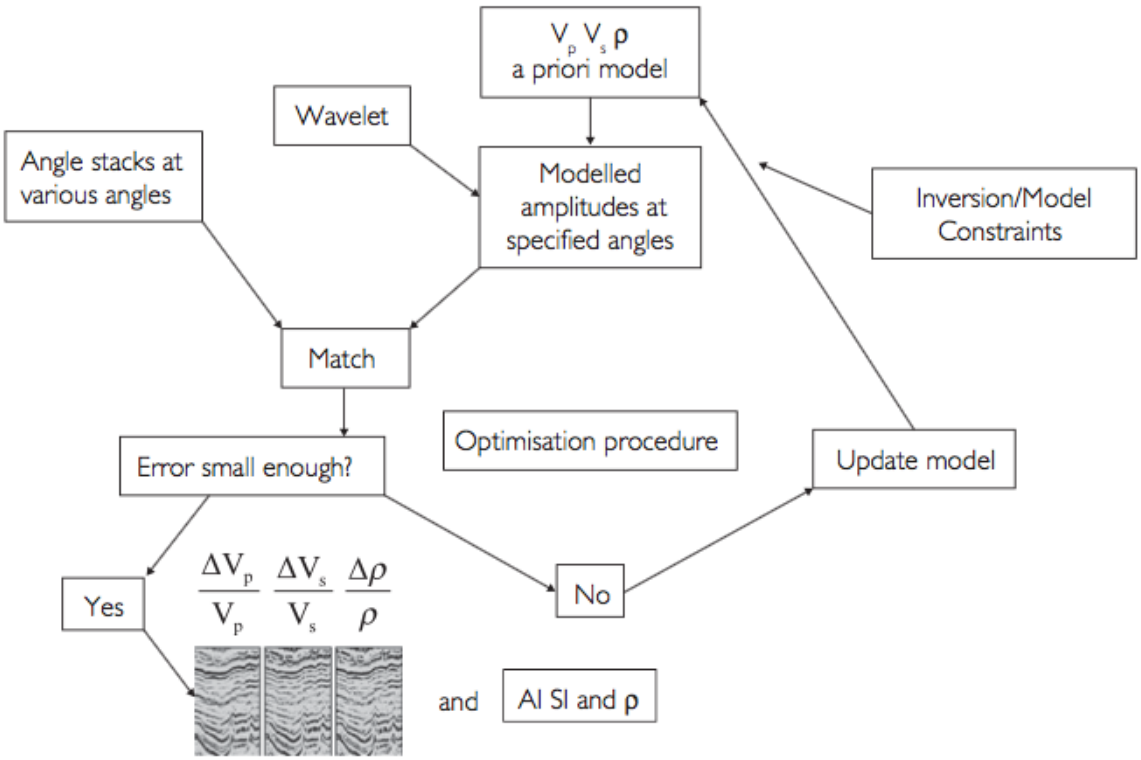

***Figure 3.18**: Schematic workflow of model-based simultaneous AVO inversion. The result of each iteration is a P-impedance, S-impedance, and density cube derived from the prior models (LFM) of Vp, Vs, and density. Subsequently, based on these cubes, the reflectivity as a function of angle is calculated using an approximation of the Zoeppritz equation. The reflectivity cube is then convolved with a wavelet. The resulting synthetic angle stacks (modelled amplitudes) are then compared with the measured angle stacks. If the error is small enough, the synthetic stacks and the impedance cubes are accepted. If not, an optimization procedure follows, and is repeated until the error is small enough. Adopted from (Simm and Bacon, 2014).*

Based on an approximation to the Zoeppritz equation, Buland and Omre (2003) performed a Bayesian linearized AVO inversion. By assuming a logarithmic approximation for changes in the P-wave velocity, these authors inverted for velocity and density, instead of reflectivity.

Based on the work of Simmons and Backus (1996) and Buland and Omre (2003), Hampson et al. (2005) presented an approach of simultaneous pre-stack inversion of PP angle gathers to estimate P-impedance, S-impedance, and density. By including the re-writing of the Aki and Richards equations by Margrave et al. (2001), Hampson et al. (2005) extended this approach to PS data that have been converted to PP time. For the PS case, however, only shear impedance and density can be derived.

3.4.3. JOINT INVERSION OF PP AND PS

P-wave reflectivity is only partially affected by the conversion of P-wave to S-wave energy with offset, whereas PS-wave reflectivity is more dependent on the S-wave velocity (Aki and Richards, 1980). Consequently, if the goal is to achieve more reliable S-wave properties, converted wave reflectivity should be included in the process. As mentioned above, it is possible to obtain estimates of shear impedance through AVO inversion of PP and PS angle stacks, individually. Alternatively, P-impedance, S-impedance, and density can also be derived through a joint inversion of PP and PS data. Based on the PP and PS reflectivity described in the Aki and Richards equations, Stewart (1990) showed how to use two independent observations, compressional wave and converted wave reflectivity, to jointly invert for relative changes in rock properties across an interface. By expressing an empirical relationship between velocity and density (Gardner et al., 1974; Lindseth, 1982) in differential form, Stewart simplified the Aki and Richards equations to relate density to both compressional and shear wave velocities. Finally, keeping Smith and Gidlow (1987) least-squares filtering approach, Stewart could solve for the estimated velocities ($\frac{\Delta\alpha}{\alpha}$ and $\frac{\Delta\beta}{\beta}$).

Over the years, numerous authors have studied different approaches of joint inversion of PP and PS seismic data based on linear approximations (Stewart, 1990; Xu and Bancroft, 1997; Veire and Landro, 2006) and using the exact Zoeppritz's equations (Zhi et al., 2013; Lu et al., 2015). In this thesis, simultaneous AVO PP and joint PP and PS inversion, based on the equations of Aki and Richards are used to carry out estimates of elastic rock properties (P- and S-impedance in particular). The resulting impedances are combined to create Vp/Vs cubes. Subsequently, the Vp/Vs cubes are compared and studied in combination with the results from the AVO analysis (e.g. fluid factor, AVO product, and EEI) to identify and discriminate fluids and lithologies in the reservoir.

4. DATA

Equinor ASA provided the dataset used in this Master thesis, which was acquired in 2008 using ocean bottom cable (OBC). It consists of multiple 3D seismic cubes (e.g. a full-stack PP in PP-time, three PP angle-stacks (0-15°, 15-30°, 30-45°) in PP-time, a full-stack PS in PS-time, and a full-stack PS in PP-time) from the ST083D14 survey, and 12 wells of which 9 are related to exploration and 3 to production (Tables 4.1 and 4.2, and figures 4.1 and 4.2). The survey was acquired in block 30/9, covering an area of approximately 160 km^2, targeting the Oseberg J-area (Figures 1.1, 2.1, and 4.1). The PP seismic data is of normal polarity, where a positive sample corresponds to an increase in acoustic impedance. The PS seismic data is of reverse polarity. Additionally, the interpretation of key horizons (e.g. top reservoir, Brent Gp) and time depth relationships for the PP seismic in PP time were available (Figures 4.1 and 4.2).

In addition to the 3D seismic cubes in PP-time, four PS angle stacks (0-15°, 15-30°, 30-45°, and 45-60°) in PP-time were processed for the purpose of this thesis. To achieve the objectives of this study, the wells (within the outline of the seismic survey) containing sonic and density logs and the 3D seismic cubes in PP-time were key (Tables 4.1 and 4.2, and Figures 4.1 and 4.2).

Considering the area, defined by the extent of the seismic survey (**Figure 4.1**), and the time interval -1800 to -2800 ms defined in **Figure 4.2**, the frequency range (at -10 dB) is 4-37 Hz for the PP seismic and 4-26 Hz for the PS seismic (**Figure 4.3**).

***Table 4.1**: Overview of available seismic cubes in the ST083D12 survey.*

Seismic	Gathers	Full stack in PS-time	Full stack in PP-time	Full stack in depth	Angle stacks in PP-time
PP	x		x	x	x
PS	x	x	x	x	x

***Table 4.2**: Overview of available wells with key logs. For the wells not containing a measured S-sonic log, an S-sonic log calculated from the P-sonic log was provided.*

Well	Purpose	Checkshot	Measured P-sonic log	Measured S-sonic log	Measured density log
30/9-5S	Exploration	x	x		x
30/9-6	Exploration	x	x		x
30/9-9	Exploration	x	x		x
30/9-11	Exploration	x	x		x
30/9-11A	Exploration	x	x		x
30/9-15	Exploration	x	x		x
30/9-18	Exploration		x		x
30/9-20S	Exploration	x	x		x
30/9-25	Exploration		x		x
30/9-J-12	Production		x		x
30/9-J-13	Observation	x	x	x	x
30/9-J-16	Injection		x		x

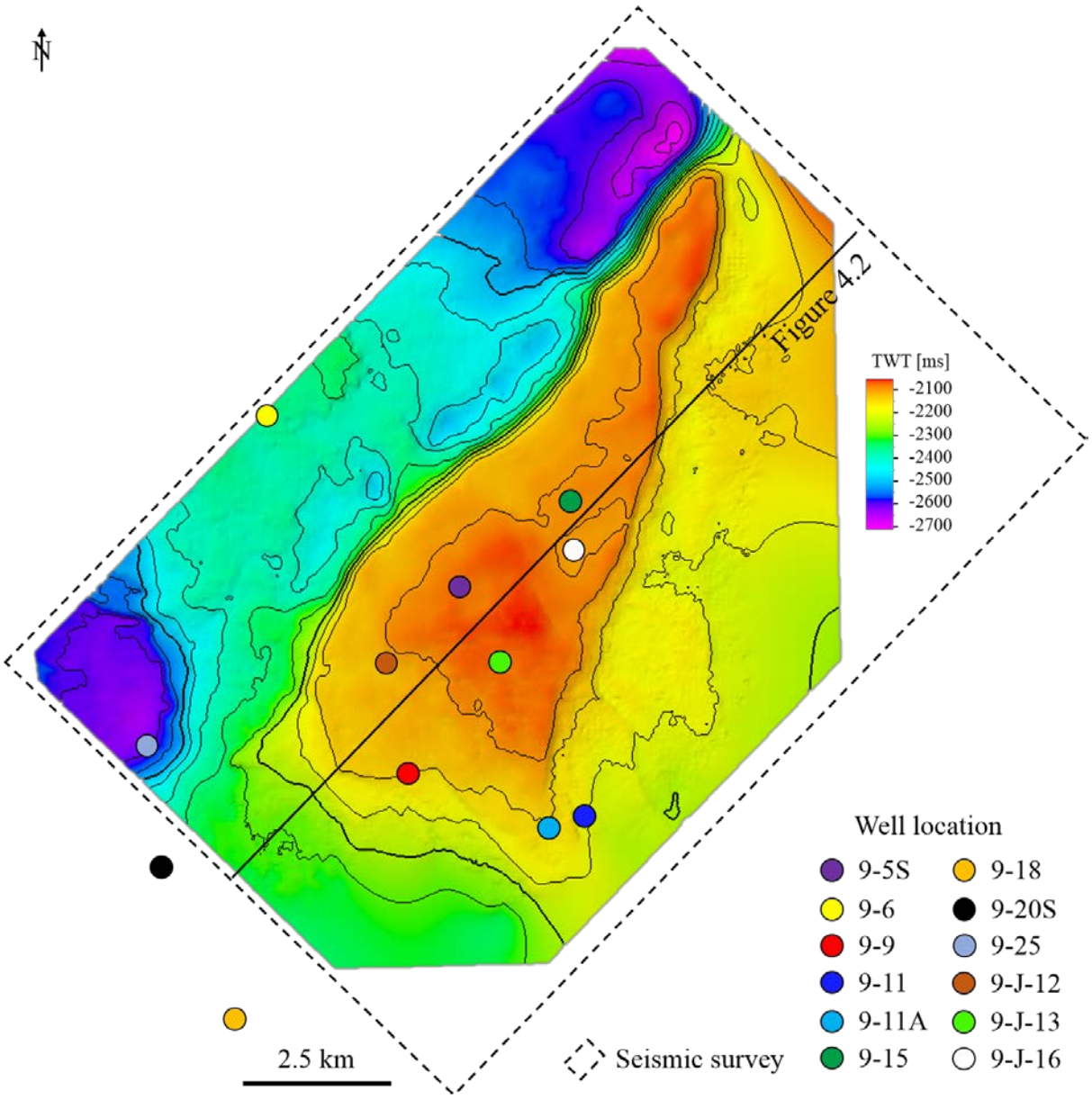

***Figure 4.1**: Interpretation of top reservoir (Brent Gp) provided by Equinor. Location (at the reservoir level) of the provided wells, seismic coverage area, and cross-sections in Figure 4.2 are included in the map. Contour interval 50 ms.*

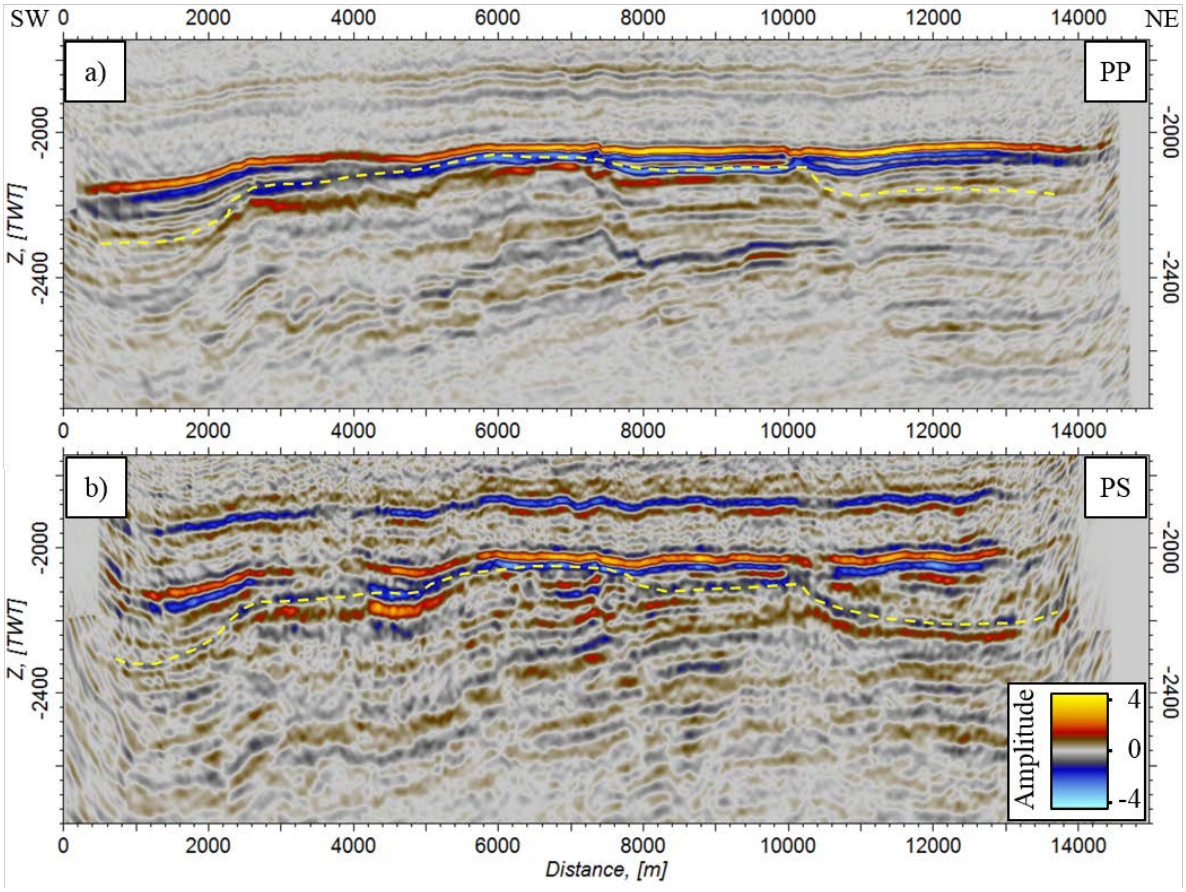

***Figure 4.2**: SW-NE seismic sections showing the interpretation of top reservoir (Brent Gp) in a) PP in PP time and b) PS in PP time. See Figure 4.1 for location of the cross-sections.*

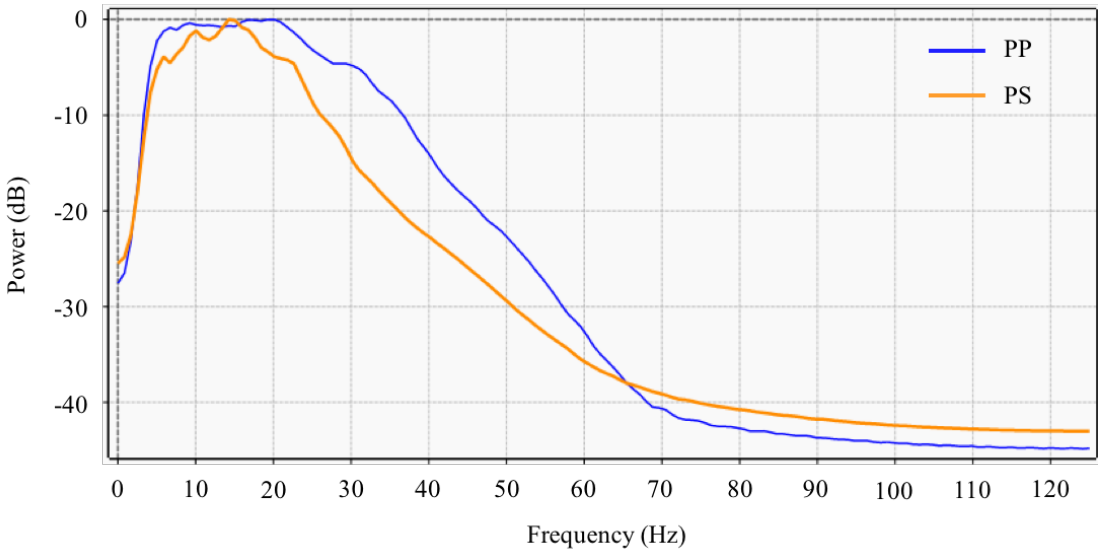

***Figure 4.3**: Frequency spectrum of the PP (blue) and PS (orange) seismic data in PP time at reservoir level. The window of analysis is defined by the extent of the seismic survey, shown in Figure 4.1, and the time interval displayed in Figure 4.2.*

5. METHODS

Chapter 5 provides a detailed description of the workflow and methods used in this study (**Figure 5.1**). Section 5.1 concentrates on the seismic interpretation, the interpretation of well logs, and the QC and pre-conditioning of the data. Section 5.2 focuses on the rock physics analysis, where the relationship between lithology and rock properties is established. Section 5.3 covers the methods used in seismic amplitude analysis, including amplitude extractions, AVO attributes, and extended elastic impedance. Section 5.4 describes the procedure of simultaneous AVO inversion.

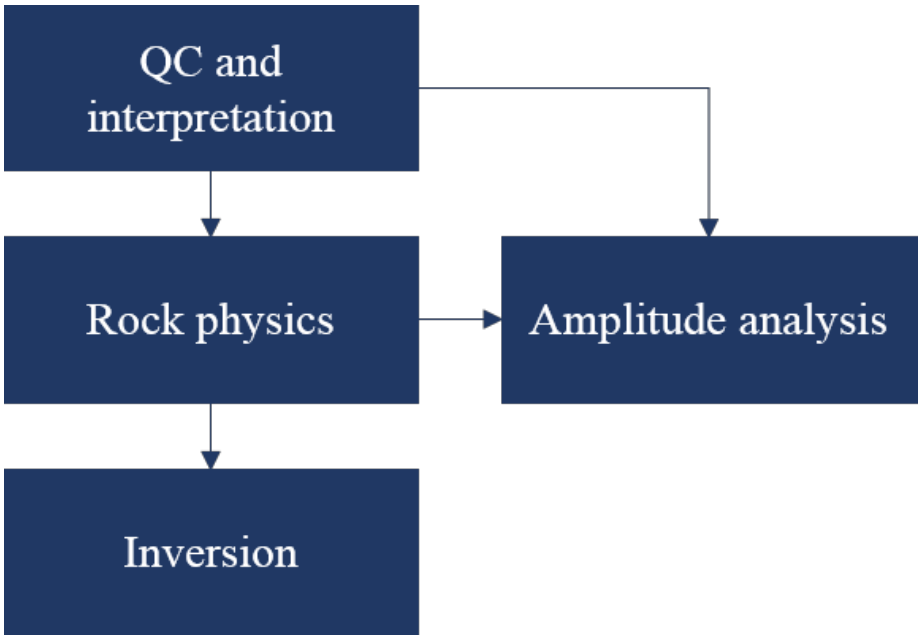

***Figure 5.1**: The general workflow of this thesis. Comprising quality control and interpretation of the data (section 5.1), rock physics analysis (section 5.2), seismic amplitude analysis (section 5.3), and simultaneous AVO inversion (section 5.4).*

5.1. QC AND INTERPRETATION

Pre-conditioning (e.g. trace alignment) of the available seismic data (section 5.1.1), interpretation of the reservoir lithology and fluid, and the sand injectites (section 5.1.2), and quality check and conditioning (e.g. of key horizons and seismic well-tie) (section 5.1.3), were carried out in order to obtain reliable results (**Figure 5.2**).

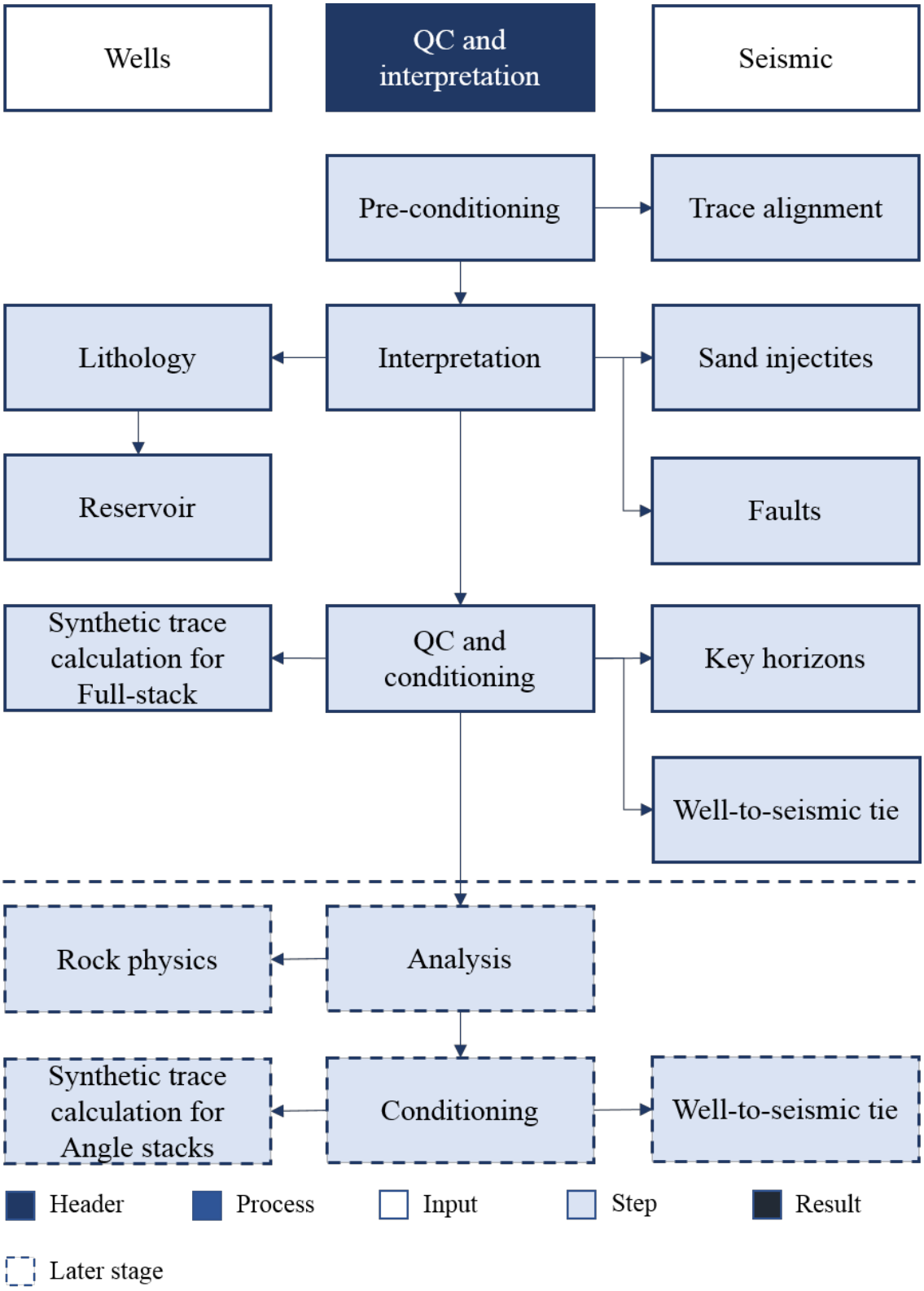

***Figure 5.2**: Workflow showing the different processes and steps of QC, conditioning, and interpretation of the provided data. The last two steps (marked by stippled lines), comprising the well-to-seismic tie of PP and PS angle stacks in PP time, were completed after some rock physics analysis (i.e. elastic and shear wave elastic impedance).*

5.1.1. PRE-CONDITIONING

Matching (trace alignment) of the different vintages of seismic data (i.e. the PP and the PS) to each other, is essential in the process of extracting useful information. Hence, the PS full-stack and the PS angle stacks were matched with the PP full-stack and the PP angle stacks, respectively, using non-rigid matching (NRM) (**Figure 5.3**). NRM estimates the change in two-way time of seismic events between two seismic volumes and optimizes the match between volumes on a sample-by-sample basis. Next, the PS mid and the PS far angle stacks were aligned with the PS near stack (**Figure 5.3**b).

5.1.2. INTERPRETATION

The 3D seismic shows reduced S/N (signal-noise ration) below the carbonate-cemented sand injectites in the overburden (see section 2.2.2 Overburden, **Figure 2.3**). Consequently, the sand injectites, were outlined (in both the PP and the PS seismic cubes) to investigate their influence on the amplitudes at reservoir level (**Figure 5.4**). Based on the dominant frequency (i.e. 20 Hz for the PP and 15 Hz for the PS, see **Figure 4.3**), and the interval velocity at reservoir level (approximately 2800 m/s), the vertical resolution (¼ wavelength) was calculated. At reservoir level, the major faults were also identified and mapped.

At well scale the main reservoir zone (Brent Gp) was studied, focusing on the wells containing the necessary well logs (e.g. gamma-ray, neutron porosity, compressional sonic, shear sonic, and density). Based on the well logs (i.e. the gamma-ray and the neutron/density cross-over) the lithological and fluid changes at the reservoir level were interpreted.

5.1.3. QC AND CONDITIONING

Based on the available interpretations (i.e. Brent Gp and Dunlin Gp) a time thickness map (seismic top – base) of the main reservoir zone (comprising the complete Brent Gp), was created to investigate the reservoir thickness within the structure.

To tie the wells to the PS seismic in PP-time, a detailed seismic-to-well tie (i.e. a checkshot calibration followed by synthetic trace calculation) was carried out for the wells containing a checkshot (see Table 4.2) and the necessary information for the synthetic trace calculation (i.e. P-sonic, S-sonic, and density logs) (**Figure 5.5**).

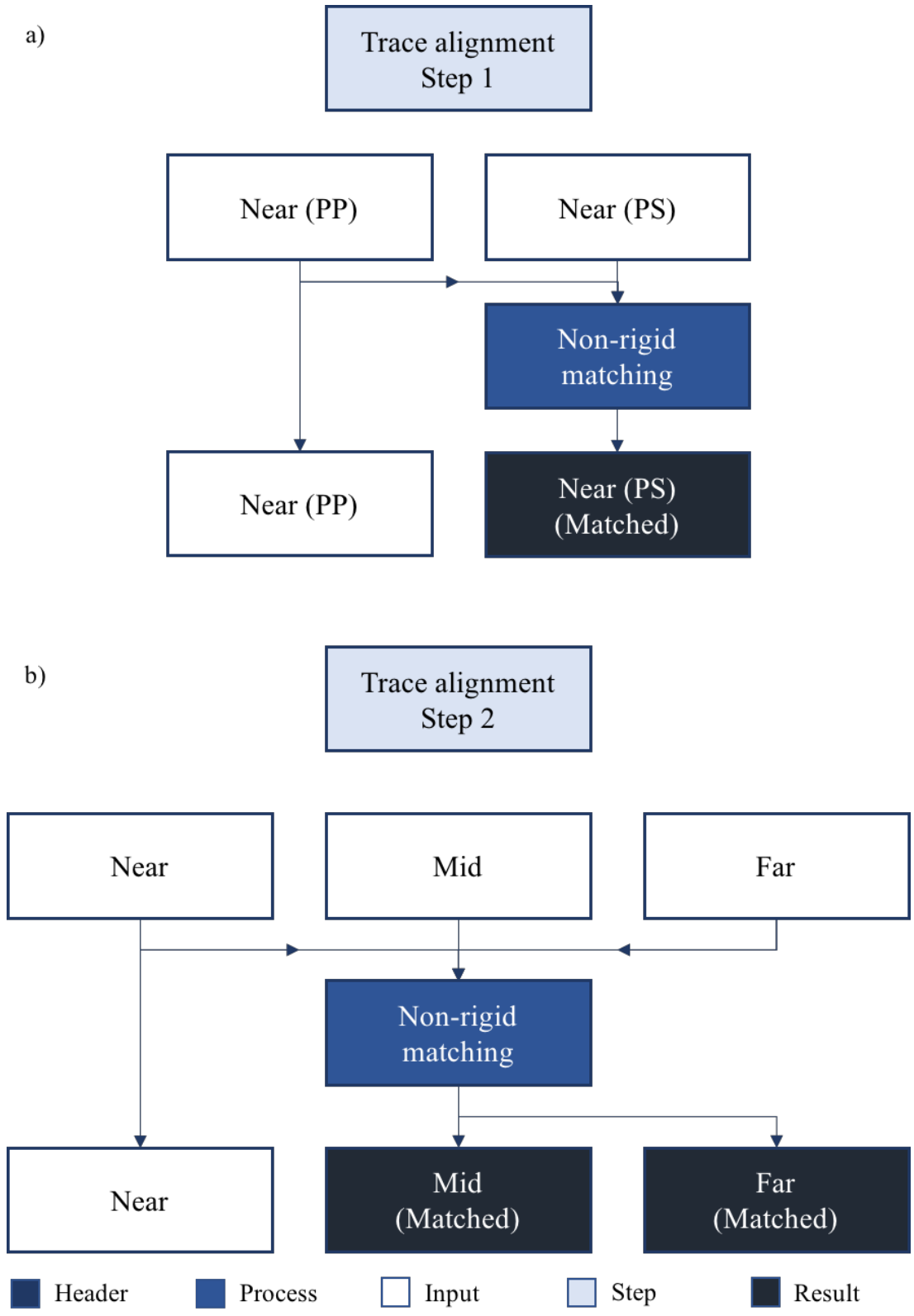

***Figure 5.3**: Seismic trace alignment. a) PS near stack in PP time aligned with PP near stack (Step 1) using non-rigid matching. b) PS mid and far stack matched with the PS near stack (Step 2).*

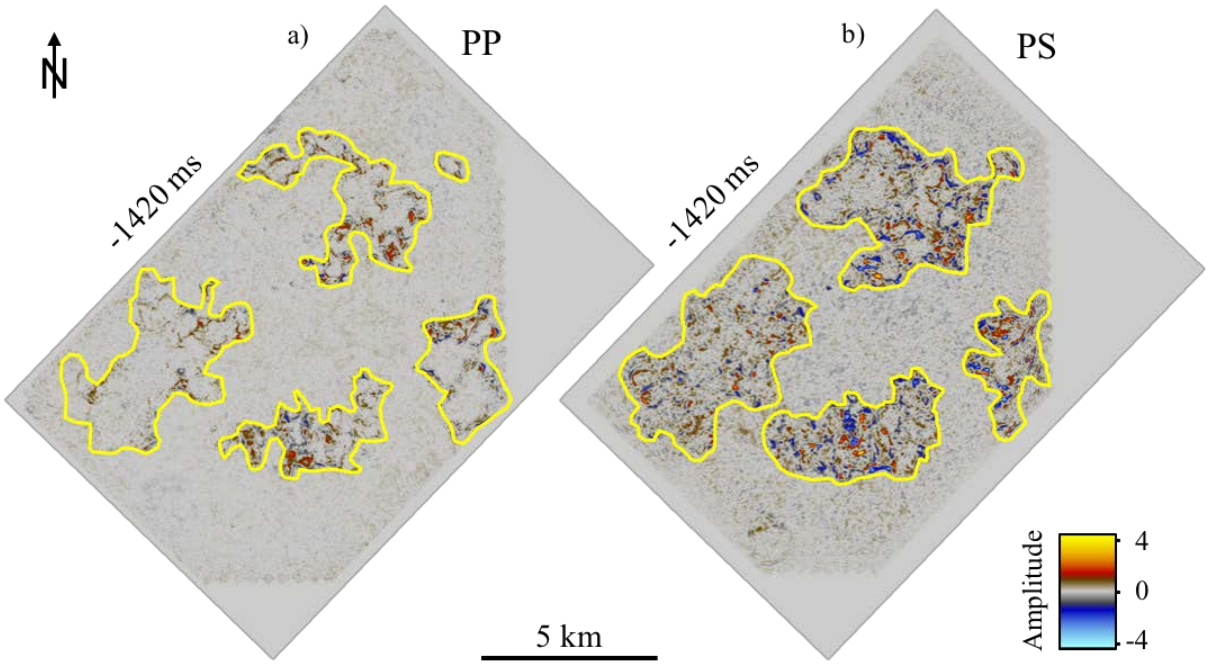

***Figure 5.4**: Time slice (-1420 ms) outlining the sand injectites in a) PP seismic and b) PS seismic in PP time.*

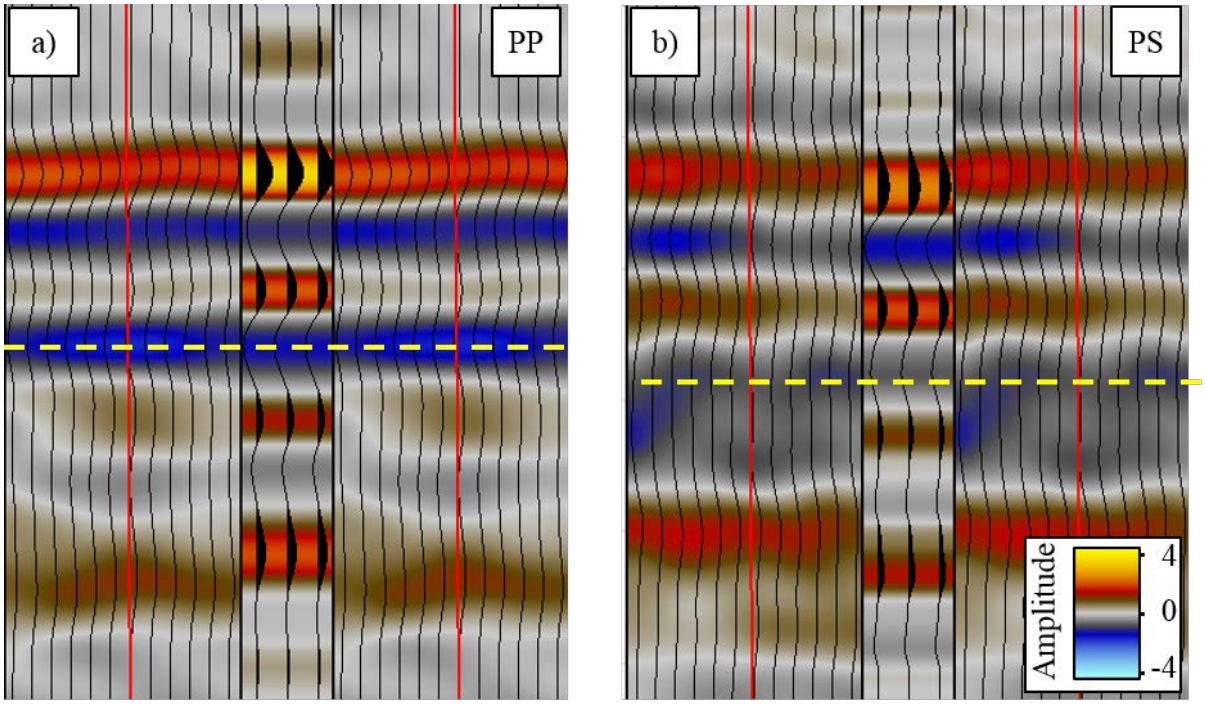

***Figure 5.5**: Seismic well tie for a) PP seismic in PP time, and b) PS seismic in PP time, in well 30/9-9. Interpretation of Top reservoir (Brent Gp) displayed with yellow dashed lines.*

5.2. ROCK PHYSICS

Rock physics analysis, comprising the calculation of elastic parameters and rock physics cross-plots (section 5.2.1), the calculation of elastic and shear wave elastic impedance (section 5.2.2), and log correlation for extended elastic impedance, was carried out to establish relationships between the seismic properties and the elastic reservoir rock properties derived at the wells.

5.2.1. LITHOLOGY AND ROCK ELASTIC PROPERTIES

Based on the available compressional (P) sonic, shear (S) sonic, and density logs, estimates of elastic rock properties (i.e. compressional velocity (Vp), shear velocity (Vs), acoustic impedance (AI), shear impedance (SI), Vp/Vs ratio, bulk modulus (K), shear modulus (μ), and Poisson's ratio (ν) were calculated along the well trajectories (**Figure 5.6**)

To validate the discrimination of different facies (lithology and fluid) using the Vp/Vs log combined with the P- or S-impedance log, cross-plots of Vp/Vs versus acoustic impedance (AI) logs were made and overlaid by logs that allow a distinction between different facies (i.e. neutron/density log and gamma ray log). The different clusters in the AI vs Vp/Vs cross-plot were compared against the interpreted lithologies in well 30/9-J-13, to provide a value range (in terms of AI and Vp/Vs) for the different lithologies.

5.2.2. ELASTIC AND SHEAR WAVE ELASTIC IMPEDANCE

Based on the Vp, Vs, and density logs, elastic impedance and shear wave elastic impedance were calculated, and used for the synthetic trace calculation, to tie the wells to the PP and the PS angle stacks, respectively (see Whitcombe (2002) for elastic impedance, and Duffaut et al. (2000) for shear wave elastic impedance). The EI and the SEI were rotated by the effective incidence angle θ (i.e. 7° (near stack), 22° (mid stack), and 37° (far stack)) to match the corresponding angle stacks, in the PP and the PS in PP time, respectively.

5.2.3. LOG CORRELATION FOR EXTENDED ELASTIC IMPEDANCE

Based on the Vp, Vs, and density logs, an extended elastic impedance log equivalent to acoustic impedance (i.e. angle χ (chi) = 0) were calculated using equation (16) (see section 3.3.4 Extended elastic impedance, and Whitcombe et al. (2002)). The EEI log was then tuned by the

angle χ providing the best correlation with the bulk modulus and the Vp/Vs ratio logs (**Figure 5.6**).

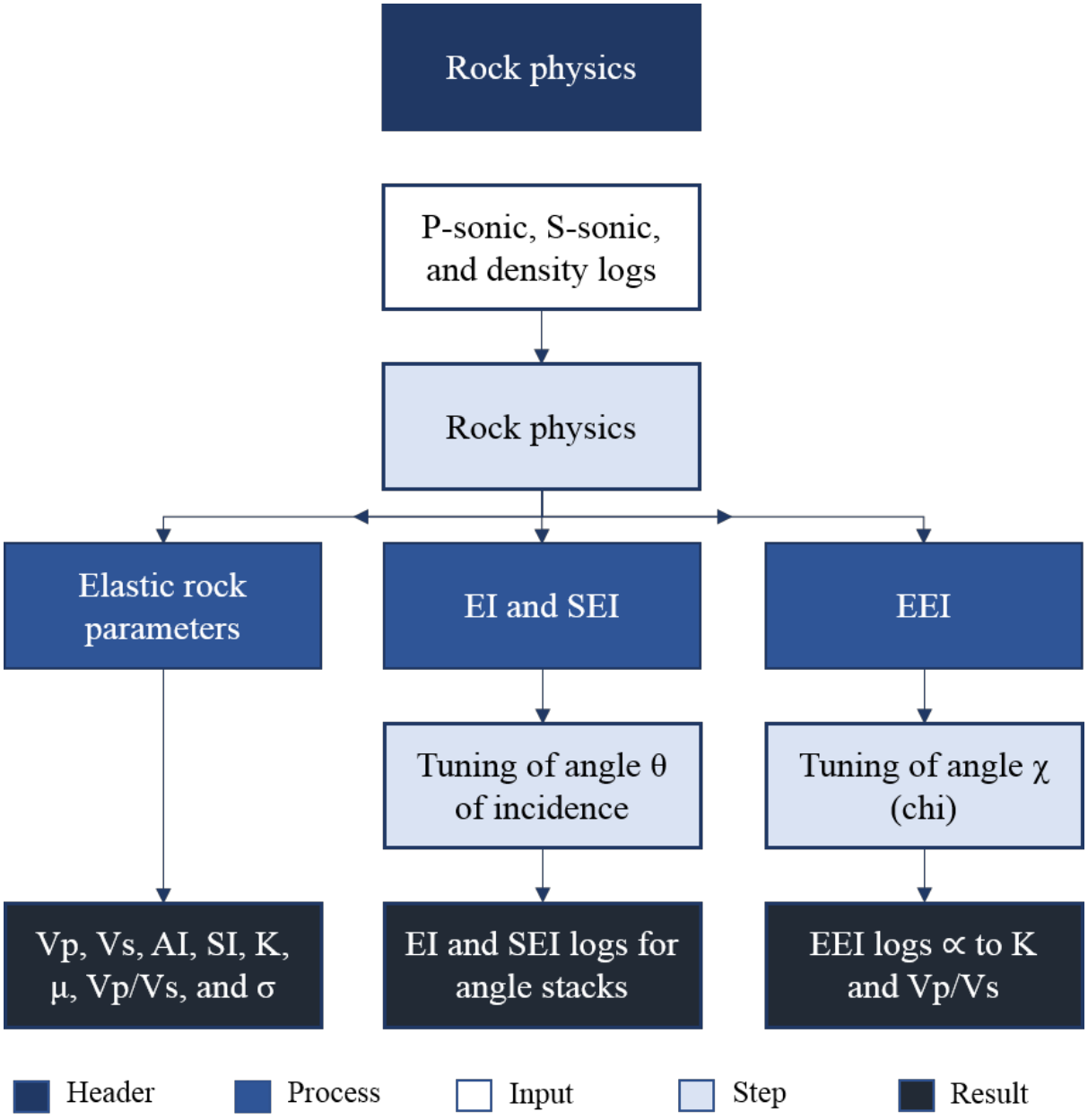

***Figure 5.6**: Rock physics workflow, comprising the calculation of elastic rock parameters (where K, μ, and ν are bulk modulus, shear modulus, and Poisson's ratio, respectively), the calculation of elastic and shear wave elastic impedance (EI and SEI, respectively), and the calculation of extended elastic impedance (EEI). The EI and the SEI were tuned by the incidence θ of the respective angle stacks. The EEI were tuned by angle χ (chi) to be approximately proportional to the bulk modulus and the Vp/Vs ratio logs.*

5.3. SEISMIC AMPLITUDE ANALYSIS

Seismic amplitude analysis, including seismic full-stack attributes (e.g. RMS amplitude) (section 5.3.1), amplitude versus offset (AVO) attributes (e.g. fluid factor and AVO product) (section 5.3.2), and extended elastic impedance analysis, was carried out to investigate amplitude anomalies at the reservoir level (**Figure 5.7**).

5.3.1. SEISMIC FULL-STACK ATTRIBUTES

Root mean square (RMS) amplitudes were extracted from the full stack PP and PS, individually, to investigate amplitude anomalies of an interval stretching from the top reservoir (Brent Gp) to 20 ms below the top.

5.3.2. AVO ANALYSIS

Based on the PP angle stacks, the reflectivity versus offset was analyzed, and the expected AVO class for the top reservoir was determined. Based on the PP angle stacks, and the Shuey (1985) two-term approximation, intercept and gradient cubes were created. Subsequently, the intercept and gradient were used to calculate AVO attributes (i.e. the fluid factor and the AVO product) to highlight class II and III AVO anomalies (see **Figure 3.8**), and deviations from the fluid line (see Figures 3.9 and 3.10), respectively (**Figure 5.7**).

5.3.3. EXTENDED ELASTIC IMPEDANCE

Based on the chi angles found in the rock physics analysis, and the intercept and gradient cubes derived from the PP angle stacks, EEI reflectivity cubes approximately proportional to bulk modulus and Vp/Vs reflectivity were generated to highlight changes in the fluid and lithology (**Figure 5.7**).

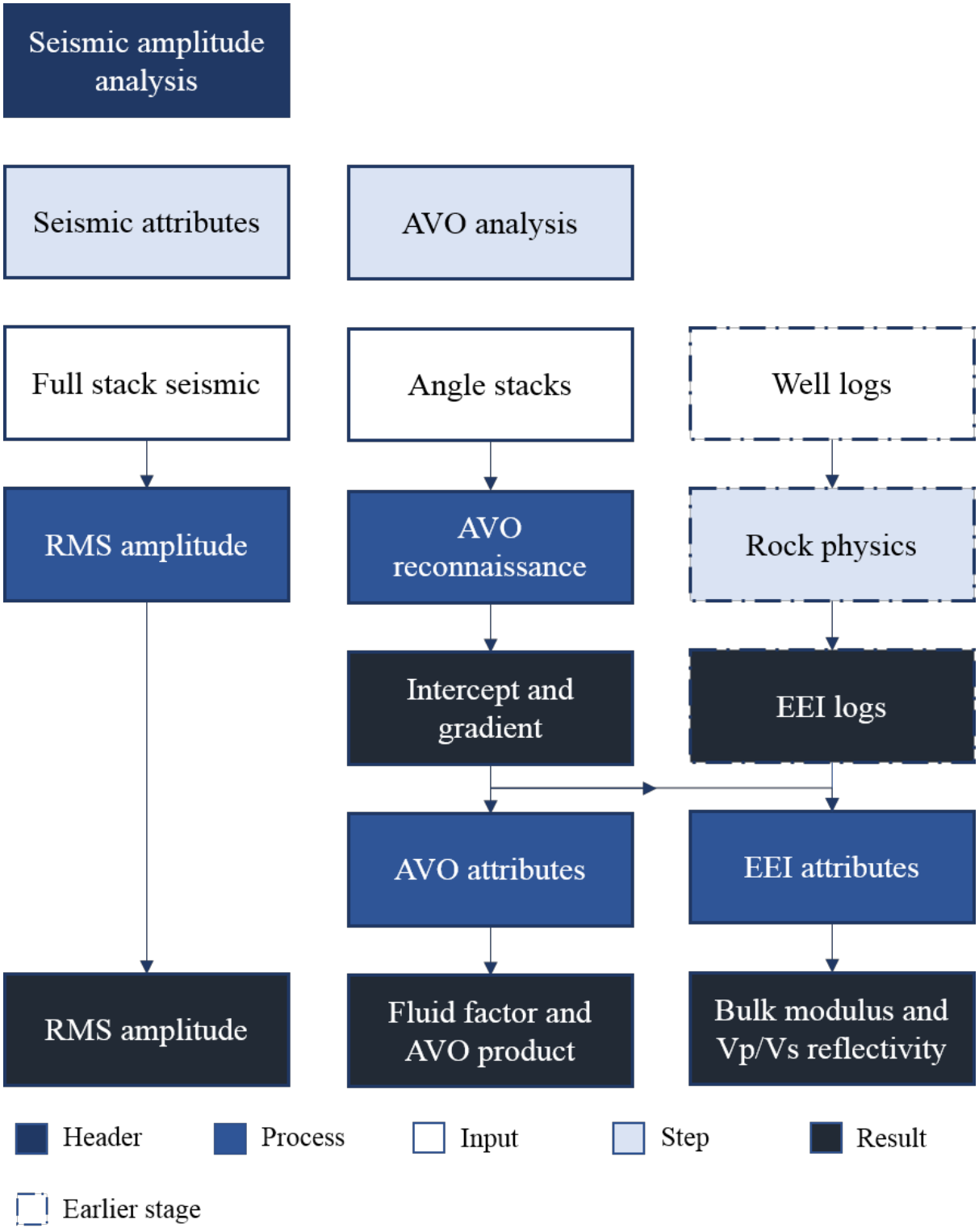

***Figure 5.7**: Seismic amplitude analysis workflow, comprising both seismic full-stack attributes and analysis of amplitude variation with offset (AVO attributes). The AVO analysis is divided in two parts. 1) using intercept and gradient for AVO attributes (e.g. fluid factor and AVO product), and 2) using intercept and gradient to calculate extend elastic impedance (i.e. bulk modulus and Vp/Vs) reflectivity.*

5.4. INVERSION

Data conditioning, including trace alignment of the PS angle stacks (section 5.4.1), wavelet extraction for the angle stacks (section 5.4.2), and low frequency model generation (section 5.4.3), were carried out to facilitate the simultaneous AVO inversion of PP and joint PP and PS data (section 5.4.4 and 5.4.5, respectively).

5.4.1. DATA CONDITIONING

The PS angle stacks were matched with the PP angle stacks (i.e. trace alignment, see section 5.1.1 Pre-conditioning, **Figure 5.3**). Then an area of interest (AOI), defined by the top reservoir surface in **Figure 4.1** and the time interval displayed in **Figure 4.2**, were chosen. Subsequently, three wells within the AOI (30/9-9, 30/9-15, and 30/9-J-13, **Table 4.1**, **Figure 4.1**) were selected for the inversion procedure.

5.4.2. WAVELET EXTRACTION

Wavelets for the PP and PS angle stacks were extracted from the synthetic studies (i.e. synthetic trace calculation, see section 5.2.2 Elastic and shear wave elastic impedance) (**Figure 5.8**).

5.4.3. LOW FREQUENCY MODEL GENERATION

Based on the geometry of the seismic cubes (PP and PS), the P- and S-impedance, and density well logs (from the selected wells, see section 5.4.1 Data conditioning) were used to construct low frequency models (LFM) guided by the seismic horizons to provide the low frequencies not present in the seismic data (**Figure 5.9**). A high-cut filter (8 Hz) was applied to the well log data.

5.4.4. SIMULTANEOUS PP AVO INVERSION

The extracted wavelets (for each of the PP angle stacks, **Figure 5.8**a), the generated low frequency models (i.e. AI, SI and density, **Figure 5.9**), the three PP angle stacks, and the horizons (Brent Gp and Drake Fm) served as input to the simultaneous AVO PP inversion algorithm (i.e. Aki and Richards) (**Figure 5.10**). The results from the simultaneous AVO PP inversion were a P-impedance, an S-impedance, and a density cube.

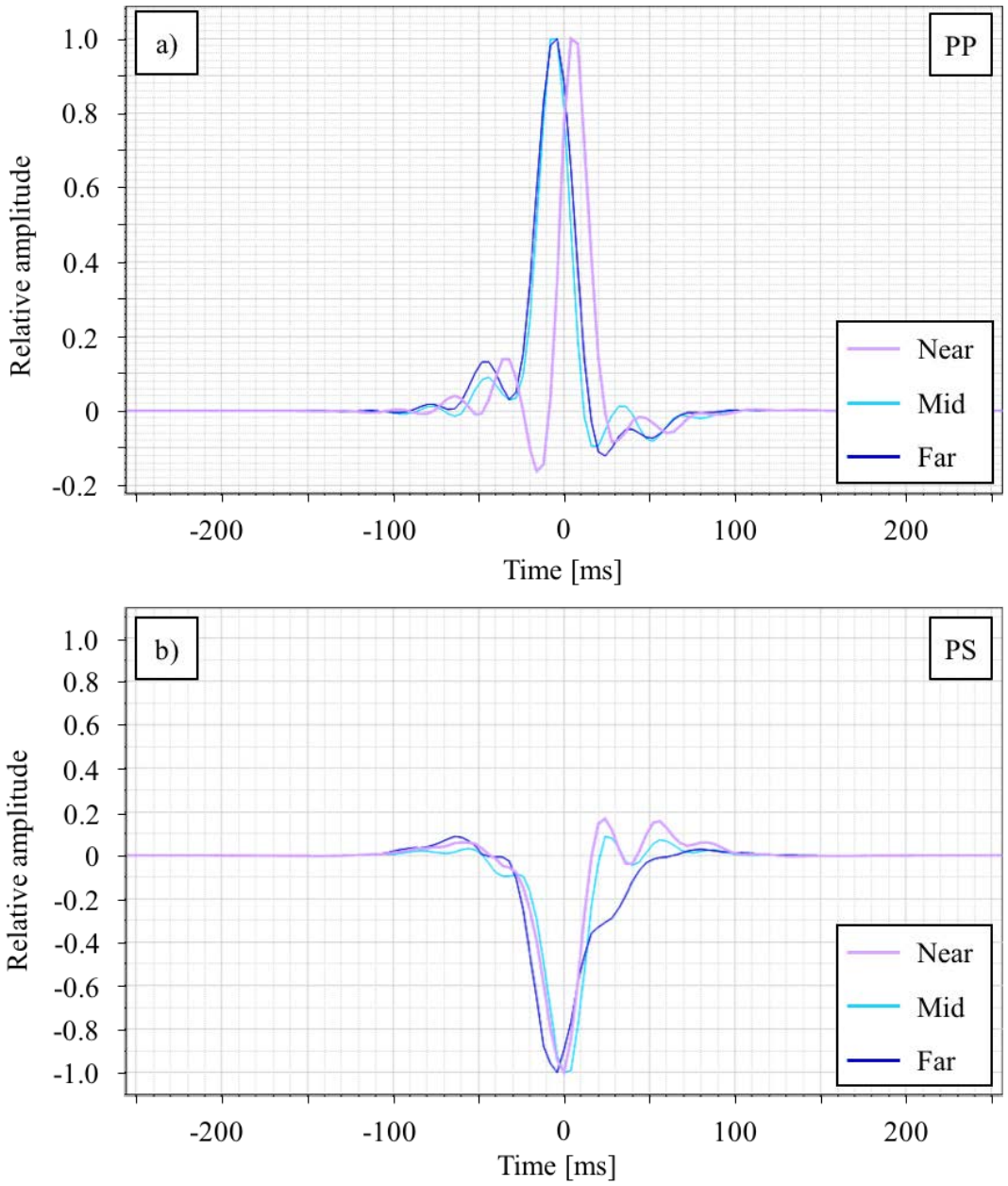

***Figure 5.8**: The extracted wavelets from the near, mid, and far stacks of a) PP and b) PS. The PP wavelets were used in the AVO PP simultaneous inversion. The PP and PS wavelets were used in the joint AVO PP and PS simultaneous inversion.*

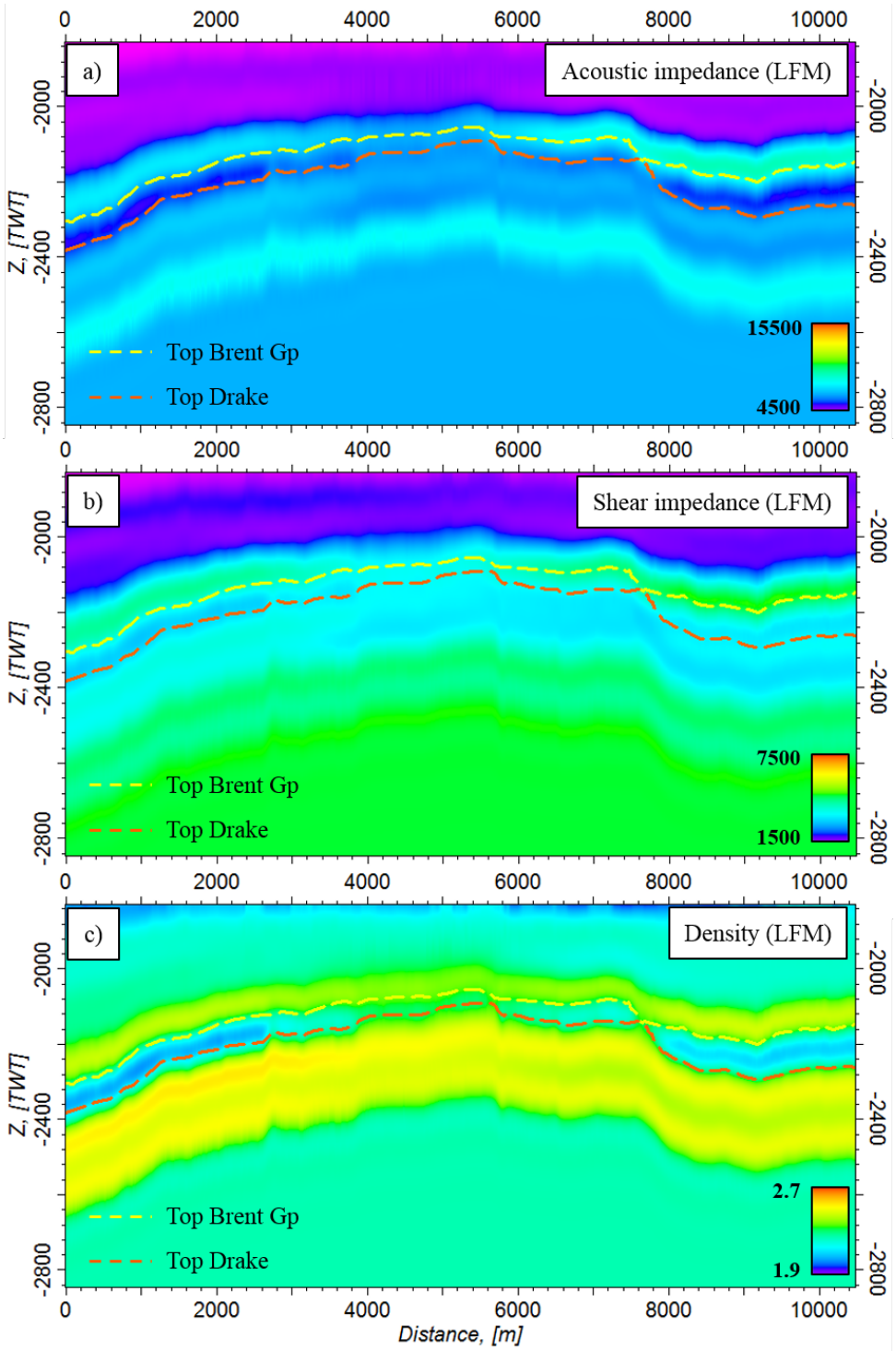

***Figure 5.9**: Low frequency model (LFM) sections of a) acoustic impedance, b) shear impedance, and c) density generated from the well logs to provide the low frequencies not present in the seismic data and which are required for the inversion. The guiding horizons top Brent Gp (yellow) and top Drake are highlighted in the sections.*

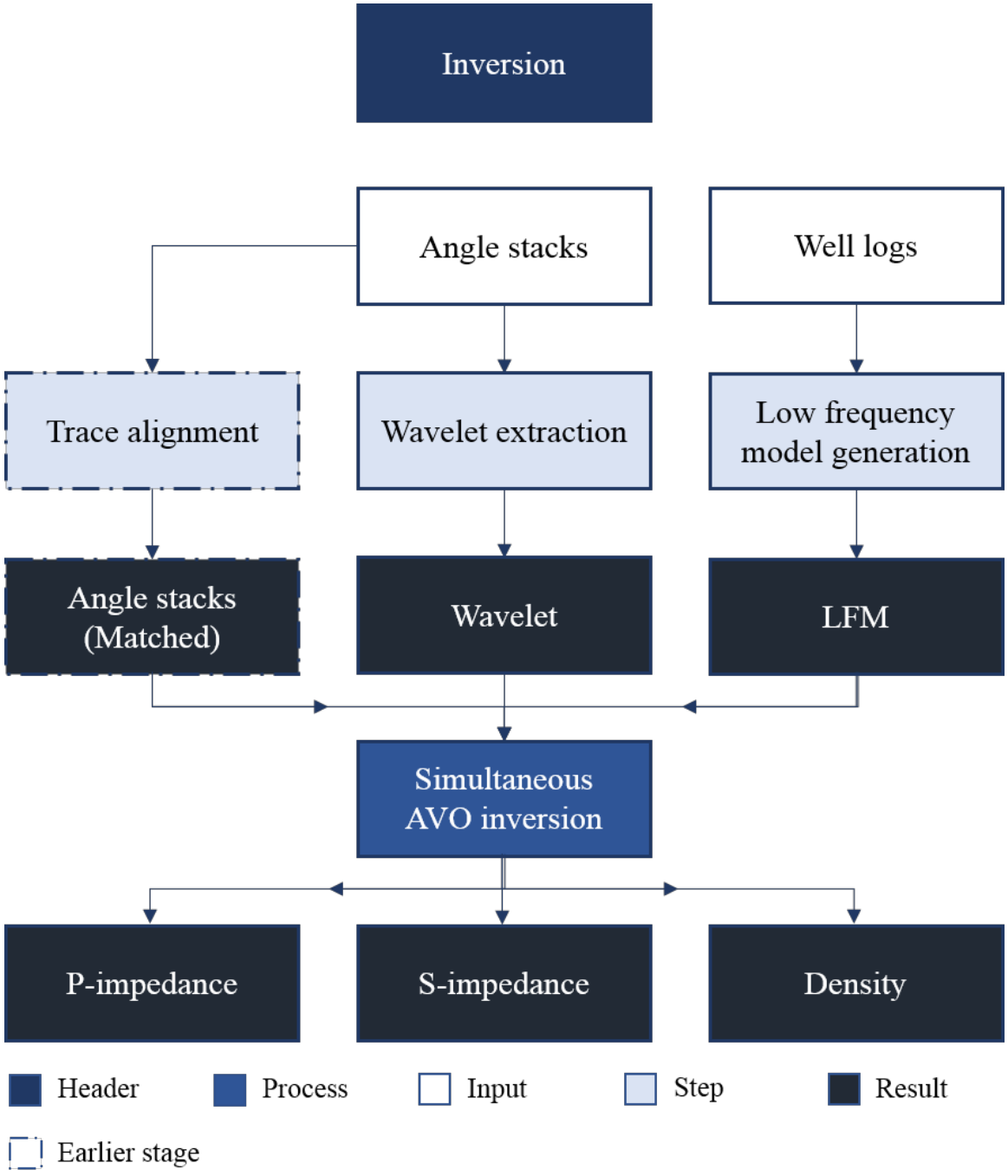

***Figure 5.10**: Workflow for simultaneous AVO inversion, including pre-conditioning (seismic trace alignment, Figure 5.3) of angle stacks, wavelet extraction and low frequency model generation.*

5.4.5. JOINT PP AND PS AVO INVERSION

For the joint simultaneous AVO PP and PS inversion algorithm the input was the same as the AVO PP inversion, with the inclusion of the PS wavelets (**Figure 5.8**b) and the three PS angle stacks in PP time. The results from the joint simultaneous AVO PP and PS inversion were a P-impedance, an S-impedance, and a density cube.

Based on the acoustic and shear impedances derived in the two simultaneous AVO inversions, Vp/Vs cubes were calculated for the AVO PP, and the joint AVO PP and PS, individually. Subsequently, Vp/Vs values were extracted at the reservoir level and investigated using horizon probes (i.e. horizon slices of different thicknesses defined by the geometry of the top and base of the Brent Gp) within the reservoir zone. Based on the results from the rock physics studies (i.e. the Vp/Vs relation with pore-fluid content) the opacity of the horizon probes was adjusted (high values were filtered out) to highlight the Vp/Vs anomalies.

5.4.6. INVERSION QC

A quality control (QC) of the two inversion results (i.e. PP and joint PP and PS) was carried out at the wells. The acoustic and shear impedance well logs were convolved with a wavelet, to match the seismic frequency spectrum (**Figure 5.11**), and subsequently compared with the acoustic and shear impedance derived in the two inversions.

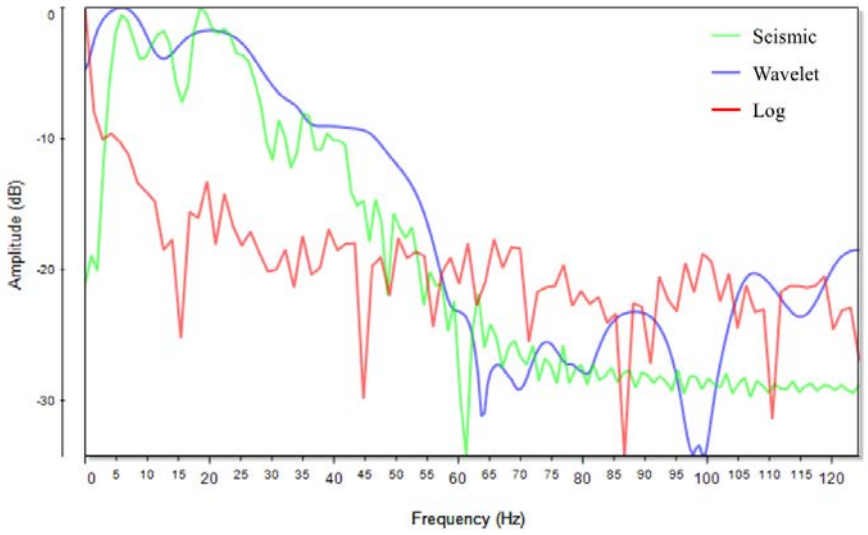

***Figure 5.11**: Frequency spectrum of the seismic (green) and impedance log (red), and the wavelet (blue) used to match the spectrum of impedance log with the seismic frequency spectrum.*

6. RESULTS

Chapter 6 provides a description of the results of this Master thesis. Section 6.1 covers the interpretation of the sand injectites and well log interpretation in the reservoir zone. Section 6.2 focuses on the relationship between lithology and the elastic reservoir rock properties derived at the wells. Section 6.2 describes in detail the results of the full stack amplitude and AVO analysis. Finally, section 6.5 discusses the results from the simultaneous PP and joint PP / PS AVO inversions.

6.1. QC AND INTERPRETATION

In this section, the implications of the sand injectites present in the overburden (section 6.1.1), the frequency content of the PP and PS cubes (section 6.1.2), and a reservoir overview at well and seismic scale (section 6.1.3) are presented.

6.1.1. IMPLICATIONS OF THE SAND INJECTITES

The study area is severely suffering from the presence of sand injectites in the overburden, therefore it is important to be aware of the influence these bodies have on the PP and PS data. **Figure 6.1** shows a time slice (- 1420 ms) at the sand injectites level with the outline of the sand injectites in the PP and the PS data. **Figure 6.1** also displays the same outline on a time slice (- 2108 ms) through the reservoir zone. Following the bright red reflector (highlighted in the PP and PS time slices) from the south, along the western side to the north, one observes a loss of amplitude energy when entering the area covered by a sand injectite (**Figure 6.1**). In general, the area within the outline of the sand injectites at the reservoir level shows less amplitude energy compared to the surrounding amplitudes.

The geometry of the sand injectites, both laterally and vertically, shows some differences in the PP and PS domain, and in general it is more extended in the PS domain (Figures 6.1 and 6.2). This suggests that the sand injectites have a greater impact on the seismic amplitudes in the PS domain compared to the PP domain. This is also supported by studying a cross-section of an area below the sand injectites (**Figure 6.2**). This figure shows that the PS seismic is affected more by the sand injectites than the PP seismic, indicating lithology related anomalies.

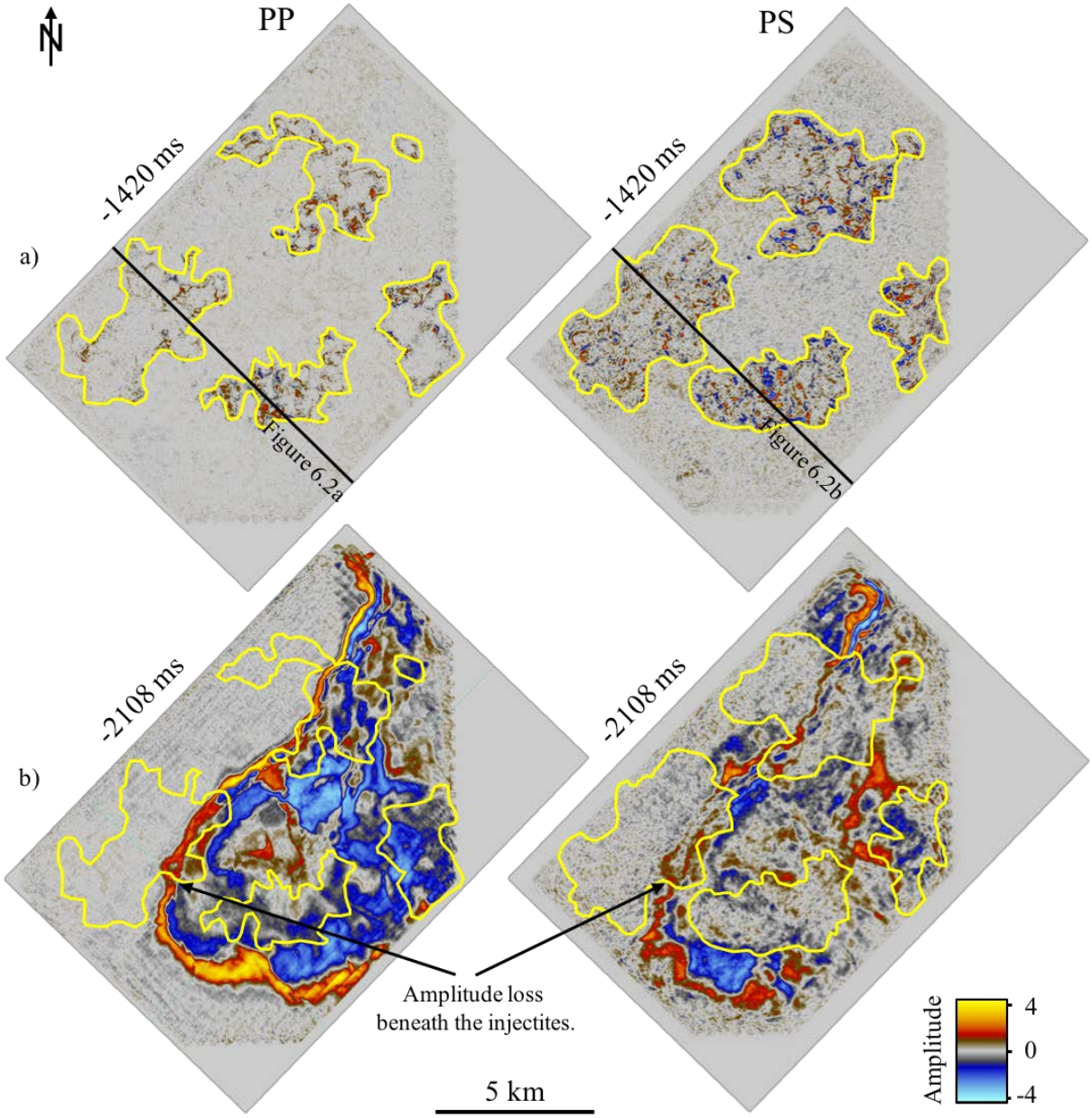

***Figure 6.1**: Outline of the sand injectites a) in the overburden (time slice at - 1420 ms) and b) at the reservoir level (- 2108 ms), of the PP cube (left) and PS cube (right). Notice the decreasing positive amplitude (highlighted in the PP and PS at the reservoir level) when entering beneath the sand injectites. In general, the amplitudes are weaker within the outline of the sand injectites at the reservoir level.*

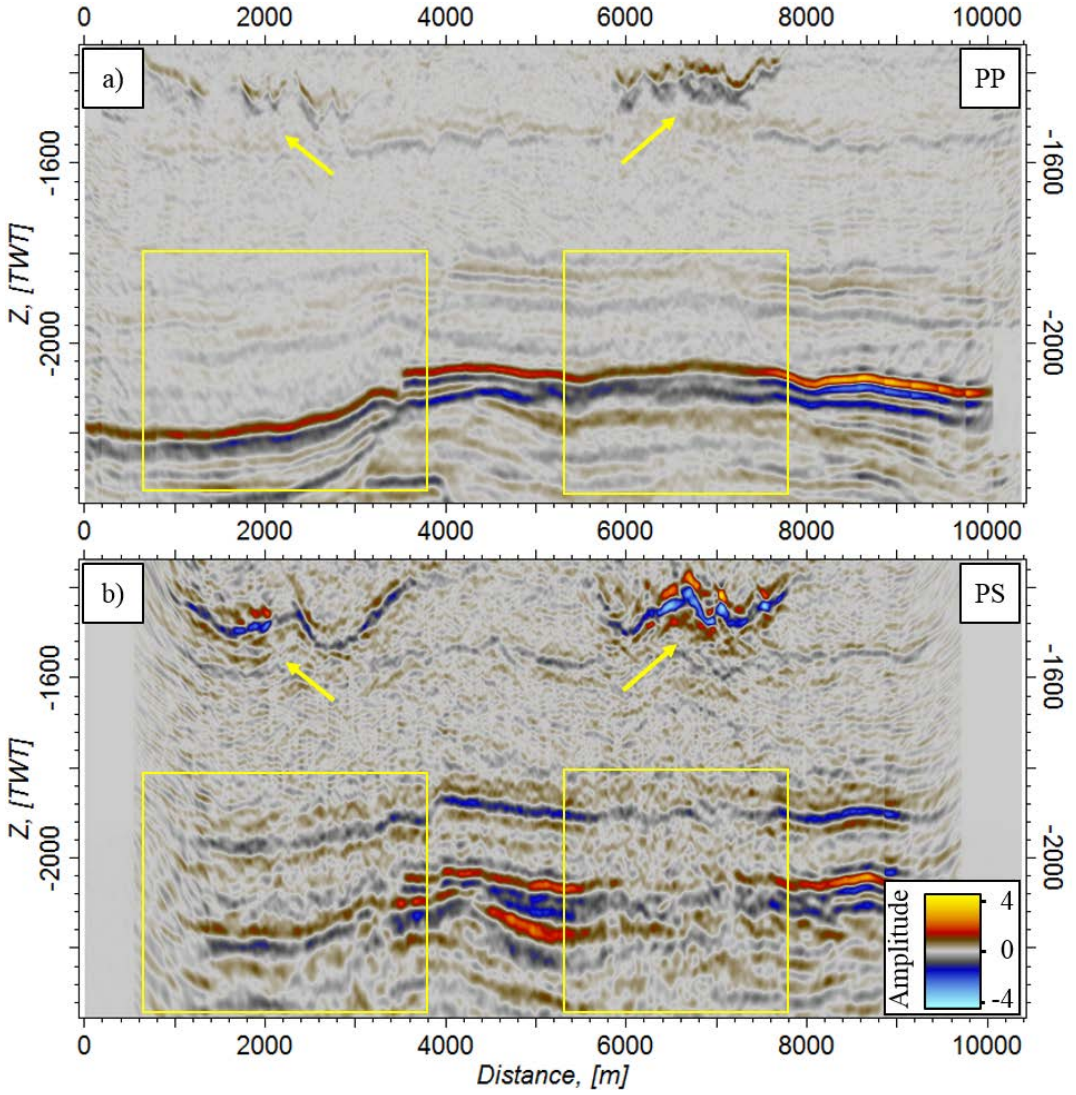

***Figure 6.2**: Impact of the sand injectites (yellow arrows) at reservoir level (yellow square) of a) PP and b) PS seismic section. Notice the loss of amplitudes when entering the yellow squares beneath the sand injectites. The geometry of the sand injectites is different in the two domains. In general, the sand injectites have a greater impact on the PS data compared to the PP data. See Figure 6.1 for the location of the cross-sections.*

6.1.2. RESOLUTION IN THE RESERVOIR ZONE

As mentioned earlier, due to the lower frequency range of S-waves relative to P-waves, the resolution of PP data is in general superior to that of the PS (Stewart et al., 2002) (see **Figure 4.3**). In the PP data (with a frequency range of 4 – 37 Hz), the vertical resolution (see section 5.1.2) is approximately 25 ms at the reservoir level, whereas in the PS data (with a frequency range of 4-26 Hz), it is approximately 35 ms at reservoir level.

6.1.3. RESERVOIR OVERVIEW

This thesis focuses on the main reservoir zone (i.e. the Brent Gp) within the horst structure between the Brage and the Brage East faults (**Figure 6.3**). **Figure 6.4** shows a time thickness map of the complete Brent Gp (see section 5.1.3), having a thickness range of around 100 ms in the south, to 0-20 ms in the vicinity of the Brage Fault in the west and north. The thickness distribution of the Brent Gp, shown in **Figure 6.4**, corresponds with the interpreted thickness of the well data (e.g. approx. 80 ms in 30/9-9, 50 ms in 30/9-J-13, 14 ms in 30/9-5S, and 18 ms in 30/9-15). A gradual westward and northward thinning of the Brent Gp is observed within the horst structure (Figures 6.3 and 6.4).

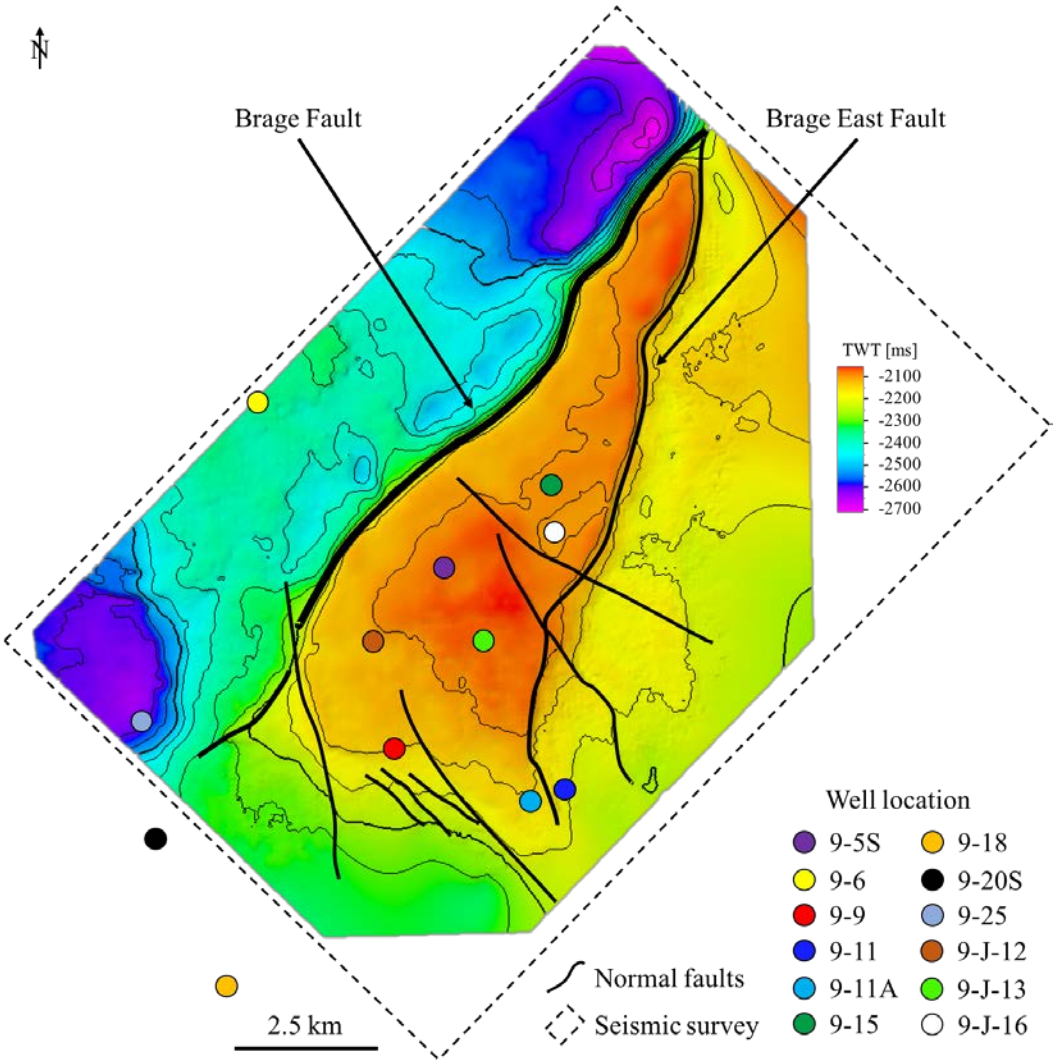

Figure 6.3: *Top reservoir (Brent Gp) map, showing the location (at the reservoir level) of the provided wells, seismic coverage area, and the interpreted faults. Contour interval 50 ms.*

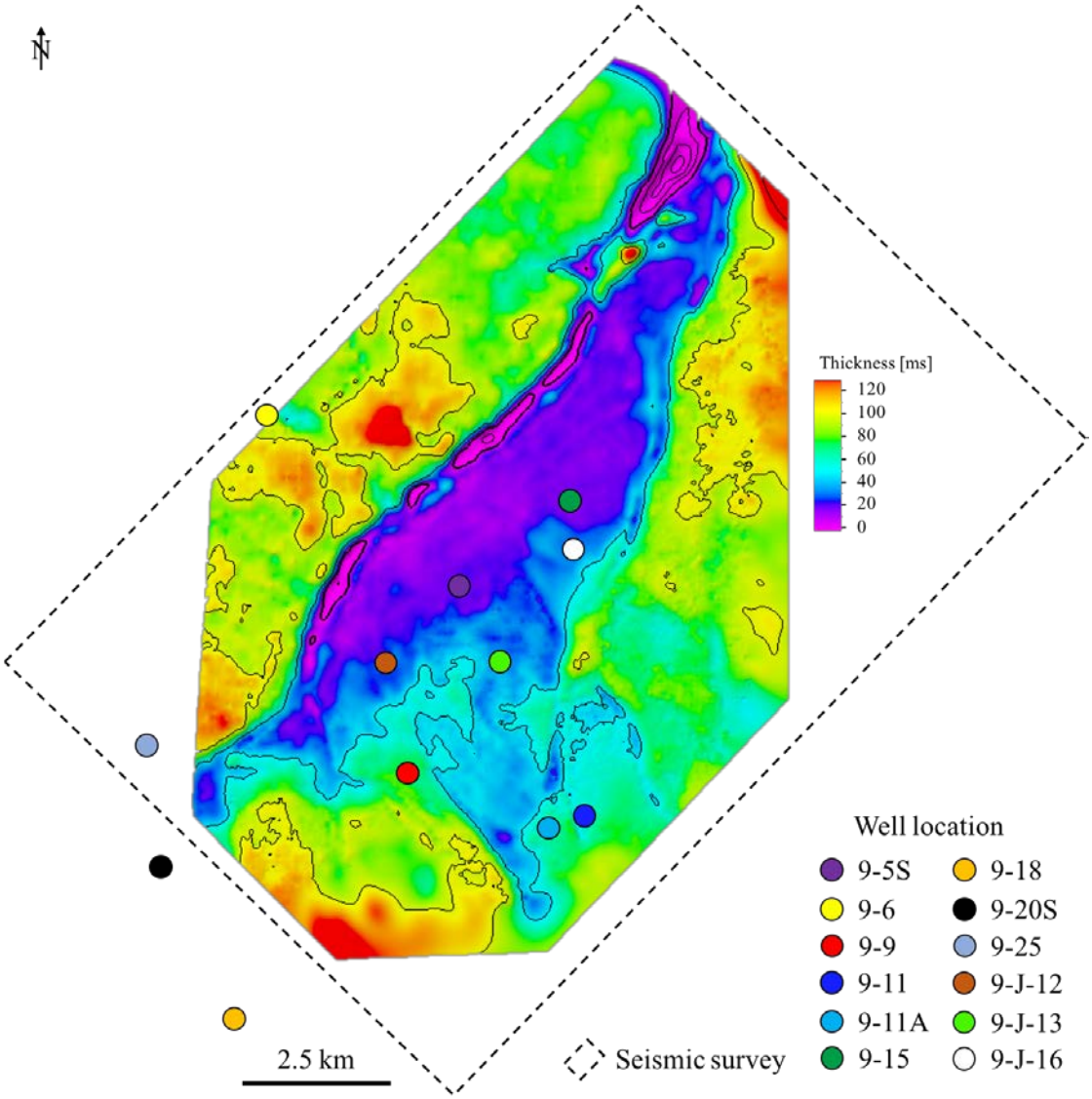

***Figure 6.4**: Time thickness map of the complete Brent Gp. Contour interval: 50 ms. Notice the gradual westward and northward thinning of the reservoir. Location of the available wells and the outline of the seismic survey are shown in the map.*

Focusing on the well (30/9-J-13) containing the only measured shear sonic log, the lithology (i.e. limestone, shale, and sandstone) is interpreted in an interval comprising the Shetland Gp and the complete Brent Gp (**Figure 6.5**). The gamma-ray (GR) log and the neutron porosity/density (Nphi/Rhob) cross-over facilitated the interpretation of limestone (overlapping Nphi/Rhob and low GR), shale (positive separation in the Nphi/Rhob and high GR), and sandstone (negative separation in the Nphi/Rhob and intermediate to low GR) (**Figure 6.5**).

By studying the Nphi/Rhob cross-over, a large negative separation sharply changing to a smaller negative separation, within the same sand-package is observed (**Figure 6.5**). This behavior indicates a change from a gas-saturated reservoir to an oil-saturated reservoir (potential gas-oil contact, **Figure 6.5**). This is also supported by the acoustic impedance, which increases with the drop in the Nphi/Rhob separation (**Figure 6.5**).

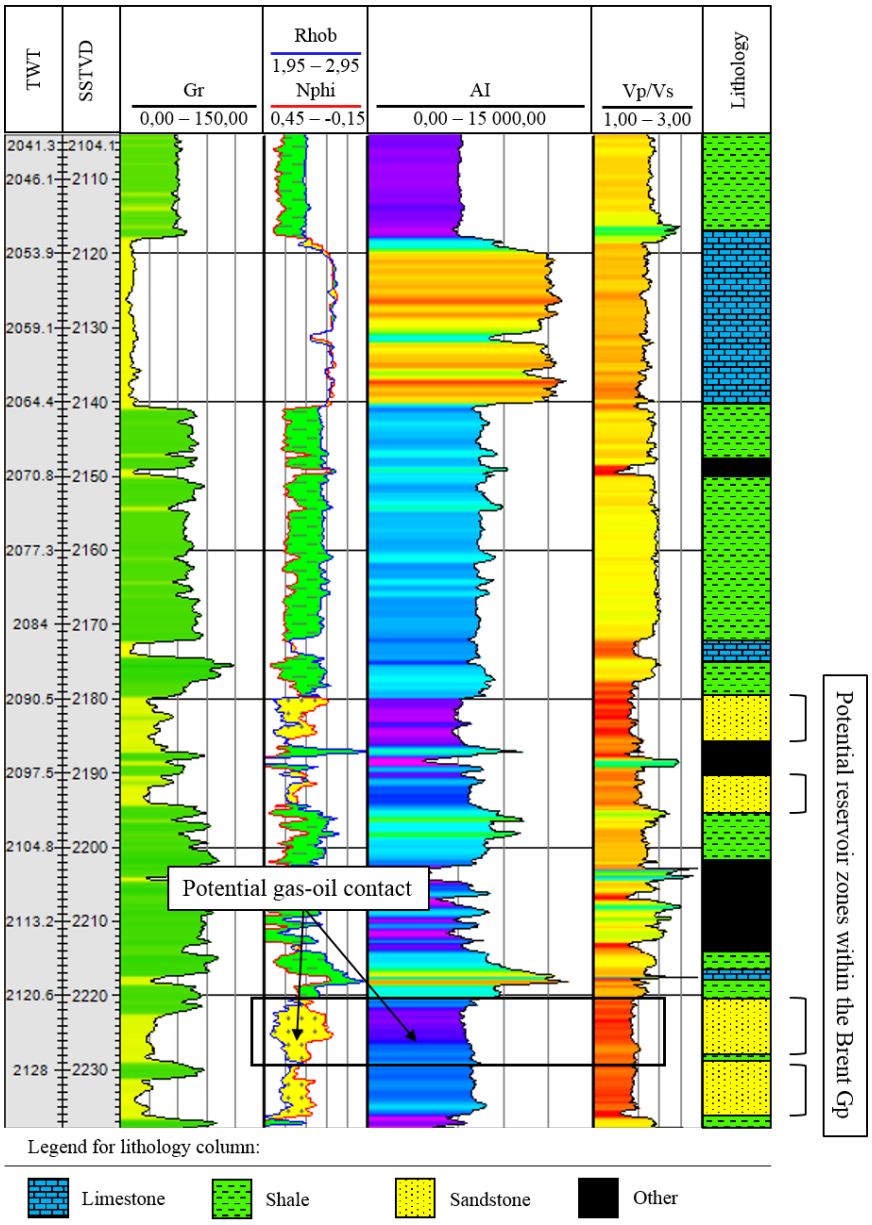

***Figure 6.5**: Well section for well 30/9-J-13. From left to right: TWT axis, SSTVD axis, gamma-ray (Gr), neutron/density (Nphi/Density), acoustic impedance (AI), Vp to Vs ratio (Vp/Vs), and interpreted lithology. The lithologies (prioritizing limestone, shale, and sandstone) are interpreted using the gamma-ray, neutron/density and the acoustic impedance logs. See Figure 6.2 for the well location.*

6.2. ROCK PHYSICS

In this section, the link between reservoir lithology/fluids and rock elastic properties (section 6.2.1), and the correlation of bulk modulus and Vp/Vs with the extended elastic impedance (section 6.2.2) are presented.

6.2.1. LITHOLOGY AND FLUID VERSUS ROCK PROPERTIES

By comparing the interpreted reservoir lithology in **Figure 6.5** with the acoustic impedance and Vp/Vs logs, it was possible to identify the interpreted limestone, shale, and sandstone using the two logs (see section 5.2.1). In **Figure 6.6** the acoustic impedance and Vp/Vs, from the well 30/9-J-13, are cross-plotted and color-coded by the gamma-ray log. The limestone (showing the lowest gamma-ray values) is different from the two other lithologies by having a much higher acoustic impedance. The sandstone (showing intermediate to low gamma-ray values) is also possible to differentiate because of the lower acoustic impedance and lower Vp/Vs compared to the shales. The cluster of intermediate to high gamma-ray values and the cluster of highest gamma-ray values correspond to the shale above and below the limestone, respectively. The shale above the limestone (Shetland Gp) also shows higher porosity values than the shale below the limestone (**Figure 6.6**).

By coloring the same cross-plot with the water-saturation log instead of the gamma-ray log, one can observe that most of the hydrocarbon-saturated rocks are easily differentiated from the water-saturated rocks by the low values of acoustic impedance and Vp/Vs (**Figure 6.7**). In general, the gas-saturated sandstones (interpreted on the Nphi/Rhob, **Figure 6.5**) show the lowest acoustic impedance and Vp/Vs values. However, it is difficult to separate between the gas- and the oil-saturated sands.

Due to the different Vp/Vs contrast between the hydrocarbon-saturated sands and the overlying shales or limestone in Figures 6.6 and 6.7, it should be possible to observe fluid-related amplitude anomalies with offset.

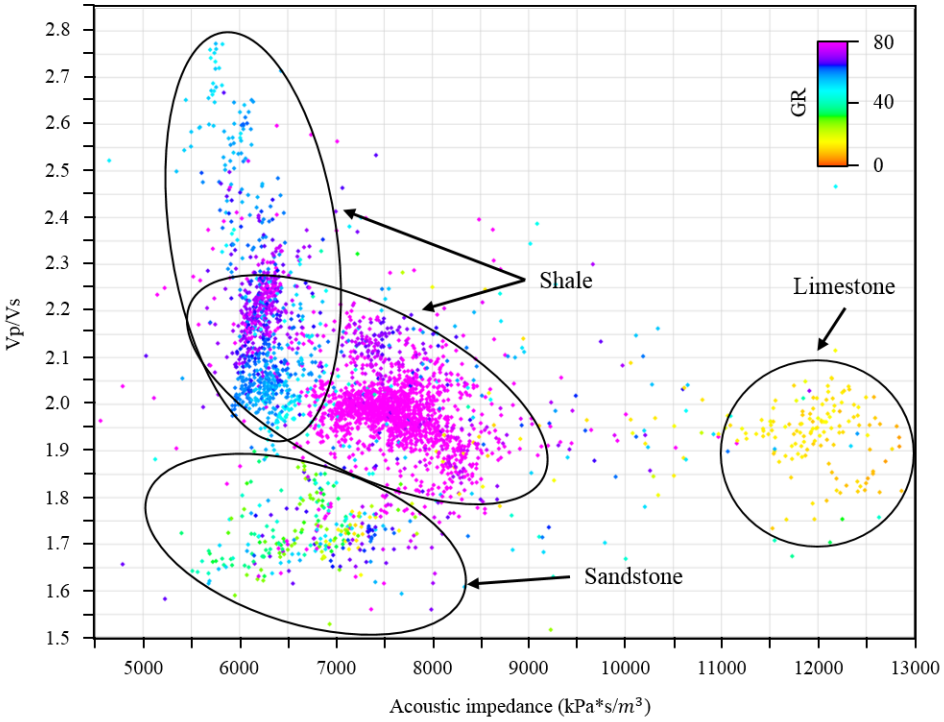

***Figure 6.6**: Acoustic impedance versus Vp/Vs from the well 30/9-J-13 colored by gamma-ray. Limestone, shale, and sandstone are differentiated in the cross-plot. See Figure 6.2 for the well location.*

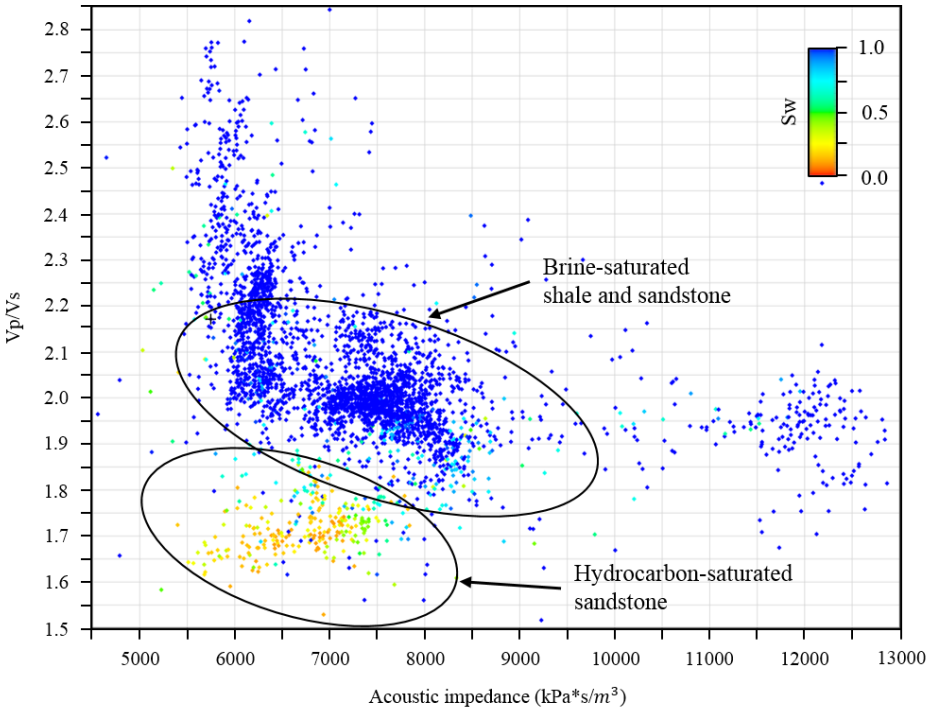

***Figure 6.7**: Acoustic impedance versus Vp/Vs from the well 30/9-J-13 water saturation. Hydrocarbon-saturated sands are separated from the brine-saturated shales and sands (following the background trend). See Figure 6.2 for the well location.*

6.2.2. EXTENDED ELASTIC IMPEDANCE

As previously discussed (see sections 3.3.4 and 5.2.3), the extended elastic impedance (EEI) log can be tuned to be approximately proportional to the elastic rock properties. **Figure 6.8** shows the bulk modulus and the Vp/Vs logs calculated at the well 30/9-J-13 (see section 5.2.2), and their EEI equivalent. At $\chi = 10^{o}$, the EEI approximately matches the bulk modulus log, and at $\chi = 45\ ^{o}$, the EEI matches the Vp/Vs log calculated at the well. **Figure 6.9** displays the correlation coefficient between the bulk modulus and the Vp/Vs with the EEI for a range of χ values.

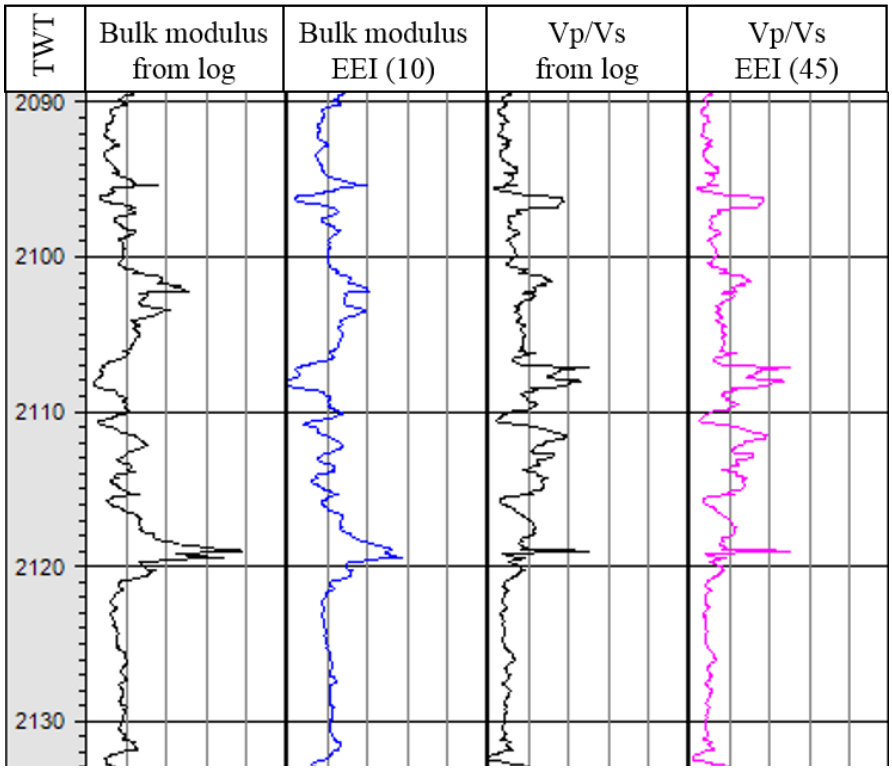

***Figure 6.8**: Well logs and equivalent EEI log derived at well 30/9-J-13. From left to right, depth (TWT), bulk modulus from rock physics, bulk modulus from EEI ($\chi = 10\ ^{o}$), Vp/Vs from log, and Vp/Vs from EEI ($\chi = 45\ ^{o}$).*

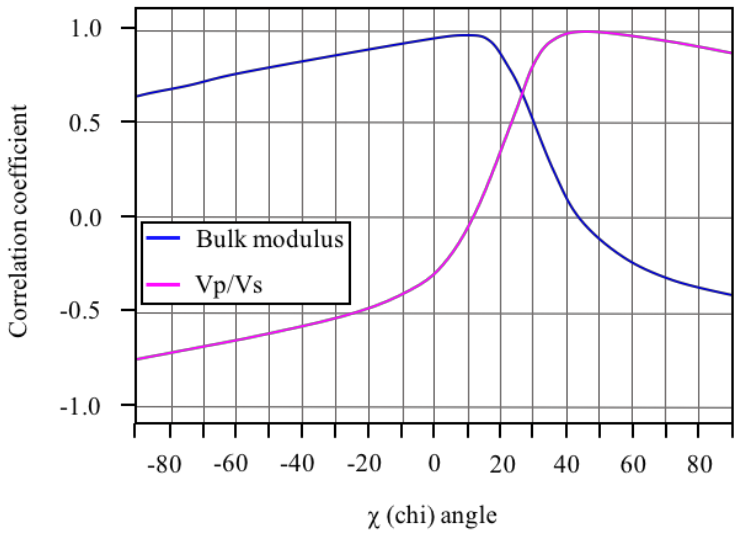

***Figure 6.9**: The correlation coefficient between the extended elastic impedance log, and the bulk modulus and Vp/Vs ratio logs, derived at well 30/-9-J-13, for the range (-90 to 90 degrees) of χ (chi) values.*

6.3. SEISMIC AMPLITUDE ANALYSIS

In this section, the seismic full stack analysis (section 6.2.1), the AVO analysis (section 6.2.2), and the EEI analysis (section 6.2.3) are presented.

6.3.1. SEISMIC FULL STACK ATTRIBUTES

Figure 6.10 shows RMS amplitudes from the PP and the PS seismic of an interval stretching from the top reservoir to 20 ms below the top, and overlain by the sand injectites. Obviously, the two maps show variations in the amplitudes. In the case of PS RMS, the amplitude anomalies could be attributed to changes in the lithology. In the case of the PP RMS, one cannot distinguish directly the anomalies caused by lithology from the ones caused by changes in the pore fluids (**Figure 6.10**a).

The two maps express amplitude anomalies along the western parts close to the Brage Fault, indicating anomalies related to changes in lithology (**Figure 6.10**). On the other hand, the anomalies surrounding the observation and the injection well in the PP, which are minor in the PS, may indicate the presence of hydrocarbon (**Figure 6.10**). An overview of the RMS amplitudes at the different well locations can be found in **Table 6.1**.

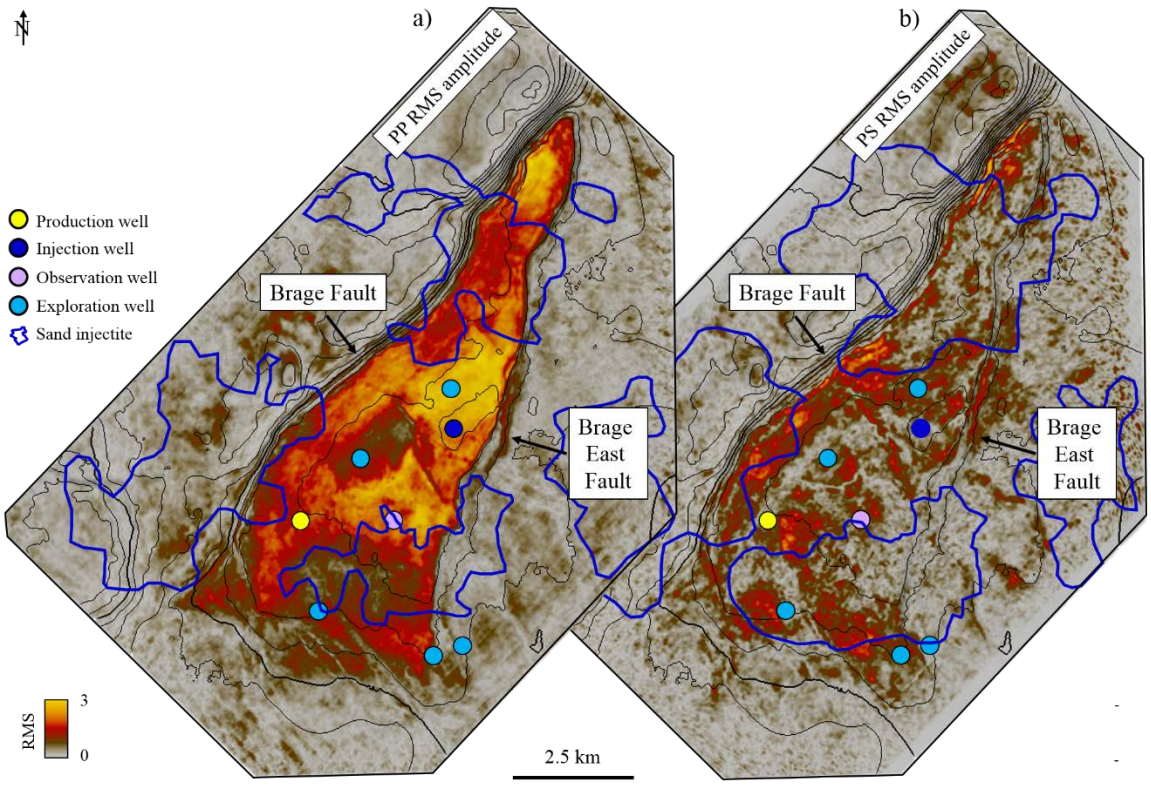

***Figure 6.10**: RMS amplitude maps from a) PP seismic and b) PS seismic of an interval stretching from the top reservoir (Brent Gp) to 20 ms below the top, and overlain by the sand injectites. RMS anomalies can be explained by changes in the lithology, and in the case of the PP, they can also be attributed to the pore fluids. Notice the loss of RMS amplitudes when entering the area beneath the sand injectites.*

***Table 6.1** Overview of the PP and PS RMS anomalies at the different well locations, including a column describing the content of the well at the Brent Gp level (NPD, 2018a). *Well-content at Brent Gp level is interpreted based on well logs.*

Well	Purpose	Content	PP RMS	PS RMS
30/9-5S	Exploration	Shows	Low	Low
30/9-9	Exploration	Oil	Intermediate	Low
30/9-11	Exploration	Dry	Low	Low
30/9-11A	Exploration	Shows	Intermediate	Intermediate
30/9-15	Exploration	Oil	High	Intermediate
30/9-J-12	Injection	/	High	Low
30/9-J-13	Observation	*Gas/Oil	High	Intermediate
30/9-J-16	Production	Oil	Intermediate	Low

6.3.2. AVO ANALYSIS

Figure 6.11a shows an intercept section through the potential fluid-related anomalies observed in the PP RMS amplitude map in **Figure 6.10**a. The top reservoir reflector displays a negative intercept response in these areas. **Figure 6.11**b shows a zoom-in of the near, mid, and far sections through the anomalous area. Highlighted in these sections is a typical AVO class III response (see **Figure 3.8**), with a negative intercept, and increasing negative response with offset (i.e. negative gradient) (**Figure 6.11**b).

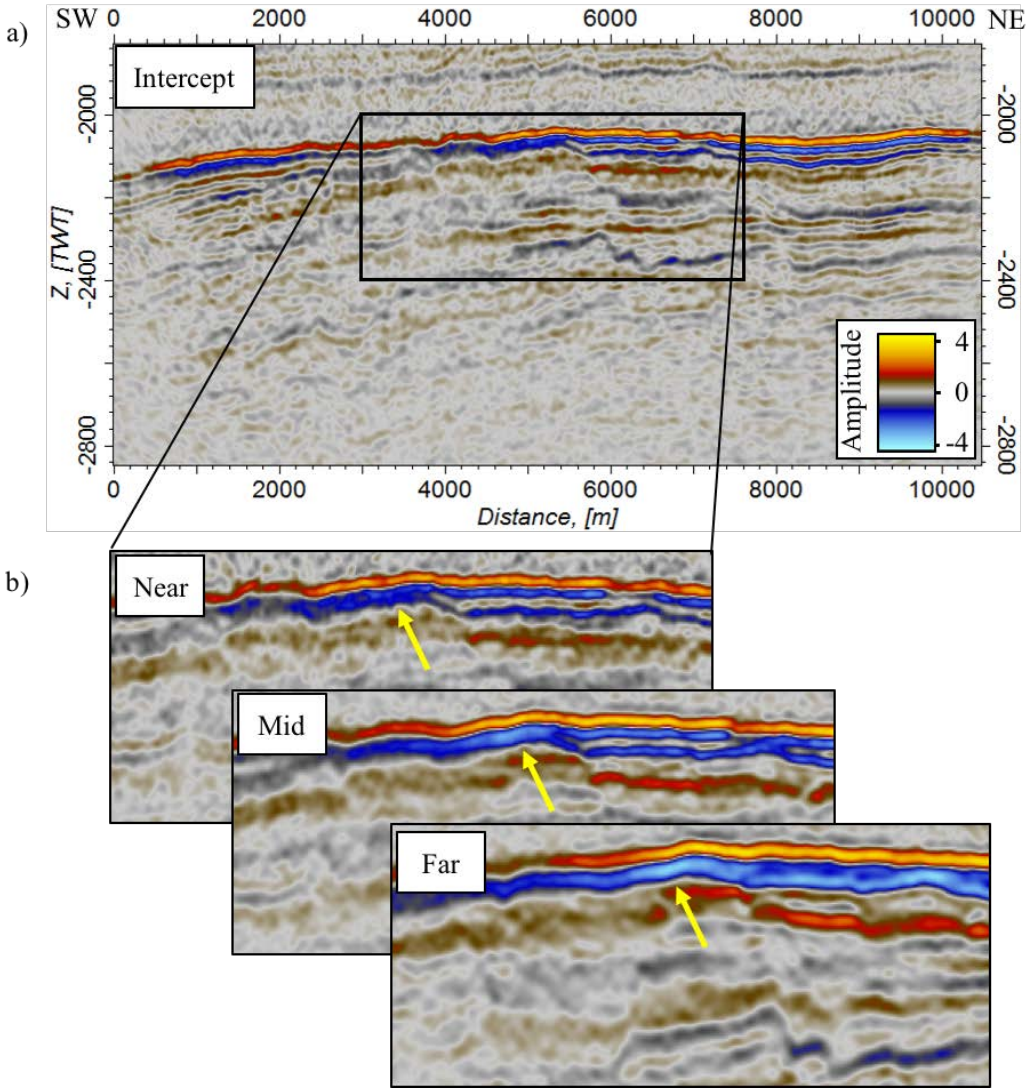

***Figure 6.11**: Intercept and angle stacks. a) Intercept section derived from the angle stacks. b) Zoom-in on a section (near, mid, and far stack, respectively) showing an AVO class III response with a negative intercept, and increasing negative response with offset (i.e. negative gradient). Location of the cross-sections can be found in Figure 6.12).*

Figure 6.12 display an intercept and a gradient map extracted at the top reservoir surface. Large areas of the reservoir structure show similar behavior as the sections in **Figure 6.11**, supporting the indication of AVO class III anomalies. By multiplying the intercept with the gradient (AVO product, see sections 3.3.2 and 5.3.2), it can be easier to investigate class II and III anomalies.

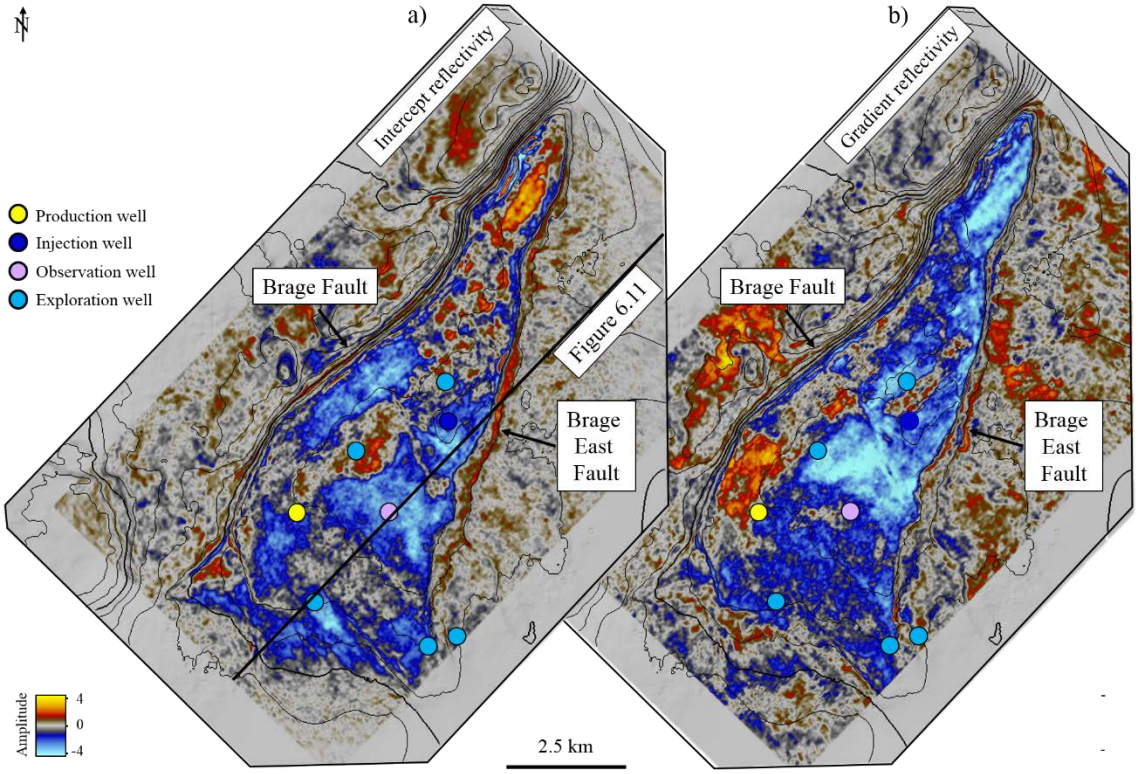

***Figure 6.12**: a) Intercept reflectivity and b) gradient reflectivity extracted at the top reservoir surface. Location of the cross-section in Figure 6.11a is highlighted in the intercept map.*

Figure 6.13 displays AVO attribute maps extracted at the top reservoir. **Figure 6.13**a shows the fluid factor anomalies at the top reservoir, indicating areas deviating from the background trend. In **Figure 6.13**b the AVO product map extracted at the top reservoir surface highlights the AVO class III (and potentially the class II) anomalies. These AVO anomalies may be attributed to the presence of hydrocarbons.

In general, the fluid factor and the AVO product maps are in good agreement, with the exception of the areas surrounding wells 30/9-5S and 30/9-15. An overview of the AVO anomalies at the different well locations is given in **Table 6.2**.

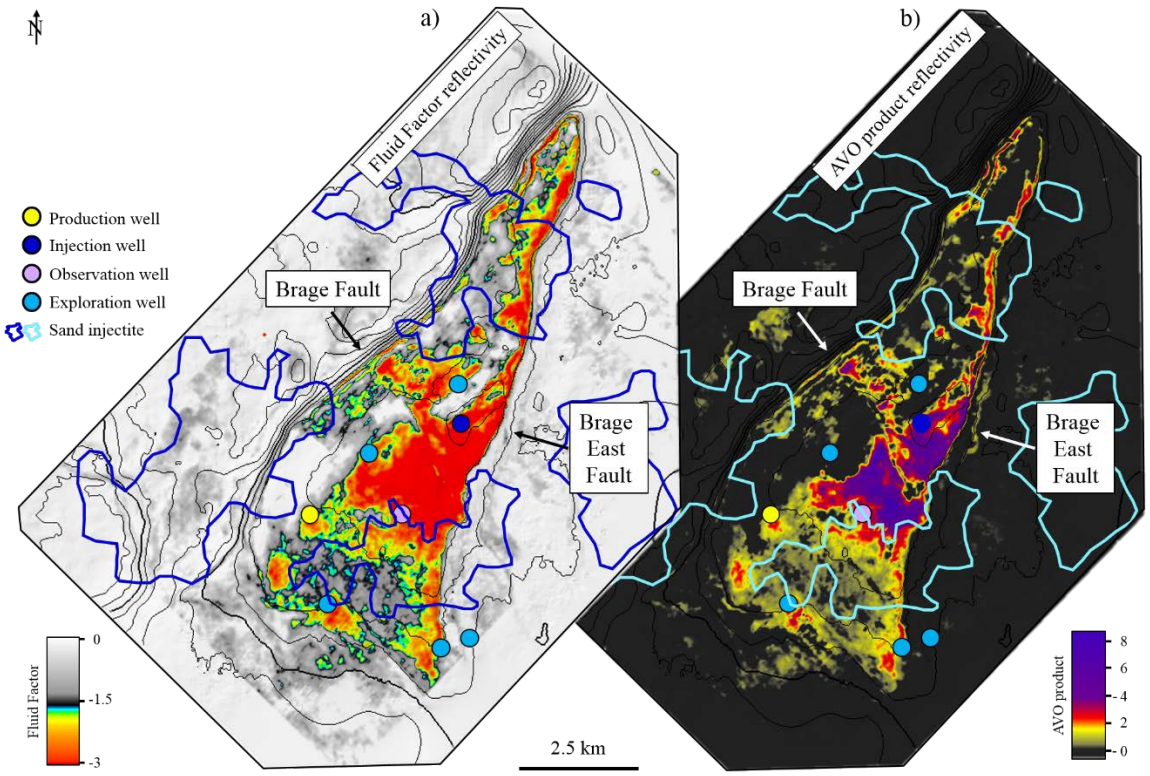

***Figure 6.13**: AVO attribute maps extracted at the top reservoir (Brent Gp). a) Fluid Factor. Negative response indicating deviations from the fluid line (i.e. the background trend). b) AVO product (intercept*gradient). Positive response indicating class III AVO anomalies. Notice the effect of the sand injectites (especially the southernmost injectite) on the two maps.*

***Table 6.2**: Overview of the anomalies and the AVO classes at the different well locations, including a column describing the content of the well at the Brent Gp level (NPD, 2018a). *Well-content at Brent Gp level is interpreted based on well logs.*

Well	Content	Intercept	Gradient	Fluid Factor	AVO class	AVO product
30/9-5S	Shows	+	-	(High) -	IIp	-
30/9-9	Oil	-	-	-	III	+
30/9-11	Dry	-	+	0	IV	-
30/9-11A	Shows	-	-	-	III	+
30/9-15	Oil	±	-	(High) -	II/IIp	±
30/9-J-12	/	-	-	(High) -	III	+
30/9-J-13	*Gas/Oil	-	-	(High) -	III	+
30/9-J-16	Oil	-	-	(High) -	III	+

6.3.1. EXTENDED ELASTIC IMPEDANCE

Figure 6.14 exhibits the intercept, bulk modulus, and Vp/Vs reflectivity for a cross-section through the anomalous area. In **Figure 6.14**b, a negative response corresponds with decreasing bulk modulus, and in **Figure 6.14**c a negative response corresponds with decreasing Vp/Vs. Consequently, the anomalies in the bulk modulus and the Vp/Vs reflectivity maps should indicate hydrocarbon-related AVO anomalies (see section 3.3.4).

Figure 6.15 display the bulk modulus reflectivity and the Vp/Vs reflectivity extracted at the top reservoir surface. The two maps seem to be in good agreement with each other, however some differences can be observed. The anomaly along the Brage Fault in the bulk modulus reflectivity map (**Figure 6.15**a) is downgraded in the Vp/Vs reflectivity map (**Figure 6.15**b). On the other hand, the anomaly to the east of well 30/9-5S, and the anomaly in the far north in the Vp/Vs map are downgraded in the bulk modulus reflectivity map (**Figure 6.15**). An overview of the EEI anomalies at the different well locations can be found in **Table 6.3**.

Overall, the EEI maps are in good agreement with the fluid factor and the AVO product maps in **Figure 6.13**, which highlights the AVO anomalies.

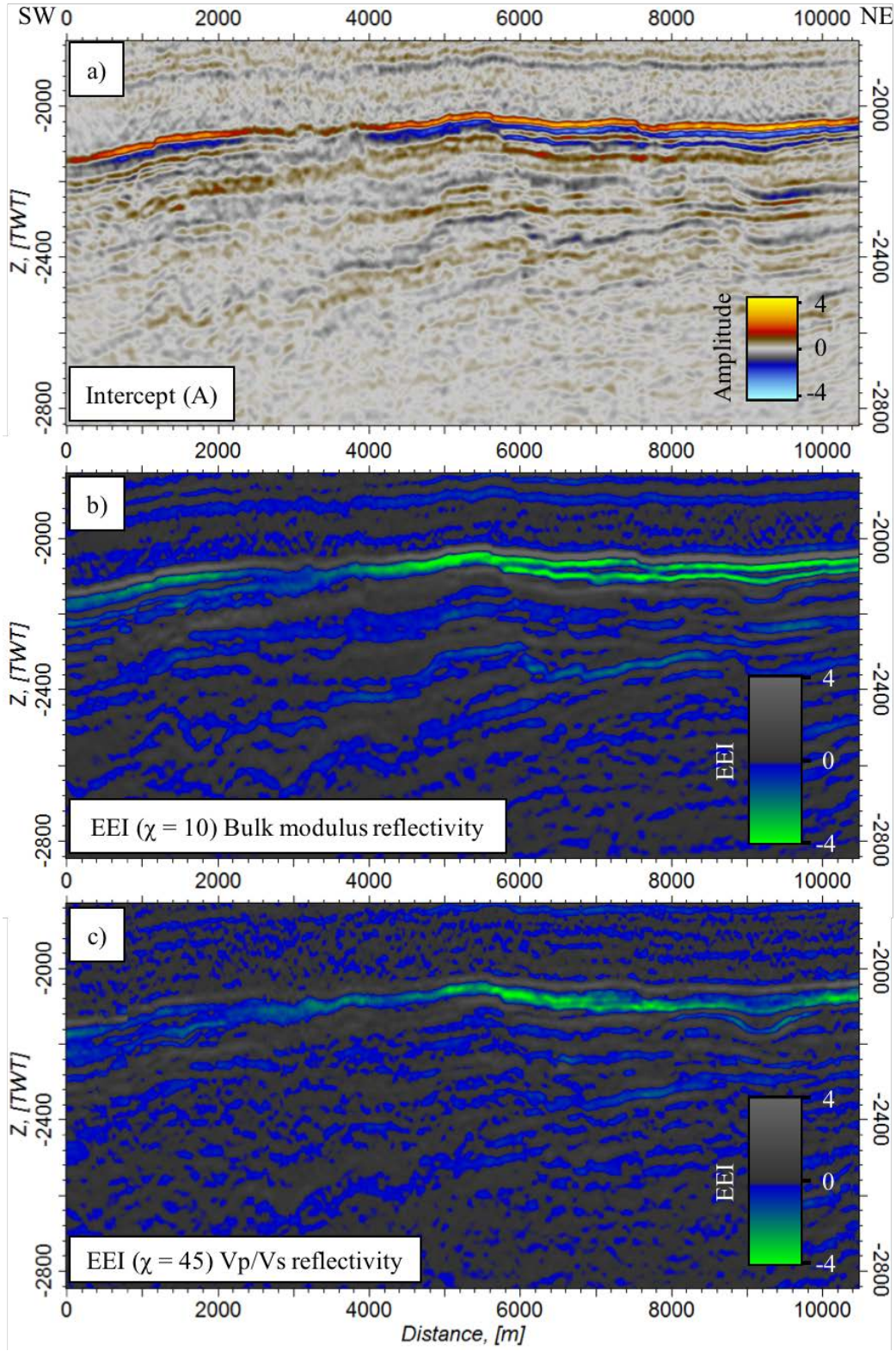

***Figure 6.14**: a) Intercept (A), b) bulk modulus reflectivity, and c) Vp/Vs reflectivity sections. Negative anomalies indicating decreasing bulk modulus in b) and decreasing Vp/Vs in c). Location of the cross-sections are shown in Figure 6.15.*

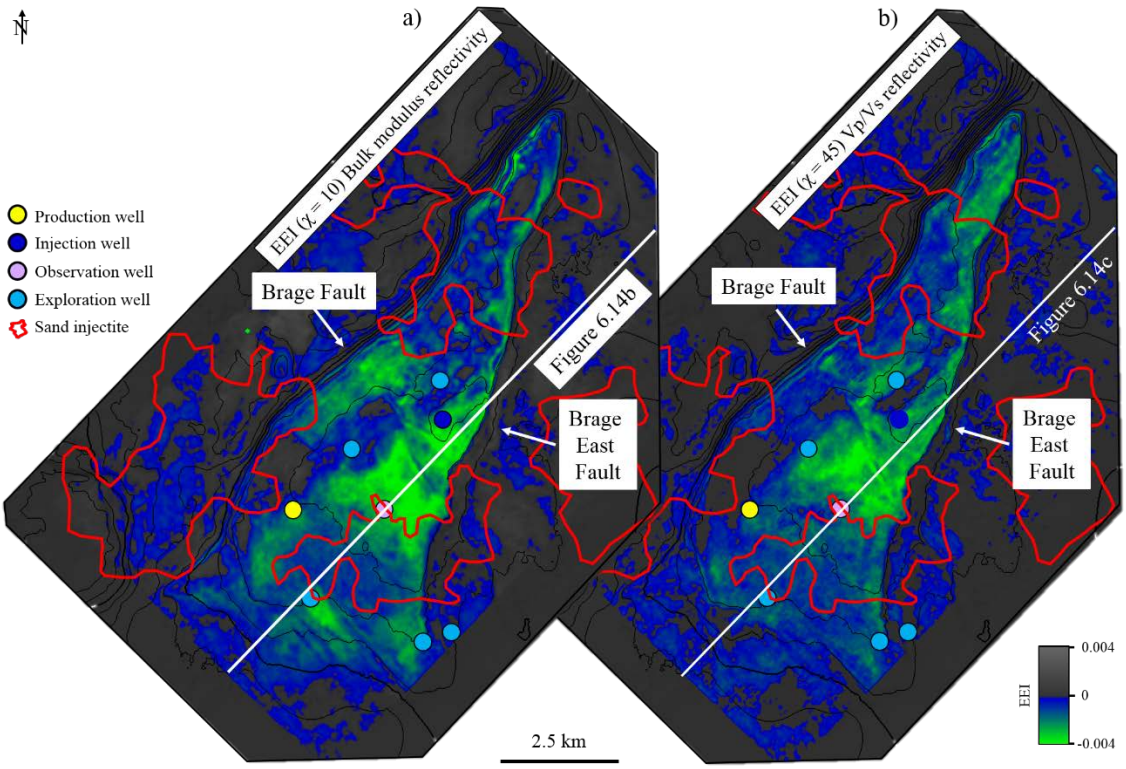

***Figure 6.15**: EEI reflectivity maps extracted at the top reservoir surface. a) EEI (χ = 10) bulk modulus reflectivity and b) EEI (χ = 45) Vp/Vs reflectivity. Negative anomalies indicating decreasing bulk modulus in a) and decreasing Vp/Vs in b). Location of the cross-sections in Figure 6.14 is highlighted in the respective maps.*

***Table 6.3**: Overview of the EEI anomalies at the different well locations, including a column describing the content of the well at the Brent Gp level (NPD, 2018a). *Well-content at Brent Gp level is interpreted based on well logs.*

Well	Content	EEI (χ = 10)	EEI (χ = 45)
30/9-5S	Shows	(Low) -	-
30/9-9	Oil	(High) -	-
30/9-11	Dry	0	0
30/9-11A	Shows	-	-
30/9-15	Oil	-	(High) -
30/9-J-12	/	(High) -	(High) -
30/9-J-13	*Gas/Oil	(High) -	-
30/9-J-16	Oil	-	-

6.4. INVERSION

In this section, the acoustic and shear impedance from the simultaneous AVO PP and joint PP and PS inversions (section 6.5.1 and 6.5.2, respectively), the QC of the resulting impedances (section 6.5.3), and the Vp/Vs from inversion (section 6.5.4) are presented.

6.4.1. SIMULTANEOUS PP AVO INVERSION

Figure 6.16 exhibits cross-sections through the anomalous area displaying the acoustic and shear impedances derived by the simultaneous PP AVO inversion. A clear decrease in the acoustic and shear impedances are observed in the south (at well 30/9-9) and in the north beneath the top reservoir (marked by yellow) (**Figure 6.16**). For the top of the structure, near well 30/9-J-13, a thin layer of lower acoustic impedance is observed, while there is no change in the shear impedance (**Figure 6.16**).

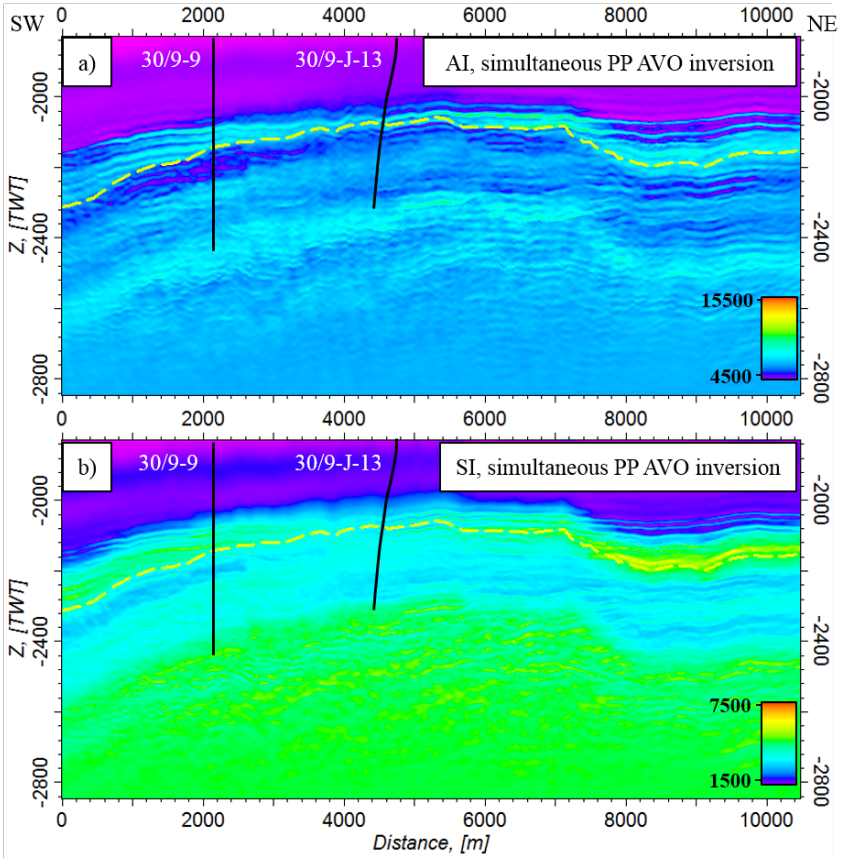

***Figure 6.16**: Resulting acoustic and shear impedances from simultaneous PP AVO inversion. a) Acoustic impedance and b) shear impedance. Top reservoir (yellow line) is highlighted in both cross-sections. See Figure 6.20 for the location of the cross-sections.*

6.4.2. JOINT PP AND PS AVO INVERSION

Figure 6.17 exhibits cross-sections equivalent to those in **Figure 6.16** for the acoustic and shear impedances derived by the joint PP and PS AVO inversion. Overall, the acoustic impedance is similar to the one derived by the PP AVO inversion, but there is a clearer decrease in the acoustic impedance at the top of the structure near well 30/9-J-13 (Figures 6.16 and 6.17). The shear impedance from the joint PP and PS AVO inversion is more heterogeneous than the shear impedance from the PP AVO inversion (Figures 6.16 and 6.17).

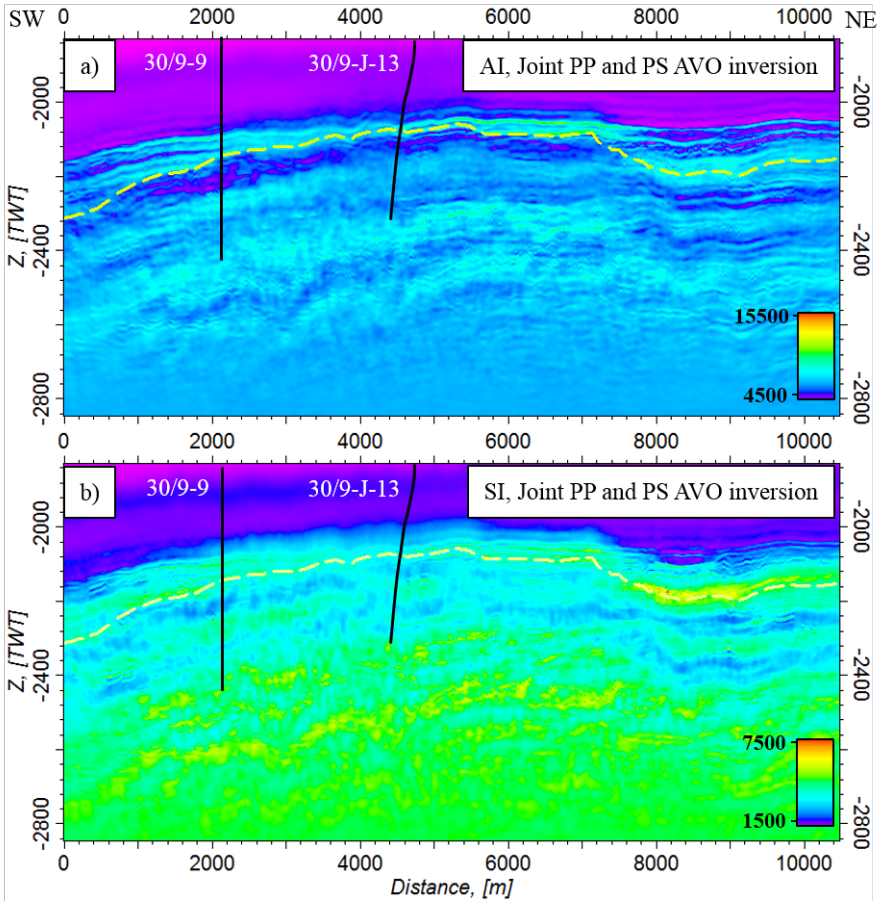

***Figure 6.17**: Resulting acoustic and shear impedances from joint PP and PS AVO inversion. a) Acoustic impedance and b) shear impedance. Top reservoir (yellow line) is highlighted in both cross-sections. See Figure 6.20 for the location of the cross-sections.*

6.4.3. INVERSION QC

Figure 6.18 shows the impedances delivered by the two inversion methods discussed above together with the impedance logs (convolved with a wavelet to match the seismic frequency spectrum) from well 30/9-9. The acoustic impedances (**Figure 6.18**a and b) show a good match with the acoustic impedance log. In the case of the shear impedance (**Figure 6.18**c and d), the joint PP and PS inversion is a better match than the PP AVO inversion.

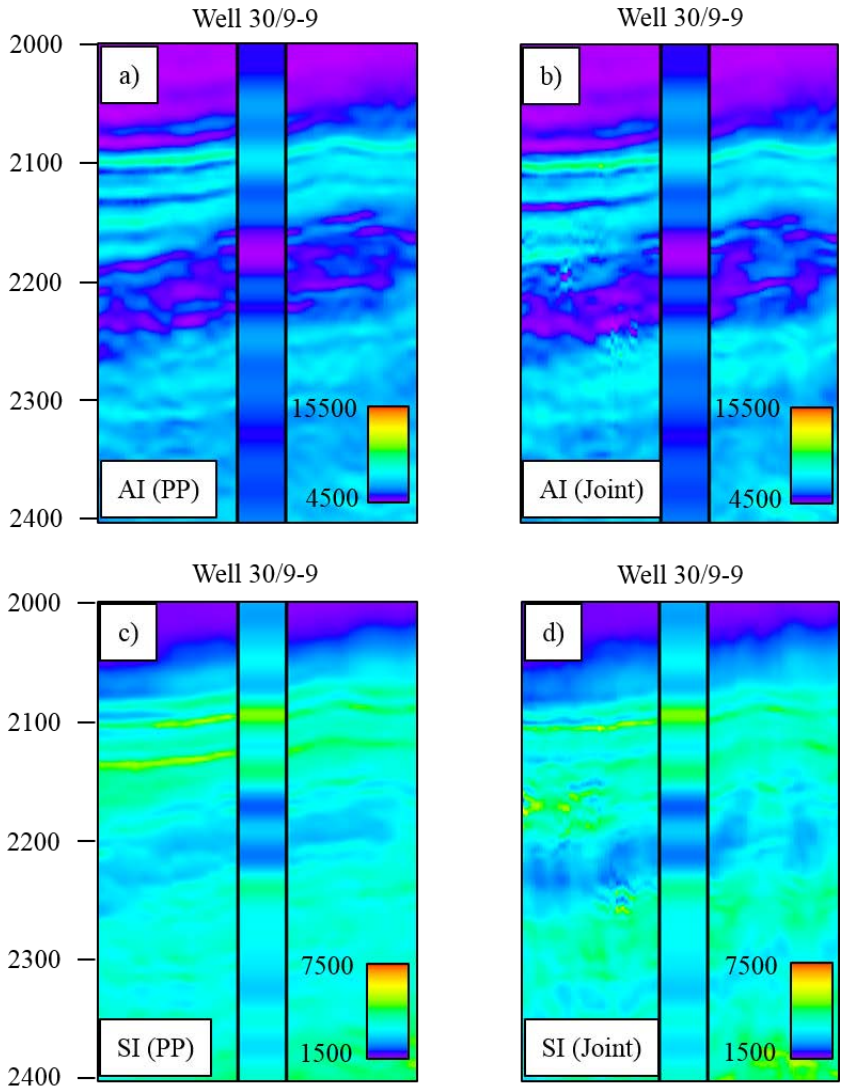

***Figure 6.18**: Seismic AVO inversion QC using well 30/9-9. a) and b) Acoustic impedance from PP AVO and joint PP and PS AVO inversion, respectively. c) and d) Shear impedance from PP AVO and joint PP and PS AVO inversion, respectively. Similar match is observed in the case of the PP impedance shown in a) and b). However, for the shear impedance, the joint PP and PS AVO inversion is a better match than the PP AVO inversion.*

Figure 6.19 provides the inversion QC using well 30/9-J-13. Similar to the results from well 30/9-9, the two PP impedances are in good agreement with the well data, and the shear impedance from the joint PP and PS AVO inversion matches better the well data than the shear impedance from the PP AVO inversion (Figures 6.18 and 6.19).

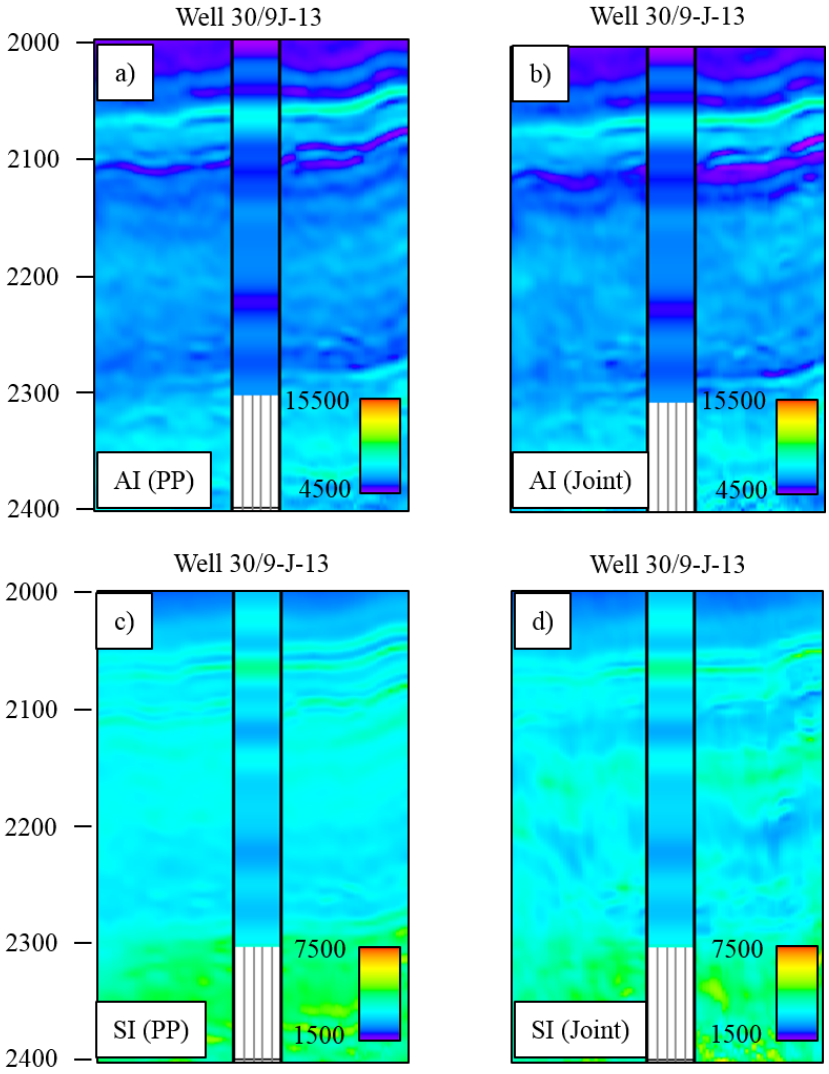

***Figure 6.19**: Seismic AVO inversion QC using well 30/9-J-13. a) and b) Acoustic impedance from PP AVO and joint PP and PS AVO inversion, respectively. c) and d) Shear impedance from PP AVO and joint PP and PS AVO inversion, respectively. Similar match is observed in the case of the PP impedance shown in a) and b). However, the shear impedance derived from the joint PP and PS AVO inversion matches better the well data than the shear impedance from the PP AVO inversion.*

6.4.4. VP/VS FROM INVERSION

Figure 6.20 exhibits Vp/Vs horizon probes (i.e. horizon slices whose top is defined by the seismic surface around the top of the Brent Gp, see also section 5.4.5) of 20 ms thickness. The opacity of the probe is adjusted (i.e. high Vp/Vs is filtered out) in order to highlight the Vp/Vs anomalies.

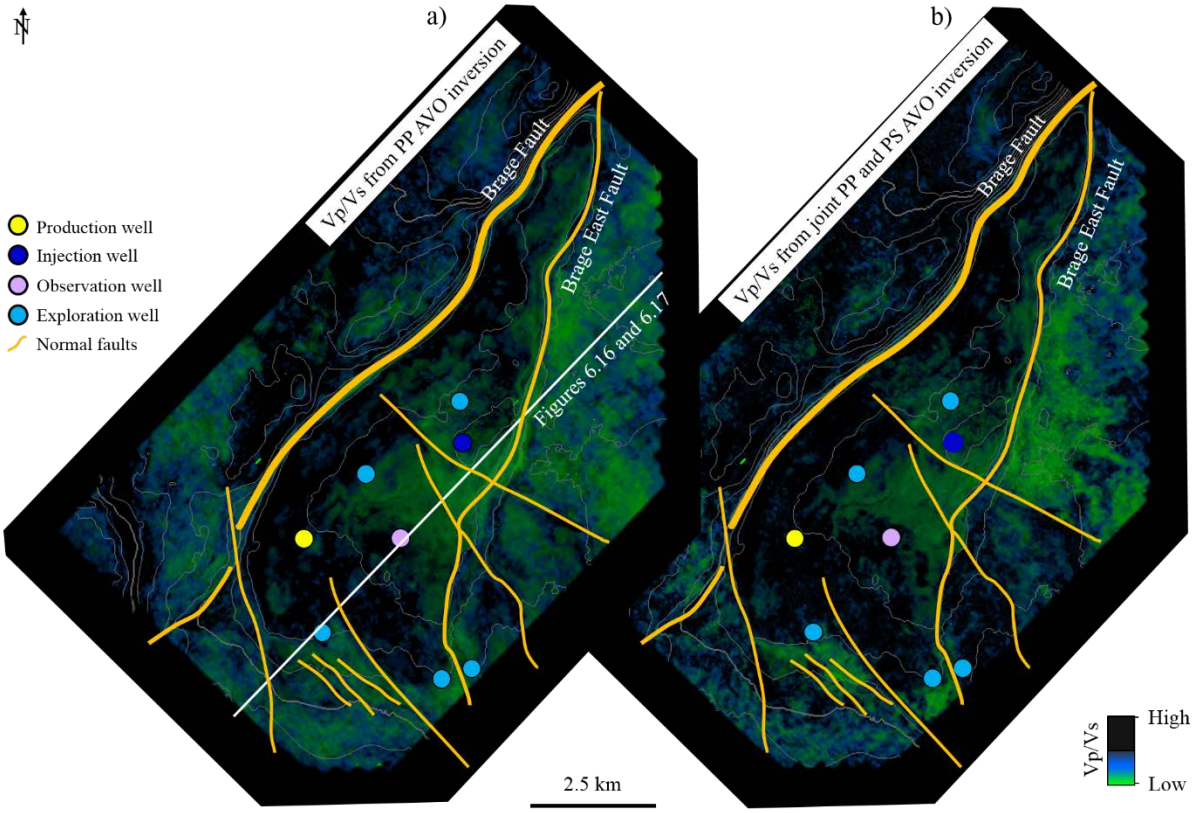

***Figure 6.20**: 20 ms thick Vp/Vs horizon probes (i.e. horizon slices) of the Brent Gp in map view. a) Vp/Vs derived in the PP AVO inversion. b) Vp/Vs derived in the joint PP and PS AVO inversion. The higher Vp/Vs values are filtered to highlight the low Vp/Vs values indicating hydrocarbons. Location of the cross-sections in Figures 6.16 and 6.17 is highlighted in the map.*

The anomalous low Vp/Vs values just north of the observation well and the low values surrounding the injection well match the anomalies of the fluid factor and the EEI Vp/Vs reflectivity maps. In general, the Vp/Vs horizon probes are in good agreement with the AVO attribute (**Figure 6.13**) and the EEI (**Figure 6.15**) maps. However, in the Vp/Vs from the PP AVO inversion, the easternmost exploration well (30/9-11) falls within an area of low Vp/Vs (**Figure 6.20**a), while in the Vp/Vs from the joint PP and PS inversion, the same production well falls within an area of higher Vp/Vs (**Figure 6.20**b).

Along the Brage Fault towards the northeast, the horizon probes show high Vp/Vs values, indicating less influence of hydrocarbons in the top 20 ms of the reservoir in these areas (**Figure 6.20**). Interestingly, both probes also display low Vp/Vs in the northeastern corner of the survey, east of the Brage East Fault, which does not match with the AVO and EEI maps. An overview of the Vp/Vs anomalies (of the top 20 ms of the reservoir) at the different well locations can be found in **Table 6.4**.

***Table 6.4**: Overview of the Vp/Vs anomalies of the top 20 ms of the reservoir at the different well locations, including a column describing the content of the well at the Brent Gp level (NPD, 2018a). *Well-content at Brent Gp level is interpreted based on well logs.*

Well	Content	Vp/Vs AVO PP	Vp/Vs joint PP and PS
30/9-5S	Shows	Low	Low
30/9-9	Oil	Low	Low
30/9-11	Dry	Low	High
30/9-11A	Shows	Low	Intermediate
30/9-15	Oil	Low	Low
30/9-J-12	/	Low	Low
30/9-J-13	*Gas/Oil	High	High
30/9-J-16	Oil	High	High

Figure 6.21, shows how the extent of the anomalous areas changes with increasing TWT. The anomalies, encasing the injection and the exploration (30/9-15) wells seem to increase with depth in both the PP and the joint PP and PS maps. In the southern segment covering the observation, production, and the four exploration wells (30/9-5S, 30/9-9, 30/9-11, and 30/9-11A), the anomalies in the joint PP and PS map decrease, whereas in the PP map they seem to increase.

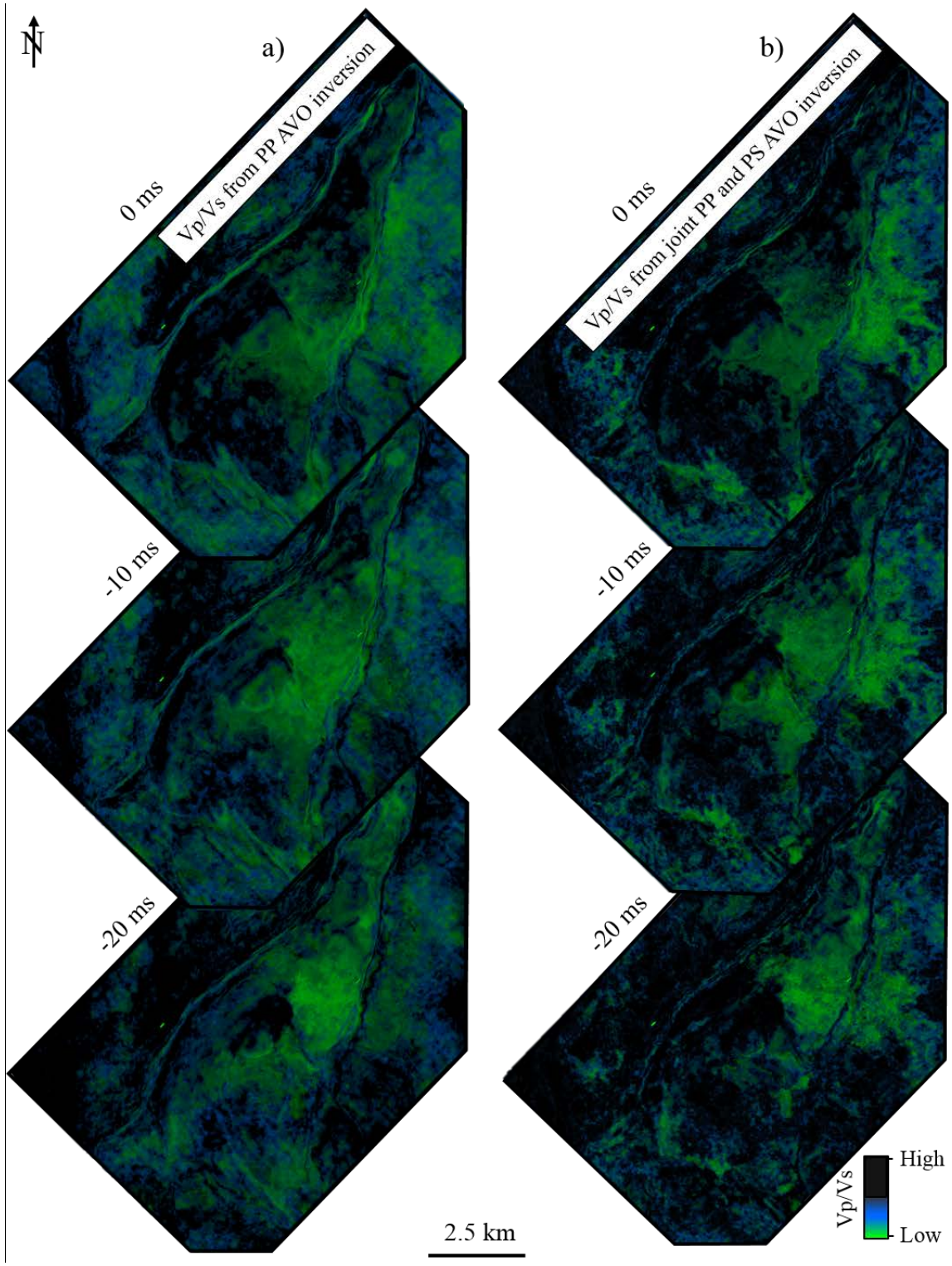

***Figure 6.21**: 20 ms thick Vp/Vs horizon probes (i.e. horizon slices) of the Brent Gp at different depth (TWT) offsets (0 ms (equivalent to the horizon probes in Figure 6.20), -10 ms, and -20 ms). a) Vp/Vs derived by the PP AVO inversion. b) Vp/Vs derived by the joint PP and PS AVO inversion. The higher Vp/Vs values are filtered to highlight the low Vp/Vs values indicating hydrocarbons. Notice the increasing extent of low Vp/Vs in the northern segment with TWT, in both the PP and the joint PP and PS probes.*

7. DISCUSSION AND CONCLUSION

In this section, the results from the rock physics studies, amplitude analysis, and AVO inversion are discussed (section 7.1), together with the conclusions (section 7.2). In addition, based on the results of this thesis, recommendations for future work (section 7.3) are proposed.

7.1. DISCUSSION

The results of this chapter are organized in three parts: Section 7.1.1 discusses the implications of the sand injectites and seismic resolution on the reservoir, section 7.1.2 discusses the lithology, and section 7.1.3 discusses the fluid distribution.

7.1.1. IMPLICATIONS OF THE SAND INJECTITES AND SEISMIC RESOLUTION

As described earlier (section 2.2.2), Dangerfield et al. (2010) and Mathewson et al. (2012) showed that the carbonate-cemented, high-velocity sand injectites in the overburden led to localized pull-up of deeper reflections and absorption of seismic energy in the Oseberg area. The impact of the sand injectites on the seismic data is clear in Figures 6.1 and 6.2, where the amplitudes at reservoir level show energy losses as the reflections enter the areas beneath the sand injectites. This effect is most prominent in the PS data, which suffers more energy loss than the PP data. Consequently, the areas covered by the sand injectites are considered uncertain for amplitude analysis.

When comparing the PP and PS data it is also important to be aware of the frequency content of the two types of seismic data. As stated in section 6.1.2, due to better vertical resolution in the deeper sections, the PP data carry more details about the structure of the reservoir zone compared to the PS data. Consequently, the PS data may not capture sufficient details in the thinner parts of the reservoir zone to be effectively used. The thinner parts (i.e. the parts below seismic resolution) of the reservoir may also experience tuning effects, influenced by the overlaying high-impedance carbonates of the Shetland Group. Large areas (in the west and the north) of the reservoir zone are 25 ms and thinner, hence below the seismic resolution of the data (**Figure 6.4**). Consequently, a tuning effect cannot be excluded.

7.1.2. LITHOLOGY

As discussed in Chapter 3 (section 3.1.4), since shear waves do not propagate through fluids, they are sensitive to changes in the lithology rather than the pore-fluid content. Consequently, the PS RMS anomalies can be explained by changes in the lithology (Figures 6.10b and 7.1). In general, the PS RMS amplitudes seem to be linked with the interpreted faults, going from high to low RMS amplitude (or vice-versa) when crossing a fault.

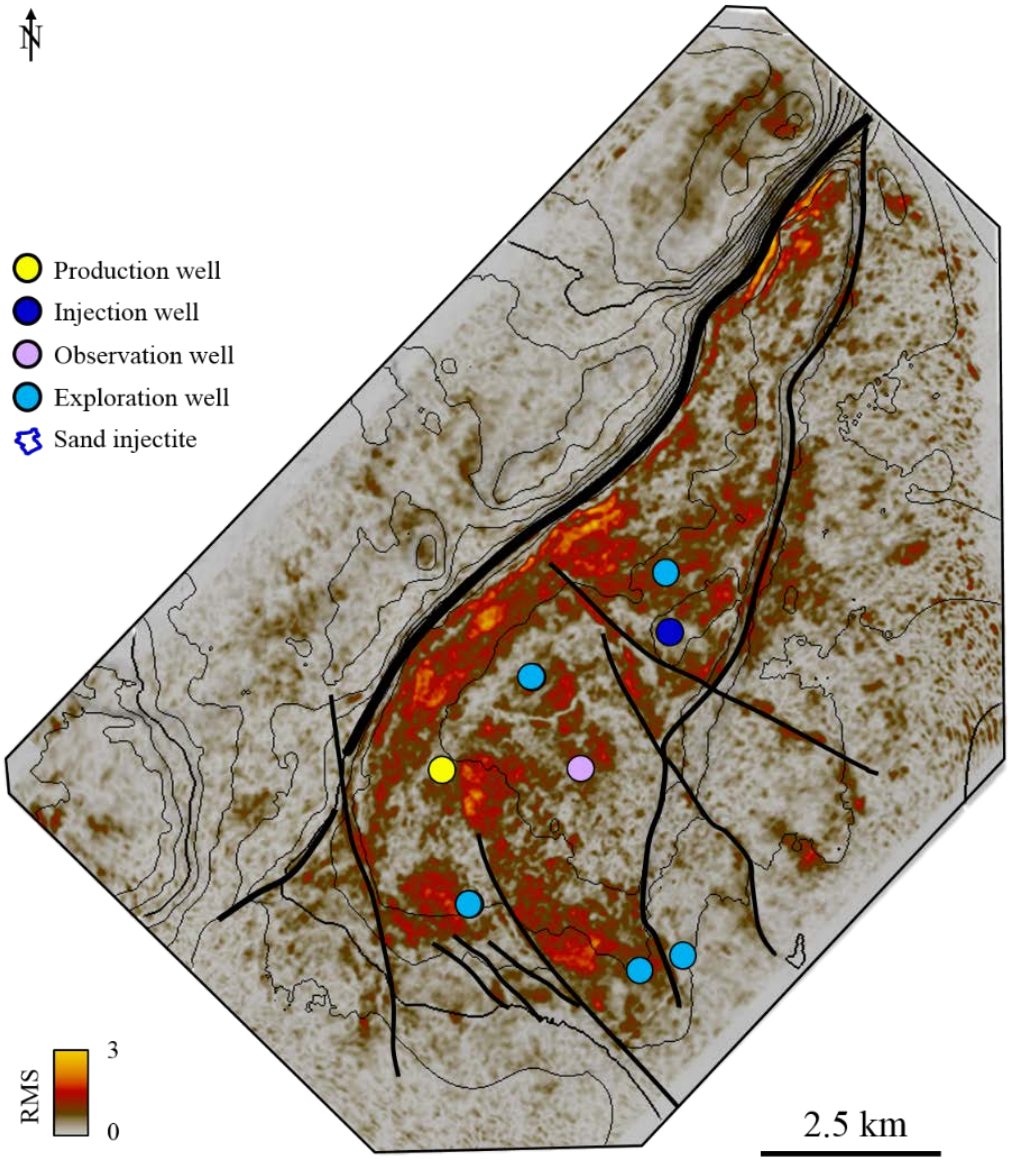

***Figure 7.1**: Relation between the major faults and the PS RMS amplitudes for an interval stretching from the top reservoir (Brent Gp) to 20 ms below the top. The RMS anomalies can be explained by changes in the lithology, which may also be associated to fault growth and fault deformation.*

The most noticeable are the high anomalies in the vicinity of the Brage Fault, which suggest a change of lithology, not only across the fault, but also within the reservoir (**Figure 7.1**). This change of lithology may be associated with the Late Jurassic growth of the Brage fault described by Færseth and Ravnås (1998), leading to maximum footwall uplift, and erosion of the footwall crest (see section 2.1). This is also supported by the gradual westward and northward thinning of the Brent Gp in the seismic time thickness map (**Figure 6.4**), and the well 30/9-5S, which encountered a thin succession of highly eroded sands at the Brent Gp interval (NPD, 2018a).

The rock physics study shows that it is possible to identify limestone, shale and sandstone with the use of acoustic impedance and Vp/Vs ratio (Figures 6.5 and 6.6). This relationship could be used to interpret lithologies at seismic scale using the estimates of acoustic impedance and Vp/Vs derived by the inversion. Considering the work of Wang (2000), who describes that clean sandstone (with < 15% clay) could have higher shear wave velocities than limestone and dolostone, the Vp/Vs volumes derived by the PP and joint PP and PS AVO inversion could indicate the reservoir sand distribution, in addition to the potential reservoir fluid distribution (Figures 6.20 and 6.21).

Overall, the joint PP and PS inversion shows a better match with the wells, and more details and variation (especially in the shear impedance) compared to the PP AVO inversion. This is in agreement with the results of Paydayesh (2014). Still, one issue arises attributed to the limited availability of shear sonic logs (only in the well 30/9-J-13). Since, the LFM (i.e. the shear impedance) is based on only one well with measured shear sonic, and the shear sonic logs in the other wells are estimated, the LFM is less reliable. Its impact on the inversion result is unknown.

7.1.3. FLUID DISTRIBUTION

From the PP RMS map (**Figure 6.10**), one cannot directly distinguish the fluid related anomalies from the lithology related anomalies. As discussed above, the PS RMS could be helpful. By analyzing the PS RMS in combination with the PP RMS, it might be possible to identify the anomalies driven by changes in the pore-fluids.

As discussed in section 3.3.2, the AVO and EEI analysis should allow to isolate the anomalies attributed to the presence of hydrocarbons. Overall, the AVO and EEI attribute maps are in good agreement with the well data (see **Table 7.1**). However, the well 30/9-5S (containing shows) is better supported by the AVO product than the fluid factor and EEI reflectivity maps. On the other hand, none of the AVO and EEI attributes seem to resolve the fact that well 30/9-11A has hydrocarbon shows.

***Table 7.1**: Overview of the RMS amplitudes, AVO and EEI anomalies, and the Vp/Vs (from inversion) anomalies at the different well locations, including a column describing the content of the well at the Brent Gp level (NPD, 2018a). *Well-content at Brent Gp level is interpreted based on well logs. Gas (G), Oil (O), intermediate (interm.), High (H), Low (L).*

Well	Cont-ent	RMS PP	RMS PS	Fluid Factor	AVO prod	EEI (10)	EEI (45)	Vp/Vs PP	Vp/Vs joint
9-5S	Shows	Low	Low	(H) -	-	(L) -	-	Low	Low
9-9	Oil	Interm.	Low	-	+	(H) -	-	Low	Low
9-11	Dry	Low	Low	0	-	0	0	Low	High
9-11A	Shows	Interm.	Interm.	-	+	-	-	Low	Interm.
9-15	Oil	High	Interm.	(H) -	±	-	(H) -	Low	Low
9-J-12	/	High	Low	(H) -	+	(H) -	(H) -	Low	Low
9-J-13	*G,O	High	Interm.	(H) -	+	(H) -	-	High	High
9-J-16	Oil	Interm.	Low	(H) -	+	-	-	High	High

As discussed in section 3.3.2, a rotation in the intercept-gradient cross-plot for the EEI to be approximately proportional to the bulk modulus, should maximize the distinction between different fluid types. However, in **Figure 6.9** only a small gain (approximately 10%) is observed relative to the amplitudes (determined by changes in the acoustic impedance) at normal incidence. Hence, the AVO response might still be influenced by changes in lithology in relation to, for example, faults (e.g. anomaly in the vicinity of the Brage Fault, **Figure 6.15**a).

On the other hand, the Vp/Vs (discussed in sections 3.1.4 and 3.4.4), is considered valuable in terms of highlighting the changes in the pore-fluid, and hence the associated AVO effect. The EEI Vp/Vs reflectivity map matches the well content of the different wells, and it shows a

lower negative response at the wells containing shows, compared to the other hydrocarbon-proven well locations (**Figure 7.2**a).

The rock physics study shows that it is possible to identify lithologies by cross-plotting the acoustic impedance against the Vp/Vs. In addition, the same approach facilitates differentiating between water-saturated and hydrocarbon-saturated sands. As mentioned in section 5.4.5, the value range defined in this study is used to filter out the high Vp/Vs values and highlight the anomalous low Vp/Vs values potentially associated with the presence of hydrocarbons.

In **Figure 7.2** the EEI Vp/Vs reflectivity map is compared with the Vp/Vs horizon probe (covering the top 20 ms of the Brent Gp). Overall, both maps highlight the same areas, except for the area surrounding the production well and the anomaly east of the Brage East Fault in the northeastern corner of the Vp/Vs horizon probes derived by the inversion (Figures 6.20 and 7.2). This area does not show any anomaly in the EEI Vp/Vs reflectivity map, and there is no well control to verify the origin of this anomaly. In the Vp/Vs from the joint inversion, it could be a result of the difference in the vertical resolution of the PP and PS data, creating an anomaly not related to hydrocarbons. However, since this anomaly is also present in the Vp/Vs from the PP AVO inversion, it is more likely associated with the reliability of the LFM as discussed above.

In the case of the production well, the anomaly in the Vp/Vs reflectivity, which is not present in the Vp/Vs from the joint inversion (and the PP AVO inversion), might be a consequence of the overlaying sand injectites (**Figure 7.2**). Due to the inclusion of the PS angles stacks, which have been proven to be more affected by the sand injectites than the PP stacks (see section 7.1.1), the results of the joint PP and PS inversion are also more affected than the results derived from the PP data (both AVO and inversion results).

Overall, the Vp/Vs derived from the two, PP AVO and joint PP and PS AVO, inversions (**Figure 6.20**), agree with the well content. In addition, the inversions facilitate investigation of the reservoir zones at different depths (**Figure 6.21**).

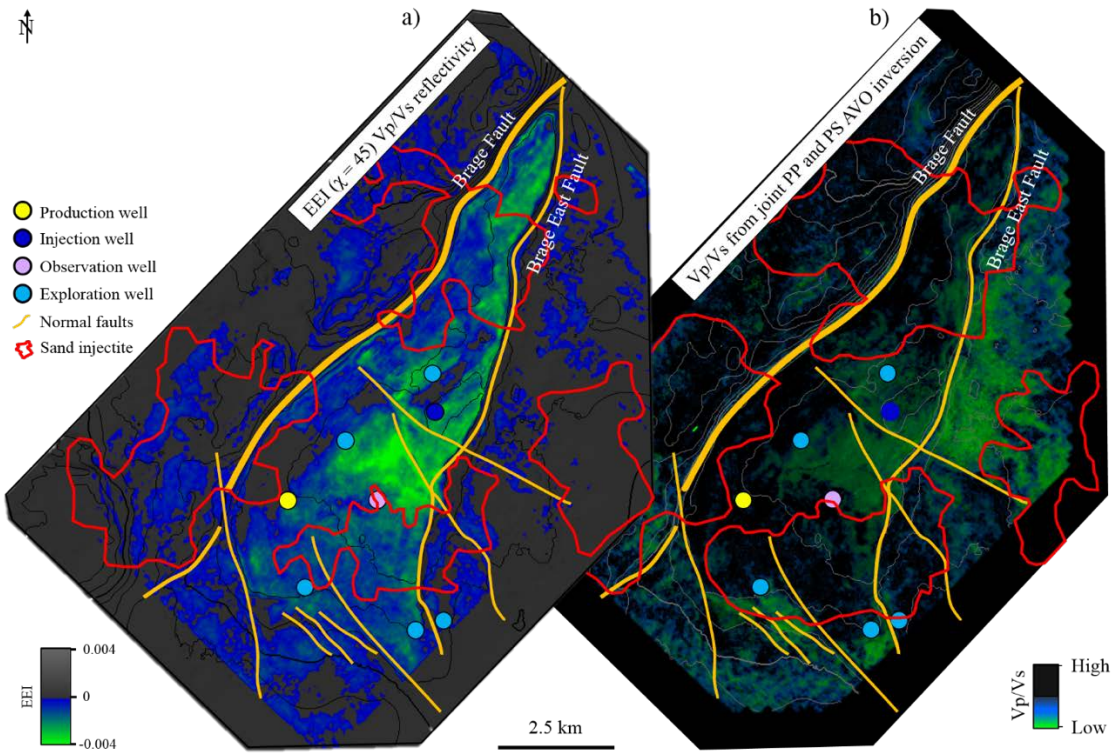

***Figure 7.2**: Vp/Vs maps. a) EEI (χ = 45) Vp/Vs reflectivity. Negative anomalies indicating decreasing Vp/Vs. b) 20 ms thick Vp/Vs horizon probe (i.e. horizon slice) of the Brent Gp in map view, derived in the joint PP and PS AVO inversion. The higher Vp/Vs values are filtered to highlight the low Vp/Vs values indicating hydrocarbons.*

7.2. CONCLUSION

Based on the theory, methods, and results of this Master thesis, the following conclusions are highlighted:

- The presence of sand injectites in the overburden clearly affects the amplitudes at reservoir level (especially the PS data). Hence, they influence the seismic study of this thesis.
- A combined analysis of PP and PS RMS amplitudes can be helpful in differentiating between fluid and lithology-related anomalies.
- The amplitude anomalies caused by changes in the pore-fluids are well defined by the AVO attribute and EEI reflectivity maps.
- Joint inversion of PP and PS data delivers more accurate and detailed shear impedance estimates compared to the simultaneous PP AVO inversion.
- Vp/Vs resulting from the joint inversion provides an outlined reservoir sand and hydrocarbon distribution.

This Master thesis underlines the potential benefits of including converted seismic waves in quantitative seismic interpretation. The compressional wave (PP) data emphasizes the changes in the pore-fluid content, whereas the converted wave (PS) data facilitates analyzing changes in the lithology. Therefore, Vp/Vs data derived from the joint inversion of PP and PS data can be useful for highlighting the reservoir sand and hydrocarbon distribution.

7.3. RECOMMENDATIONS FOR FUTURE WORK

Based on the results of this Master thesis the following improvements and recommendations for future work are suggested:

Interpretation:

- Detailed fault interpretation to fully understand the connectivity between the different compartments of the reservoir.

Rock physics:

- Improve the signature of different pore-fluid content by further rock physics studies.

Synthetic modelling:

- Synthetic wedge modelling studies of the wells to investigate the potential tuning effects of the thin reservoir zones.
- Fluid substitution and AVO modelling to investigate the expected seismic response with different pore-fluid content.

AVO Inversion:

- Better matching of the PP and PS angle stacks to minimize errors.
- Improve prediction of the shear sonic to get a more reliable LFM.
- A more detailed analysis of the wavelet used for inversion.

8. REFERENCES

Aki, K., and Richards, P. G., 1980, Quantitative seismology, W.H. Freeman and Co.

Avseth, P., Mukerji, T., and Mavko, G., 2010, Quantitative seismic interpretation: Applying rock physics tools to reduce interpretation risk, Cambridge university press.

Bach, T., Espersen, T. B., Pedersen, J. M., Hinkley, R., Pillet, W. R., and Rasmussen, K. B., 2000, Inversion of seismic AVO data, Methods and Applications of Inversion, Springer, p. 31-41.

Badley, M., Price, J., Dahl, C. R., and Agdestein, T., 1988, The structural evolution of the northern Viking Graben and its bearing upon extensional modes of basin formation: Journal of the Geological Society, v. 145, no. 3, p. 455-472.

Badley, M. E., Egeberg, T., and Nipen, O., 1984, Development of rift basins illustrated by the structural evolution of the Oseberg feature, Block 30/6, offshore Norway: Journal of the Geological Society, v. 141, no. 4, p. 639-649.

Barr, F. J., 1997, Dual-sensor OBC technology: The Leading Edge, v. 16, no. 1, p. 45-52.

Batzle, M., and Wang, Z., 1992, Seismic properties of pore fluids: Geophysics, v. 57, no. 11, p. 1396-1408.

Bortfeld, R., 1961, Approximations to the reflection and transmission coefficients of plane longitudinal and transverse waves: Geophysical Prospecting, v. 9, no. 4, p. 485-502.

Buland, A., and Omre, H., 2003, Bayesian linearized AVO inversion: Geophysics, v. 68, no. 1, p. 185-198.

Castagna, J. P., Batzle, M. L., and Eastwood, R. L., 1985, Relationships between compressional-wave and shear-wave velocities in clastic silicate rocks: Geophysics, v. 50, no. 4, p. 571-581.

Castagna, J. P., Swan, H. W., and Foster, D. J., 1998, Framework for AVO gradient and intercept interpretation: Geophysics, v. 63, no. 3, p. 948-956.

Chan, W.-k., 1998, Analyzing converted-wave seismic data: Statics, interpolation, imaging, and PP correlation, University of Calgary.

Chapman, C., 1976, Exact and approximate generalized ray theory in vertically inhomogeneous media: Geophysical Journal International, v. 46, no. 2, p. 201-233.

Connolly, P., 1999, Elastic impedance: The Leading Edge, v. 18, no. 4, p. 438-452.

Corcoran, C. T., 1989, Methods for processing converted wave seismic data, Google Patents.

Dangerfield, J., Daniels, J., Riste, P., Skaug, M., and Haugen, V., 2010, Ocean Bottom Seismic in the Oseberg South Area: 72nd EAGE Conference and Exhibition Extended Abstracts.

Duffaut, K., Alsos, T., Rognø, H., Al-Najjar, N. F., and Landrø, M., 2000, Shear-wave elastic impedance: The Leading Edge, v. 19, no. 11, p. 1222-1229.

Ensley, R. A., 1985, Evaluation of direct hydrocarbon indicators through comparison of compressional-and shear-wave seismic data: a case study of the Myrnam gas field, Alberta: Geophysics, v. 50, no. 1, p. 37-48.

Fatti, J. L., Smith, G. C., Vail, P. J., Strauss, P. J., and Levitt, P. R., 1994, Detection of gas in sandstone reservoirs using AVO analysis: A 3-D seismic case history using the Geostack technique: Geophysics, v. 59, no. 9, p. 1362-1376.

Fleming, N., Ramstad, K., Eriksen, S. H., Moldrheim, E., and Johansen, T. R., 2007, Development and Implementation of a Scale-Management Strategy for Oseberg Sør: SPE Production & Operations, v. 22, no. 03, p. 307-317.

Foster, D. J., Keys, R. G., and Lane, F. D., 2010, Interpretation of AVO anomalies: Geophysics.

Francis, A., 2013, A simple guide to seismic inversion.
Francis, A. M., and Syed, F. H., 2001, Application of relative acoustic impedance inversion to constrain extent of E sand reservoir on Kadanwari Field: SPE/PAPG Annual Technical Conference, Islamabad.
Færseth, R., 1996, Interaction of Permo-Triassic and Jurassic extensional fault-blocks during the development of the northern North Sea: Journal of the Geological Society, v. 153, no. 6, p. 931-944.
Færseth, R. B., and Ravnås, R., 1998, Evolution of the Oseberg fault-block in context of the northern north sea structural framework: Marine and Petroleum Geology, v. 15, no. 5, p. 467-490.
Gabrielsen, R. H., Færseth, R. B., and Jensen, L. N., 1990, Structural Elements of the Norwegian Continental Shelf. Pt. 1. The Barents Sea Region, Norwegian Petroleum Directorate.
Gaiser, J. E., 1996, Multicomponent VP/VS correlation analysis: Geophysics, v. 61, no. 4, p. 1137-1149.
Gardner, G., Gardner, L., and Gregory, A., 1974, Formation velocity and density—The diagnostic basics for stratigraphic traps: Geophysics, v. 39, no. 6, p. 770-780.
Garotta, R., Vuillermoz, C., and Granger, P., 1990, Comparing 3-D Operations and Results from Converted PS Waves: SEG Technical Program Expanded Abstracts, Society of Exploration Geophysicists, p. 1086 - 1088.
Granli, J. R., Arntsen, B., Sollid, A., and Hilde, E., 1999, Imaging through gas-filled sediments using marine shear-wave data: Geophysics, v. 64, no. 3, p. 668-677.
Hamada, G., 2004, Reservoir fluids identification using Vp/Vs ratio?: Oil & Gas Science and Technology, v. 59, no. 6, p. 649-654.
Hampson, D. P., Russell, B. H., and Bankhead, B., 2005, Simultaneous inversion of pre-stack seismic data: SEG Annual Meeting, Society of Exploration Geophysicists.
Han, D.-h., Nur, A., and Morgan, D., 1986, Effects of porosity and clay content on wave velocities in sandstones: Geophysics, v. 51, no. 11, p. 2093-2107.
Hanson, R., MacLeod, M., Bell, C., Thompson, C., and Somod, J., 1999, Multi-component seismic interpretation: data integration issues, Alba Field, North Sea, SEG Technical Program Expanded Abstracts, Society of Exploration Geophysicists, p. 808-811.
Helland-Hansen, W., Ashton, M., Lømo, L., and Steel, R., 1992, Advance and retreat of the Brent delta: recent contributions to the depositional model: Geological Society, London, Special Publications, v. 61, no. 1, p. 109-127.
Hilterman, F. J., 2001, Seismic amplitude interpretation: 2001 distinguished instructor short course, SEG Books, v. 4.
Jenkinson, T., Bansal, R., Martinez, A., Matheney, M., Khare, V., and Cornaglia, V., 2010, Joint PP-PS angle-stack analysis and AVA inversion in Grane Field, offshore Norway: The Leading Edge, v. 29, no. 10, p. 1228-1239.
Koefoed, O., 1955, On the effect of Poisson's ratios of rock strata on the reflection coefficients of plane waves: Geophysical Prospecting, v. 3, no. 4, p. 381-387.
Lawton, D. C., and Howell, C., 1992, P-SV and PP synthetic stacks, SEG Technical Program Expanded Abstracts, Society of Exploration Geophysicists, p. 1344-1347.
Lindseth, R. O., 1982, Digital processing of geophysical data: a review, SEG Books, v. 1.
Lu, J., Yang, Z., Wang, Y., and Shi, Y., 2015, Joint PP and PS AVA seismic inversion using exact Zoeppritz equations: Geophysics, v. 80, no. 5, p. R239-R250.

Løseth, T. M., Ryseth, A. E., and Young, M., 2009, Sedimentology and sequence stratigraphy of the middle Jurassic Tarbert Formation, Oseberg South area (northern North Sea): Basin Research, v. 21, no. 5, p. 597-619.

MacLeod, M., Hanson, R., Bell, C., and McHugo, S., 1999, The Alba Field ocean bottom cable seismic survey: Impact on development: The Leading Edge, v. 18, no. 11, p. 1306-1312.

Margrave, G. F., Stewart, R. R., and Larsen, J. A., 2001, Joint PP and PS seismic inversion: The Leading Edge, v. 20, no. 9, p. 1048-1052.

Mathewson, J., Evans, D., Adewumi, O., Horn, F., Leathard, M., Dangerfield, J., and Tonning, S., 2012, Improved imaging and resolution of overburden heterogeneity by combining amplitude inversion with tomography: 74th EAGE Conference and Exhibition.

NPD, 2018a, Factpages: Oseberg Sør, The Norwegian Petroleum Directorate, Accessed 01.01.2018.

-, 2018b, Factmaps: Oseberg Sør, The Norwegian Petroleum Directorate, Accessed 01.01.2018.

Nur, A., Mavko, G., Dvorkin, J., and Galmudi, D., 1998, Critical porosity: A key to relating physical properties to porosity in rocks: The Leading Edge, v. 17, no. 3, p. 357-362.

Ostrander, W., 1984, Plane-wave reflection coefficients for gas sands at nonnormal angles of incidence: Geophysics, v. 49, no. 10, p. 1637-1648.

Paydayesh, M., Leathard, M., and Mathewson, J., 2014, The Synergy Between PS and PP for Reservoir Definition-Applying Simultaneous Joint PP-PS Inversion for Oseberg South: 76th EAGE Conference and Exhibition.

Ravnås, R., and Bondevik, K., 1997, Architecture and controls on Bathonian–Kimmeridgian shallow-marine synrift wedges of the Oseberg–Brage area, northern North Sea: Basin Research, v. 9, no. 3, p. 197-226.

Ravnås, R., Bondevik, K., Helland-Hansen, W., Lømo, L., Ryseth, A., and Steel, R., 1997, Sedimentation history as an indicator of rift initiation and development: the late Bajocian-Bathonian evolution of the Oseberg-Brage area, northern North Sea: Norsk Geologisk Tidsskrift, v. 77, no. 4, p. 205-232.

Rodrigues, N., Cobbold, P., and Løseth, H., 2009, Physical modelling of sand injectites: Tectonophysics, v. 474, no. 3-4, p. 610-632.

Russell, B. H., 1988, Introduction to seismic inversion methods, Society of Exploration Geophysicists, Tulsa.

Rutherford, S. R., and Williams, R. H., 1989, Amplitude-versus-offset variations in gas sands: Geophysics, v. 54, no. 6, p. 680-688.

Shuey, R., 1985, A simplification of the Zoeppritz equations: Geophysics, v. 50, no. 4, p. 609-614.

Simm, R., and Bacon, M., 2014, Seismic Amplitude: An interpreter's handbook, Cambridge University Press.

Simmons, J. L., and Backus, M. M., 1996, Waveform-based AVO inversion and AVO prediction-error: Geophysics, v. 61, no. 6, p. 1575-1588.

Smith, G., and Gidlow, P., 1987, Weighted stacking for rock property estimation and detection of gas: Geophysical Prospecting, v. 35, no. 9, p. 993-1014.

Smith, G. C., and Gidlow, M., 2003, The fluid factor angle and the crossplot angle: SEG Technical Program Expanded Abstracts, v. 22, p. 185-188.

Steel, R., 1993, Triassic–Jurassic megasequence stratigraphy in the Northern North Sea: rift to post-rift evolution: Geological Society, London, Petroleum Geology Conference series, v. 4, no. 1, p. 299-315.

Steel, R., and Ryseth, A., 1990, The Triassic—Early Jurassic succession in the northern North Sea: megasequence stratigraphy and intra-Triassic tectonics: Geological Society, London, Special Publications, v. 55, no. 1, p. 139-168.
Stewart, R. R., 1990, Joint P and P-SV inversion: The CREWES Project Research Report, v. 2, p. 112-115.
Stewart, R. R., Gaiser, J. E., Brown, R. J., and Lawton, D. C., 2002, Converted-wave seismic exploration: Methods: Geophysics, v. 67, no. 5, p. 1348-1363.
-, 2003, Converted-wave seismic exploration: Applications: Geophysics, v. 68, no. 1, p. 40-57.
Stewart, R. R., Pye, G., Cary, P. W., and Miller, S., 1995, Interpretation of P-SV seismic data: Willesden Green: Alberta: CREWES Research Report, v. 5, p. 15.11-15.19.
Veeken, P., and Da Silva, 2004, Seismic inversion methods and some of their constraints: First break, v. 22, no. 6, p. 47-70.
Veire, H. H., and Landro, M., 2006, Simultaneous inversion of PP and PS seismic data: Geophysics, v. 71, no. 3, p. R1-R10.
Wang, Z., 2000, Velocity-density relationships in sedimentary rocks: Seismic and acoustic velocities in reservoir rocks, v. 3, p. 258-268.
-, 2001, Fundamentals of seismic rock physics: Geophysics, v. 66, no. 2, p. 398-412.
Whitcombe, D. N., 2002, Elastic impedance normalization: Geophysics, v. 67, no. 1, p. 60-62.
Whitcombe, D. N., Connolly, P. A., Reagan, R. L., and Redshaw, T. C., 2002, Extended elastic impedance for fluid and lithology prediction: Geophysics, v. 67, no. 1, p. 63-67.
Xu, C., 2011, Oil reservoir assessment using multicomponent seismic data: University of Calgary.
Xu, Y., and Bancroft, J. C., 1997, Joint AVO analysis of PP and PS seismic data: The CREWES Project Research Report, v. 9.
Yielding, G., Badley, M. E., and Roberts, A. M., 1992, The structural evolution of the Brent Province: Geological Society, London, Special Publications, v. 61, no. 1, p. 27-43.
Zhi, L., Chen, S., and Li, X.-y., 2013, Joint AVO inversion of PP and PS waves using exact Zoeppritz equation: SEG Annual Meeting, Society of Exploration Geophysicists.
Zoeppritz, K., 1919, VII b. Über Reflexion und Durchgang seismischer Wellen durch Unstetigkeitsflächen: Nachrichten von der Gesellschaft der Wissenschaften zu Göttingen, Mathematisch-Physikalische Klasse, v. 1919, p. 66-84.